Title
Field and Laboratory Investigations on Seismic Properties of Unconsolidated Saline Permafrost

Author
Dou, Shan

Publication Date
2015

Peer reviewed|Thesis/dissertation

Field and Laboratory Investigations on Seismic Properties of Unconsolidated Saline Permafrost

By

Shan Dou

A dissertation submitted in partial satisfaction of the

requirements for the degree of

Doctor of Philosophy

in

Earth and Planetary Science

in the

Graduate Division

of the

University of California, Berkeley

Committee in charge:

Professor Douglas S. Dreger, Chair
Professor Bruce A. Buffett
Professor David R. Brillinger
Dr. Jonathan Ajo-Franklin

Summer 2015

Field and Laboratory Investigations on Seismic Properties of Unconsolidated Saline Permafrost

Abstract

Field and Laboratory Investigations on Seismic Properties of Unconsolidated Saline Permafrost

by

Shan Dou

Doctor of Philosophy in Geophysics

University of California, Berkeley

Professor Douglas S. Dreger, Chair

Saline permafrost is mechanically weak and very sensitive to temperature disturbances, which makes its degradation particularly worrisome in a warming climate. For the purposes of hazard mitigation and prevention, it is crucial to gain knowledge about the properties and distributions of saline permafrost. However, one major challenge is that saline permafrost is hard to access, as it often is covered with a surficial layer of non-saline permafrost. Seismic methods are cost-effective methods for detecting and delineating saline permafrost, but research on seismic properties of unconsolidated saline permafrost is lacking.

The body of work comprising this dissertation is the first systematic study to investigate seismic properties of unconsolidated saline permafrost. Encompassing field and laboratory components, the study reveals pervasive presence of saline permafrost across the Barrow Environmental Observatory (BEO) in Alaska, and illustrates saline permafrost's striking vulnerability to temperature disturbances. Besides these findings regarding the distributions and properties of saline permafrost, other key deliverables of this dissertation include 1) rich seismic datasets for field and laboratory investigations of unconsolidated saline permafrost, 2) full-wavefield-based workflow for delineating irregularly dispersive media, and 3) improved microstructural realization regarding pore-scale distributions of ice in saturated frozen sediments.

Through this work we hope to call attention to the possibly ubiquitous presence of saline permafrost along the polar coasts. Considering the potentially large impact of saline permafrost degradation in a warming climate, we advocate future research needs in regional-scale mapping of saline permafrost and assessing its influences in climate modeling.

To my family

Table of contents

List of figures

List of tables

Acknowledgments

I foremost would like to thank Dr. Jonathan Ajo-Franklin and Professor Douglas Dreger for providing guidance, support and inspiration throughout the past four years of my graduate studies. I am also grateful for the support of my other dissertation committee members: Professors Bruce Buffet and David Brillinger.

I thank the group of scientists and engineers at Lawrence Berkeley National Laboratory (LBNL) that I have had great pleasure to work with and learn from: Michelle Robertson, Seiji Nakagawa, Baptiste Dafflon, John Peterson, Craig Ulrich, Paul Cook, Marco Voltolini, Brian Bonner, Yuxin Wu, James Berryman, Alejandro Morales, Justin Erspamer, Haruko Wainwright, Tom Daley, and Susan Hubbard.

I am deeply appreciative of the superb computing and network support provided by Charley Paffenbarger (UC Berkeley), Stephen Thompson (UC Berkeley), Bryan Taylor (LBNL), and Susan James (LBNL).

I thank Ved Lekic, Sanne Cottaar, Karl Kappler, Robert Porritt, Zack Geballe, Eloisa Zepeda Alarcon, Jane Kanitpanyacharoen, Ahyi Kim, Mei Xue, Kyung-Eun Min, Leslie Hsu, Su-Chin Chang, Kate Chen, Holly Brown, Avinash Nayak, Andrea Chiang, Cheng Cheng, and Sierra Boyd for always bringing wholesomeness into my life.

I am greatly indebt to my family and friends for their support.

I owe thanks to the group of amazing trainers at Cal Rec Sports center, Shane Barnard, Miwa Natsuki, Shaw-Chin Chiu, Shola Ogunlana, Andra Enoiu, and Geoffrey Suguitan, for giving me a dose of positive energy every day.

I would like to acknowledge the administrative staff at the Department of Earth and Planetary Science (EPS; UC Berkeley) and the Earth Sciences Division (LBNL). I thank the EPS gradate students' advisers, Professors Michael Manga and Roland Bürgmann, for their support and advice. I also thank all the fellow students in the EPS department for providing a friendly and stimulating environment that nurtures scientific progress.

This work is financially supported through contract DEAC0205CH11231 to Lawrence Berkeley National Laboratory (LBNL) and through contract DE-AC05-00OR22725 to Oak Ridge National Laboratory (ORNL). It is part of part of the Next-Generation Ecosystem Experiments (NGEE-Arctic) project sponsored by the Office of Biological and Environmental Research in the DOE Office of Science. I thank Susan Hubbard (LBNL) and Stan Wullschleger (ORNL) for their leadership within the NGEE-Arctic program.

1. Introduction

This dissertation investigates seismic properties of unconsolidated saline permafrost at both field and laboratory scales. One might ask why we should care about saline permafrost, and study its properties under changing temperature and salt content conditions? In the field how can seismic methods be used to characterize the structure of subsurface permafrost, infer its properties and why such techniques need development? In this first chapter the motivations, objectives, general background, and the scope of the laboratory and field scale experiments of this dissertation are introduced.

1.1 Occurrence, properties and significance of saline permafrost

Saline permafrost[1], as defined in Brouchkov (2002), contains soluble salts that take up at least 0.05 wt% of the dry weight of the soil[2]. Most of these salts originally came from seawater, as saline permafrost often originates from marine deposit and/or sediments that were subjected to seawater incursions. Hence, saline permafrost is widespread in subsea and costal areas of the Arctic (Figure 1.1)(e.g., Brouchkov 2003, Hivon and Sego 1993, Osterkamp 1989). Saline permafrost can also be found in cold and arid areas where the rate of evaporation exceeds the rate of precipitation (e.g., central Siberia and Antarctica), causing salts to become more and more concentrated in the residual pore fluids.

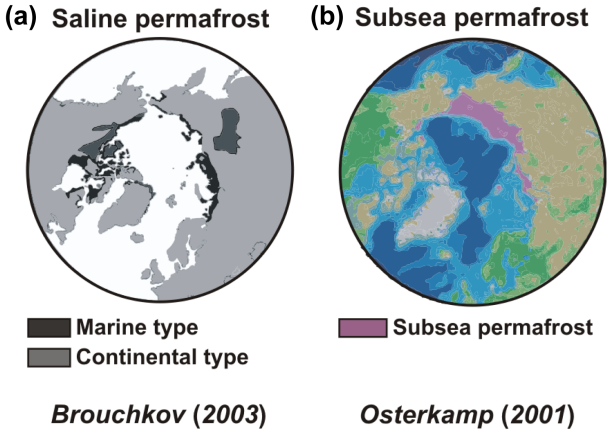

Figure 1.1 Distribution of saline permafrost in the Arctic. Adapted from Brouchkov (2003) and Osterkamp (2001).

Saline permafrost is very sensitive to temperature disturbances, which makes it influential in determining the overall response of permafrost systems in a warming climate. The fundamental cause of such sensitivity is the freezing point depression effect of dissolved salts. Because dissolved salts hinder freezing, saline permafrost ordinarily is only partially frozen despite the year-around exposure to subzero temperatures. The

[1] Permafrost is ground that remains at or below 0°C for at least two consecutive years.
[2] For saturated saline permafrost, this salt concentrate roughly translates to a pore-water salinity of 1–2 ppt.

partially frozen state of saline permafrost makes it vulnerable to temperature changes, as water and ice coexist in a delicate equilibrium that can be easily perturbed. An adverse consequence is that saline permafrost is likely to degrade at an accelerated pace in a warming climate, which could then intensify the positive feedback between climate change and permafrost degradation. For this reason, the distribution and properties of saline permafrost should be taken into account when predicting trajectories of climate change.

Knowledge about the distribution and properties of saline permafrost are also important for engineering applications as saline permafrost is often a source of geohazard (e.g., Hivon and Sego 1995, Nixon and Lem 1984, Ogata et al. 1983). Containing less ice, the key strengthening constituent of permafrost, saline permafrost is mechanical weaker and thus more readily deforms under load. Consequently, infrastructure built on saline permafrost is prone to damages because of the large strain that it can undergo placing substantial demands on structures built on or which are founded in the permafrost. Therefore, construction on saline permafrost is best avoided, however if that is not possible then special care must be taken during the design/planning stages to account for its unique properties. Hence, knowledge about the distribution, subsurface structure, and properties of saline permafrost are crucial for assessing the feasibility and design requirements for construction.

1.2 What makes seismic methods useful for studying saline permafrost?

For engineering applications and climate studies, field-scale (tens to hundreds of meters vertically and laterally) information about saline permafrost is crucial. However, field-scale mapping of permafrost is often challenging, because permafrost is a subsurface phenomenon that is rarely accessible or visible from the ground surface.

To probe permafrost, drilling and geophysical techniques both are useful. Drilling is a direct method that allows one to directly measure parameters of interests (e.g., sediment texture, temperature, ice/water content, and pore-water salinity) from the excavated soil/sediment samples. The limiting factors are its high costs, invasive nature, and limited spatial coverage as it only provides point measurements. Geophysical techniques are indirect methods that provide information about certain subsurface properties (e.g., seismic velocities and electrical resistivity), from which parameters of interest are then deduced during the geophysical interpretation stage (e.g., water/ice content and pore-water salinity). These techniques are mostly non-invasive, cost-effective, and can cover areas on the scale of tens to hundreds of meters both laterally and vertically. The drawback is that geophysical interpretation can be prone to ambiguities or errors. To aid proper interpretation, the ideal strategy is to drill at a few targeted locations where notable features are present in the geophysical profiles. In practice, geophysical techniques are often used as a primary method to obtain information on subsurface conditions and to guide drilling.

Geophysical prospecting of permafrost is made possible because geophysical properties change markedly as interstitial water freeze into ice (e.g., Hoekstra and McNeill 1973, Nakano and Froula 1973, Timur 1968). Among the commonly used geophysical properties, seismic (velocity and attenuation) and electrical (resistivity and permittivity) properties are most sensitive to the water-to-ice phase change. Therefore,

seismic and electrical methods are the most useful geophysical methods for permafrost studies (Andersland and Ladanyi 2004, Hauck and Kneisel 2008, Kneisel et al. 2008).

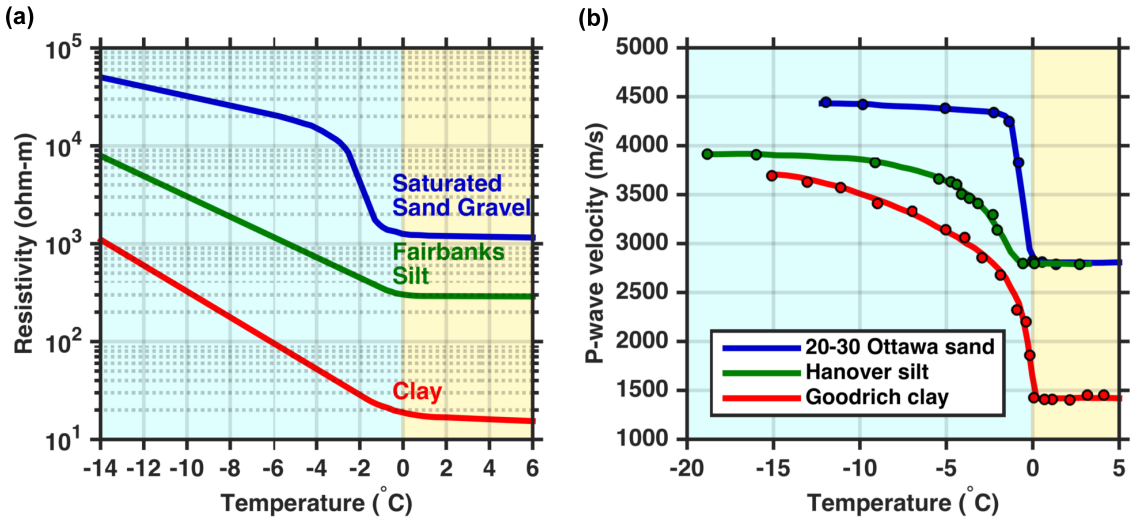

Figure 1.2 Examples of geophysical properties of permafrost: (a) electrical resistivity versus temperature (reproduced after Hoekstra and McNeill (1973)); (b) P-wave velocity versus temperature (reproduced after Nakano and Froula (1973)).

Note that sensitivity characteristics of seismic and electrical methods are controlled by different mechanisms. Electrical conduction relies on liquid water, whereas seismic waves transmit energy primarily through the solid matrix of the sediments. As a result, seismic properties tend to reach a plateau when most of the interstitial water has turned into ice, while electrical properties may continue to change (as shown in Figure 1.2). Such sensitivity difference is more obvious for saline permafrost, as electrical properties can respond strongly to the presence of charge carriers even when the amount of residual water is too small to yield noticeable changes in seismic properties. Consequently, electrical properties may exhibit a wide range of variation in saline permafrost, which increases the likelihood of interpretation ambiguities. Moreover, the saline interstitial water may render strong conductive loss, which limit the usefulness of electrical permittivity techniques (e.g., ground-penetrating radar imaging). In this regard, seismic methods are particularly useful for being able to remain robust when applied to saline permafrost.

In addition, seismic methods have at least two more merits:

- Among the geophysical properties that are useful for delineating permafrost, seismic velocities are most relevant for engineering practices, as velocity and strength properties of geomaterials often are correlated (e.g., Chervinskaya et al. 1998, Schön 2011).
- Seismic properties are sensitive primarily to the presence of ice and changes in ice content during freezing/thawing (e.g., Nakano and Arnold 1973, Zimmerman and King 1986). This makes seismic methods useful not only in providing point-in-time snapshots, but also in continuous monitoring of permafrost conditions to evaluate changes in its properties.

However, seismic properties of saline permafrost are rarely found in the existing literature. Field-scale studies are particularly lacking. The few laboratory studies that do exist focus mostly on consolidated sedimentary rocks (e.g., Desai and Moore 1967, Pandit and King 1978, 1979, Sondergeld and Rai 2007), whereas little research is done on unconsolidated sediments that comprise large portions of saline permafrost. Clearly more research is needed to close the knowledge gap about seismic properties of unconsolidated saline permafrost. This dissertation aims to narrow this gap.

1.3 What field and laboratory methods were used, and why?

The characteristics of unconsolidated saline permafrost determine what types of seismic methods are applicable. In this dissertation, surface-wave methods are used to acquire field data, and ultrasonic pulse-transmission methods are used to acquire laboratory data. In this section, I will explain the rationales behind these choices.

For seismic field testing, mapping saline permafrost is challenging given that commonly used body-wave methods such as reflection and refraction often become ineffective. This is because the success of these methods requires the subsurface to have a positive velocity gradient (seismic velocities increase with increasing depths). Although this generally is the case for the Earth's near-surface strata, the presence of saline permafrost is more likely to result in drastic velocity reversals, as saline permafrost often exists as embedded low-velocity features that are overlain by high-velocity surficial layers.

The irregular velocity structure of saline permafrost reflects the heterogeneous salt distribution that is typical of frozen ground; Salt-enriched, ice-poor layers usually lay underneath surficial layers that are salt-depleted and ice-rich (Figure 1.3) (e.g., Hivon and Sego 1993). Published laboratory studies have shown that such salt distribution is attributable to the desalting effect of ice: That is, growing ice excludes dissolved salts because crystal lattice of ice has no room to accommodate salt molecules. As the ground freezes from the top toward the bottom, the ice formed near the ground surface "squeezes" salts out, causing the residual pore water to have increased salinity (and density) and start to migrate downward under the influence of density-driven flow and diffusion (e.g., Baker and Osterkamp 1989, Bing et al. 2015).

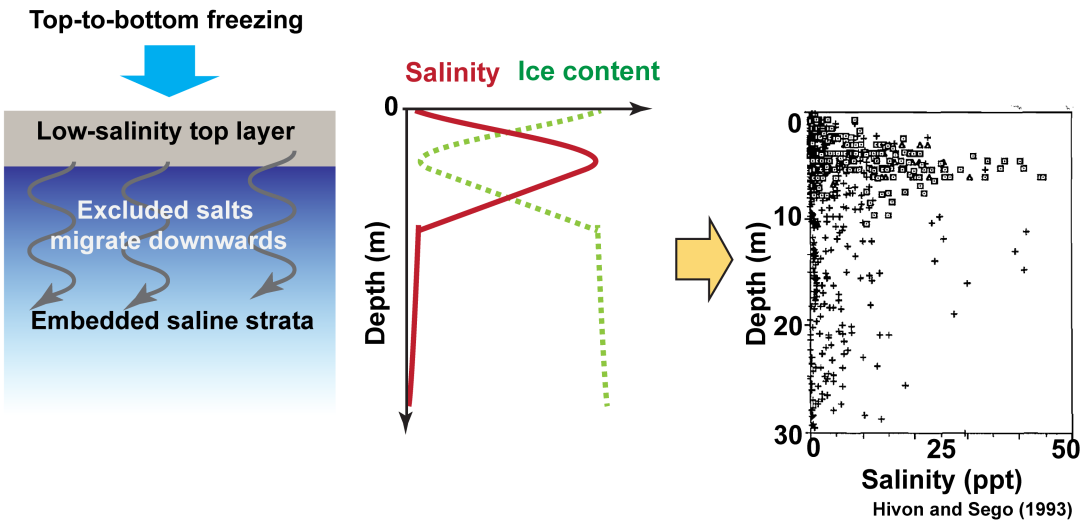

Figure 1.3 Schematics illustrating the likely formation process of saline permafrost. The salinity distribution profiles come from Hivon and Sego (1993).

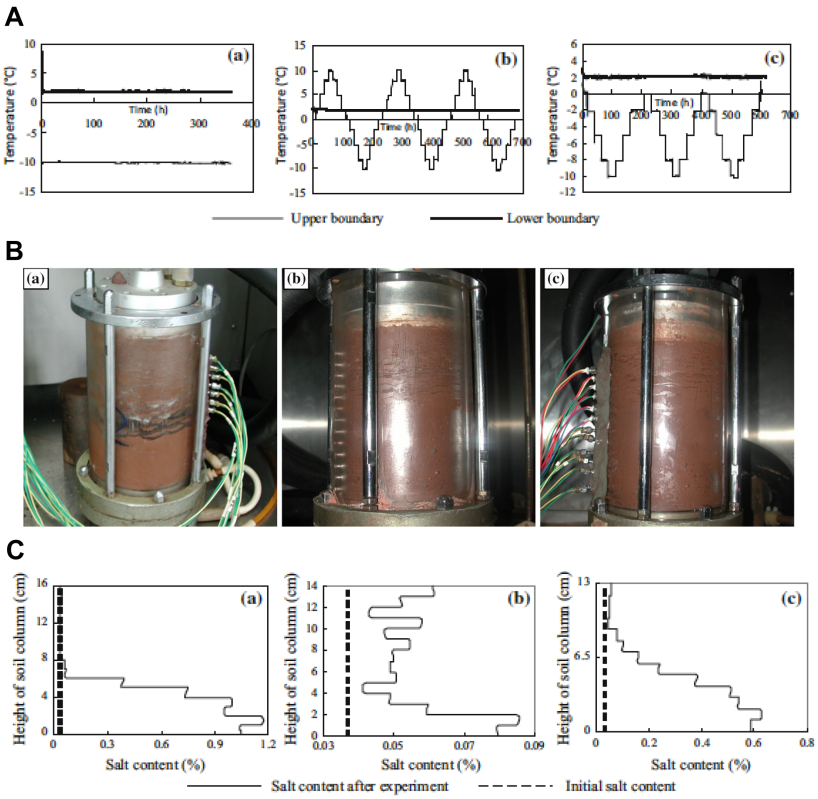

Figure 1.4 Column experiments by Bing et al. (2015) illustrating the salt content profiles (panel C) after (a) unidirectional freezing, (b) unidirectional cyclic freeze-thaw from −10°C to +10°C, and (c) unidirectional cyclic freeze-thaw from −10°C to 0°C (Images are taken from Bing et al. (2015)).

Luckily surface-wave methods remain effective when applied to saline permafrost. Different from reflection and refraction methods, surface-wave methods do not require abrupt velocity contrasts or positive velocity gradients to be applicable. Moreover, collecting high signal-to-noise ratio (S/N) surface-wave data does not require any special acquisition systems. Instead, the same systems used for reflection and refraction surveys are directly usable for surface-wave surveys. Therefore, surface-wave methods are used in the field-scale studies in this dissertation. Furthermore, surface waves having the largest amplitudes generally produce data with good signal-to-noise using low energy sources.

For laboratory studies, the temperature-sensitive nature of saline permafrost requires experimental methods that are accurate, reliable, and repeatable. In this dissertation, an ultrasonic pulse-transmission system was computer-automated to continuously acquire data at a fixed time interval (every 10 minutes). The freezing/thawing of the sediment samples was conducted inside of a temperature-controllable benchtop freezer that allows steady and uniform cooling/warming of the samples, and the temperatures of the samples were continuously monitored and recorded throughout the experiment. The controlled condition and dense data sampling enabled a systematic investigation on how seismic properties of saline permafrost vary with respect to temperatures and salinities. The resulting data therefore provide a solid foundation for examining the rock physics relationship between seismic properties and ice content.

1.4 The scope and structure of this dissertation

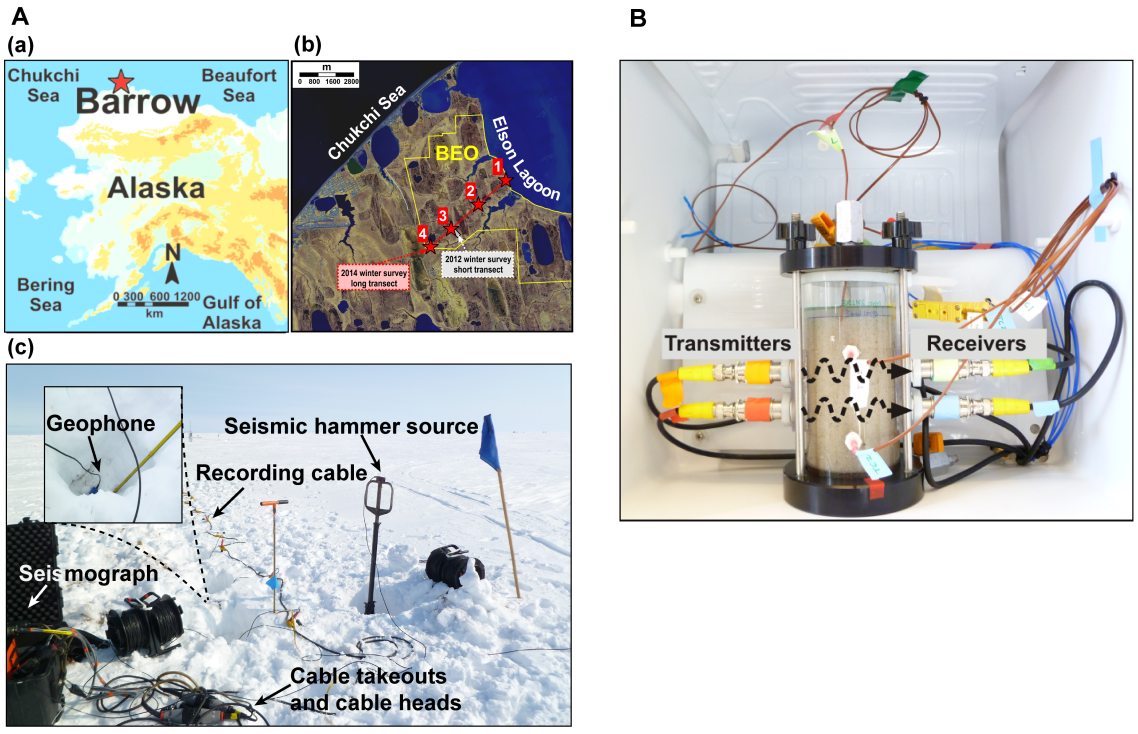

Figure 1.5 The basic setting of the field-scale studies (panel A) and lab-scale studies (panel B).

This dissertation has a total of six chapters. The core part comprises two field-scale studies and two lab-scale studies, each constituting a chapter:

- The two field-scale studies both center upon field sites in the Barrow Environmental Observatory (BEO), a 7,466-acre research reserve that is located at the northernmost part of the Alaskan Arctic Coastal Plain (Figure 1.5, panel A). The first study (Chapter 2; published as Dou and Ajo-Franklin (2014)) is based upon field data acquired in the winter of 2012. As a pilot study, it demonstrates the effectiveness of surface-wave methods in delineating velocity structures of permafrost. The results reveal that embedded saline permafrost is present along the seismic survey line and is likely to be pervasive across the entire BEO. The second study (Chapter 3) is based upon a follow-up field survey conducted in the winter of 2014. With the extended spatial coverage of the survey, the results of this study confirm the pervasiveness of saline permafrost across the entire BEO, and suggest that saline permafrost may cover a considerable portion of the Arctic Coastal Plain.
- The two lab-scale studies both center upon ultrasonic measurements obtained during controlled freezing/thawing of saturated, unconsolidated saline sediments (Figure 1.5, panel B). The first study (Chapter 4) presents the setup of the laboratory experiment and the characteristics of the ultrasonic data. The data illustrate the potent velocity reduction effect of the dissolved salts, the strong temperature sensitivity of the partially frozen sediments, and the unexpected attenuation that was particularly pronounced near the onset of freezing. The second study (Chapter 5) focuses on establishing a rock physics model that allows one to infer ice content from seismic velocities, and the experimental data presented in Chapter 4 were used as the reference for evaluating the quality of the model. An effective medium model was built by using a two-end-member mixing approach that does not involve ad hoc tunings of free-parameters. The good data fits suggest the utility of the model in inferring ice content from seismic velocities at the interpretation stages.

The final chapter (Chapter 6) summarizes the key points of this dissertation, the implications to permafrost studies, and some remaining questions that need to be addressed via future research.

2. Full-wavefield inversion of surface waves for mapping embedded low-velocity zones in permafrost

Published as: Dou, S., and J. Ajo-Franklin, 2014, Full-wavefield inversion of surface waves for mapping embedded low-velocity zones in permafrost: Geophysics, 79, no. 6, EN107-EN124, doi: 10.1190/geo2013-0427.1.

2.1 Introduction

Permafrost—defined as frozen ground that stays at or below 0 °C for at least two consecutive years—comprises 24% of the land in the northern circumpolar region (Jones et al. 2009). This vast permafrost-covered area houses approximately 50% of the terrestrial soil carbon pool (Zimov et al. 2006) and about 13% of the world's undiscovered, technically recoverable oil resource (Gautier et al. 2009). Knowledge of permafrost properties is thus essential both for ecosystem sustainability and future resource development. Nevertheless, permafrost is particularly difficult to study because it is largely invisible from the ground surface. Boreholes, although effective for subsurface characterization, are expensive, invasive, and are intrinsically point measurements. In contrast, geophysical approaches are cost-effective, mostly non-intrusive, and capable of resolving subsurface features at scales of tens to hundreds of meters laterally and vertically. Naturally, geophysical methods have been widely used to infer permafrost structures across various scales (see the review by Kneisel et al. (2008)).

Among the available geophysical approaches, seismic techniques have been used in a variety of studies for permafrost characterizations (e.g., Hauck and Kneisel 2008, Hilbich 2010, Justice and Zuba 1986, Miller et al. 2000, Ramachandran et al. 2011). Such research efforts are in especially high demand for seismic exploration in the Arctic regions: As permafrost is a near-surface structure that often overlays deeper oil-bearing strata, its presence can complicate processing and interpretation by generating severe traveltime distortions. Knowledge of permafrost structures is therefore essential for applying static corrections (e.g., Cox et al. 1999, Strobbia et al. 2009, Trupp et al. 2009). However, despite widespread interest, permafrost remains a challenging target for seismic investigations. Seismic delineation of permafrost structures might seem trivial at first glance, given the marked velocity contrast between frozen and unfrozen ground (e.g., Timur 1968, Zimmerman and King 1986). The challenges, however, come from the fact that seismic velocities in permafrost are primarily controlled by ground-ice content rather than lithology. In near-surface structures that are mainly controlled by lithology, it is often sufficient to assume a "layer-cake" earth model comprised of dry surface soil, wet overburden, weathered bedrock, and fresh bedrock. In this case, seismic velocities increase with depth, and thus commonly used seismic prospecting methods (e.g., refraction, reflection) are straightforward to apply. In contrast, although lithology does exert its influences, other factors such as thermal, chemical, and hydrological conditions can cause dramatic variations in ice/water content of permafrost; irregular distributions of ice and water in turn lead to complex seismic structures in permafrost. Because simple

layering and monotonically increasing velocities with depth seldom exist within permafrost, body waves (P- and S-waves) that travel through the body of the medium usually are "blind" to embedded low-velocity features. Therefore, commonly used seismic prospecting methods based upon refraction analysis are often unable to provide reliable information about permafrost structures (e.g., Barnes 1963, Trupp et al. 2009).

In contrast, surface-wave methods do not require abrupt velocity contrasts or normal velocity gradients (increasing velocities with depth), and thus they can be used for mapping irregular velocity structures in permafrost. Furthermore, collecting high S/N surface-wave data usually is straightforward by using the same acquisition systems as those for refraction and reflection methods. Motivated by the development of the Multichannel Analysis of Surface Waves (MASW) technique (Park et al. 1999, Xia et al. 1999), surface-wave methods have become widely accepted for applications in near-surface velocity characterizations (see the review by Socco et al. (2010)). In particular, recent studies have shown the potential of applying such methods to the Arctic regions (Ke et al. 2010, Strobbia et al. 2009).

Although surface-wave methods are a viable option for seismic mapping of permafrost structures, distinct challenges also exist. For instance, in areas with thin permafrost, the near-surface material resembles a velocity model with a fast top layer (Ke et al. 2010); in areas with thick permafrost, layers or zones of unfrozen ground could occur as low-velocity layers or pockets that are enclosed in a high velocity background (Strobbia et al. 2009, Trupp et al. 2009). The irregular velocity variations in permafrost, combined with the marked velocity contrasts between frozen and unfrozen materials, could render conventional surface-wave inversion methods inapplicable.

In this study, to investigate subsurface properties of permafrost, we applied dispersion analysis of surface waves to active-source seismic datasets collected along a series of off-end linear arrays at a site in the Arctic Coastal Plain near Barrow, Alaska. The surface-wave data exhibit inversely dispersive trends (i.e. phase velocities increase with increasing frequencies), for which conventional surface-wave inversion methods are inapplicable. As an alternative, we used a full-wavefield method equipped with a global-local hybrid optimization technique to infer the velocity structure. Inversion results reveal the presence of pronounced low-velocity zones with S-wave velocities in the 300–680 m/s range—70%–80% lower than the shallower permafrost units. The spatial extent of these low-velocity zones is also largely consistent with previously observed low electrical resistivity features. These results suggest the possible existence of saline zones within permafrost that are unfrozen or only partially frozen due to freezing-point depression effect of dissolved salts. This is a vivid example of the complex conditions in permafrost-affected ground, and the full-wavefield inversion of surface waves is an effective approach for quantitative delineation of permafrost.

2.2 Background

2.2.1 Field site description and data acquisition

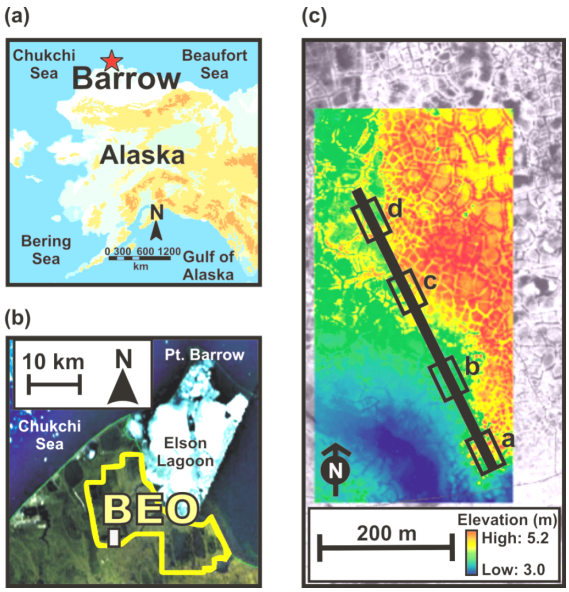

Figure 2.1 Maps of the study area near Barrow, Alaska: (a) The Barrow area within Alaska (red star). (b) The location of Barrow Environmental Observatory (BEO: yellow outline). The gray box indicates NGEE-Arctic geophysics study site. (c) The 475-meter-long seismic survey line (the black southeast-northwest trending line). Colored background is LiDAR (Light Detection And Ranging) measurement of the surface topography. The black boxes (a, b, c, and d) denote the spatial locations where our study focuses on.

Geological setting of the field site

The Barrow peninsula (70.9° N–71.5° N, 155.4° W–157.5° W) is located at the northern extremity of the Arctic Coastal Plain in Alaska. Bounded by the Chukchi and Beaufort Seas of the Arctic Ocean, this triangular-shaped land mass is approximately 530 km north of the Arctic Circle, which yields a polar climate with mean annual air temperatures as low as −12 °C. The entire area is underlain by continuous permafrost to depths of more than 300 m (Jorgenson et al. 2008), whereas the active layer (the topmost layer of soils that freeze and thaw seasonally) only reaches a thickness ranging from 30 cm to 90 cm (Hinkel and Nelson 2003). Soil cores from Barrow indicate that the upper permafrost is ice-rich, with volumetric ice content averaging 50%–75% in the upper 2 m (Sellmann et al. 1975). The parent materials of the soils are unconsolidated Quaternary sediments of Gubik Formation that consist largely of silt, fine-grained sand, and a small amount of clay and gravel (Black 1964, Williams and Carter 1984). The sediments are primarily of marine origin, resulting from repeated regression and transgression of the Arctic Ocean (Thurston et al. 1987). The top of the bedrock is commonly found in boreholes at depths of about 10–30 m below the land surface (Collins and Brewer 1961).

Active multichannel surface-wave survey

Our study area is within the Barrow Environmental Observatory (BEO)—a research reserve consisting of 7,466 acres of arctic tundra (Figure 2.1). As part of the Next-Generation Ecosystem Experiments project (NGEE-Arctic) initiated by the U.S. Department of Energy (DOE), we conducted a combined seismic refraction and surface-wave survey at the BEO site in May of 2012. During the time of data acquisition, the air

temperature remained below freezing and the active layer was completely frozen. We laid out 48 10-Hz vertical geophones in a linear array with 1.1-m receiver interval. Seismic data were acquired in a roll-along manner along a 475-m southeast-northwest trending survey line using a 14 kg (30 lbs) vertical sledgehammer source.

Note that with the vertical source and the vertical receivers, the type of surface waves we acquired are Rayleigh waves—a subset of surface-wave types. However, since the majority of literature on near-surface geophysics use "surface wave" rather than "Rayleigh wave", we use "surface wave" throughout the rest of this paper.

2.2.2 Representative synthetic examples of surface-wave dispersion

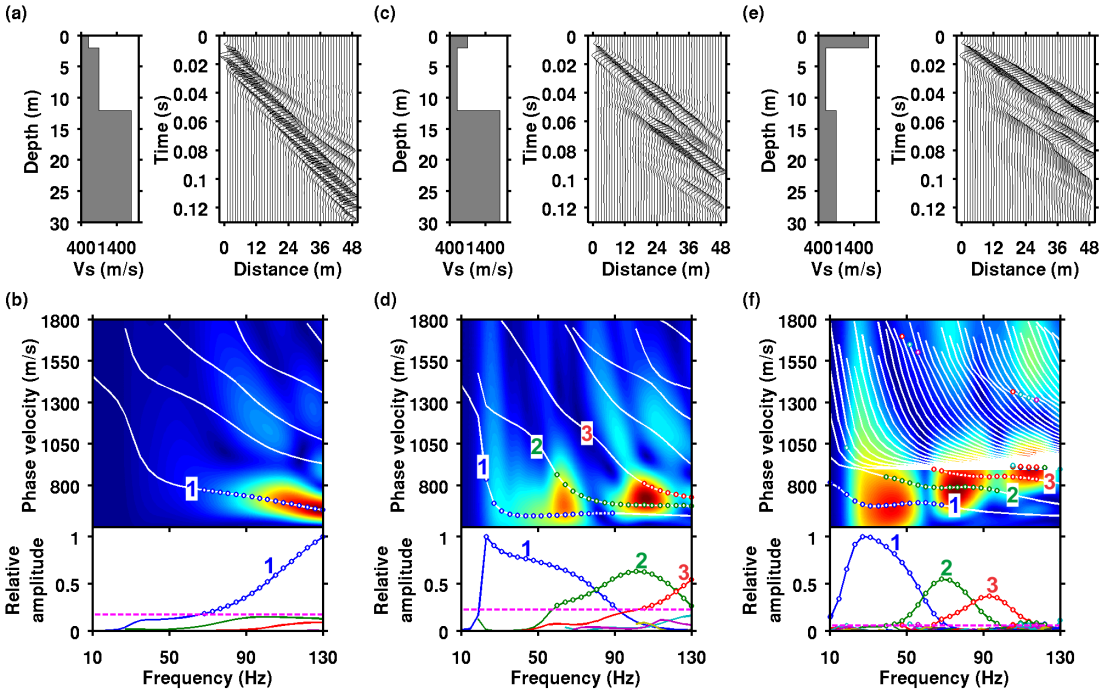

Figure 2.2 Three representative layered velocity models and the corresponding synthetic wavefields: Model 1, normally dispersive model ((a) and (b)); model 2, irregularly dispersive model with an embedded low-velocity layer ((c) and (d)); model 3, irregularly dispersive model with a high-velocity top layer ((e) and (f)). In (a), (c), and (e), the panel on the left shows the velocity structure of the model; the panel on the right shows the associated synthetic waveforms. In (b), (d), and (f), the pseudo-color image shows the dispersion spectrum. The superimposed white lines are the corresponding theoretical modal curves, and the colored lines are these modes' relative amplitudes (i.e., surface displacement distributions). A threshold in relative amplitudes for each velocity model is labeled by a magenta dashed line, denoting the threshold above which the mode amplitudes are strong enough to be present as spectral highlights. For each mode, the frequency range within which the relative amplitudes are above the threshold is denoted by open circles. The numeric labels 1, 2, and 3 denote the fundamental mode, the 1st overtone, the 2nd overtone, and the 3rd overtone, respectively.

Prior to the field data analysis, we consider a few synthetic examples that represent typical surface-wave dispersion patterns for near-surface (top 50–100 m) seismic investigations. As illustrated in Figure 2.2, model 1 (Figure 2.2a), in which S-wave velocity monotonically increases with depth, represents a normally dispersive medium; model 2 (Figure 2.2c) and 3 (Figure 2.2e), in which S-wave velocities do not monotonically increase with depth (i.e., velocity reversals are present), represent irregularly dispersive media. Between the two irregularly dispersive media, model 2 has an embedded low-velocity layer and the highest velocity exists in its half-space, whereas model 3 has the highest velocity in its topmost layer.

The model structure and the dispersion behavior of surface waves are mathematically connected by the Rayleigh secular equation, which represents an eigenvalue problem derived from the equation of motion and the associated boundary conditions (no traction at the free surface, and no traction and strain at infinite depth). Because a propagating surface wave train essentially is a superposition of its harmonic modes, the nontrivial eigenvalues of the Rayleigh secular equation are equivalent to the eigenfrequencies of the modes both in space (wavenumber k is the spatial frequency) and time (frequency f is the temporal frequency). The phase velocity of each mode $v(f)$ is obtained via $v(f) = 2\pi f/k$, and the kinematic attributes of the wavefield carried by each mode can be expressed as a set of (f, v) points called "modal curves".

While numerical modeling of modal curves can be achieved by searching for the nontrivial eigenvalues of the Rayleigh secular equation (i.e., the root-finding method), the measured modal curves (the dispersion curves) need to be extracted from dispersion spectra of the wavefield. The dispersion spectrum is generated by transforming the original wavefield in the offset-time (x-t) domain into the frequency-velocity (f-v) domain. It contains the complete signal content—comprised of kinematic and energy information—of the wavefield. For a normally dispersive medium, the dispersion spectrum usually has its energy concentrated along a smooth and continuous "ridge" (Figure 2.2b). This ridge corresponds to the fundamental mode that dominates the wavefield of the normally dispersive medium. A measured fundamental-mode dispersion curve can be extracted by picking the spectral maxima along the ridge, and its dispersion trend manifests that velocity decreases with frequency.

Although the fundamental mode dominates the wavefield of a normally dispersive medium, higher-order modes can become equally or more energetic in irregularly dispersive media. To examine energy distribution among the modes for the representative examples, theoretical modal curves (calculated by the root-finding method implemented in Herrmann (2004)) are superimposed on the corresponding dispersion spectra, and the associated amplitude responses of individual modes are displayed underneath each dispersion spectrum (Figure 2.2b, 2.2d, and 2.2f). For model 1 (Figure 2.2b), the fundamental mode is predominant, and different modal curves are distant from each other; the fundamental-mode energy form a continuous ridge. For model 2 (Figure 2.2d), at least three modes are strongly excited, and the modal curves are more closely spaced when compared with model 1; the multimodal energy distribution forms both "streaks" and "blobs", and the higher-order modes' energy are dominant. For model 3 (Figure 2.2f), multiple modes have strong amplitude responses, and a large number of closely-spaced modal curves are present; the discrete peaks of multimodal energy form an inversely dispersive trend, in which velocity appears to increase with frequency.

Note that the root-finding method, in principle, is only applicable to normally dispersive media. For an irregularly dispersive medium, the root-finding method still can be used to approximate the dispersion curves, but the layer configuration of the medium needs to simultaneously satisfy the following two conditions: (1) The half-space has the highest P- and S-wave velocity than all of the layers above; (2) The high-velocity layer within the velocity reversal section of the medium is adequately thin and thus it brings little influence on the long-period portions of the dispersion curves. Among the irregularly dispersive media shown in Figure 2.2 (model 2 and 3), model 2 satisfies both of these conditions; as to model 3, since its half-space does not have the highest velocity, an artificial basement whose P- and S-wave velocity are higher than those of model 3 is appended at great depth to make the root-finding method applicable, and the top of the basement is deep enough so that the associated reflections and refractions cannot contaminate the useful portion of the wavefield. This method of appending a high-velocity basement—sometimes referred to as "locked mode approximation" (Harvey 1981)—is useful for qualitative interpretations of the multimodal wavefield, but the quantitative accuracy of the dispersion curves is degraded to various extents.

Next, we take a closer look at the amplitude fluctuations in the dispersion spectra. When compared against amplitude responses of individual modes, it becomes evident that these fluctuations are attributable to a combination of the following factors:

1) Heterogeneous energy distribution along each individual mode: The energy distribution along a single mode is highly heterogeneous, and the modulations in energy depend strongly on the velocity structure. For instance, the fundamental mode shown in Figure 2.2 has distinctly different amplitude responses among the three different models; and the modulations in these amplitude responses accompany the variations of spectral amplitudes along the fundamental mode.
2) Uneven energy partitioning among modes and mode superposition: For a given velocity structure, energy partitioning is uneven among different modes, as shown by the different amplitude responses of individual modes in Figure 2.2b, 2.2d, and 2.2f. Moreover, when multiple modes are strongly excited, mode superposition exerts dominant control over amplitude fluctuations in the dispersion spectra. For example, in the multimodal dispersion spectra of model 2 and 3 (Figure 2.2d and 2.2f), the frequency ranges and the relative amplitudes of the spectral highlights are generally consistent with the overlaps in the modal amplitude responses, revealing strong correlations between spectral highlights and mode superposition.

In summary, the synthetic examples demonstrate striking differences in surface-wave dispersion between the normally dispersive and irregularly dispersive media. The patterns in dispersion spectra—including the dispersive trends and the fluctuations in spectral amplitudes—depend strongly on velocity structures. These three synthetic examples can be viewed as templates for identifying unusual dispersion trends observed in similar field datasets.

2.2.3 Field observations of surface-wave dispersion

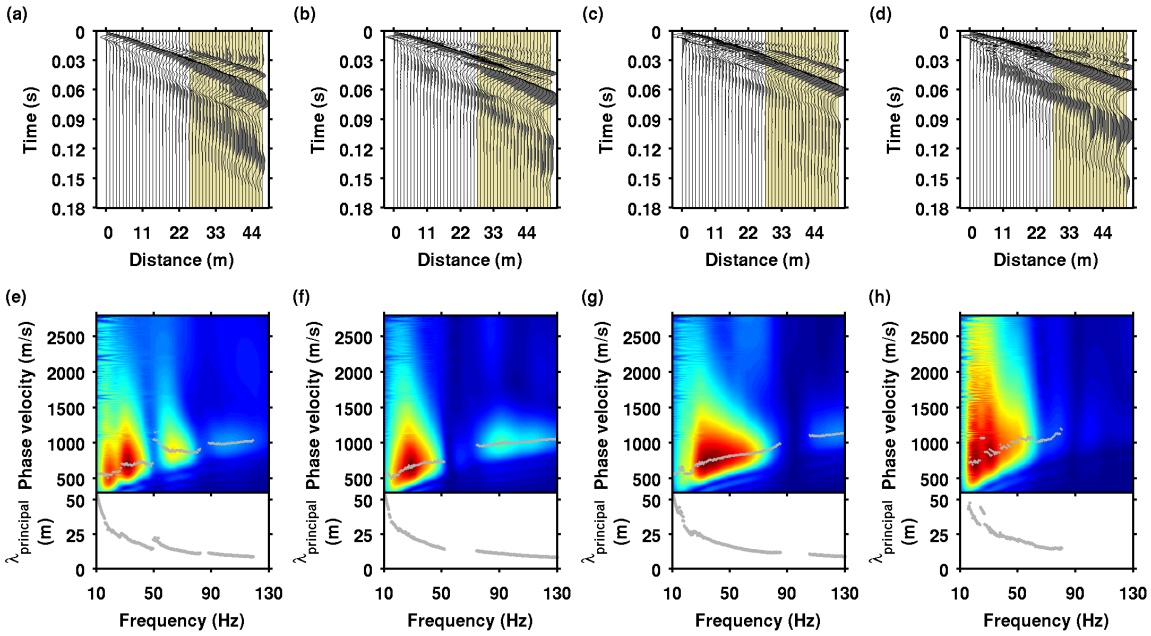

Figure 2.3 Displays of the field data: The upper panels (a), (b), (c), and (d) are time-domain shot gathers (band-pass filtered with a passband of 10–130 Hz). They correspond to locations a, b, c, and d in Figure 1c, respectively. The lower panels (e), (f), (g), and (h) show the associated dispersion spectra and the principal wavelength values derived from the (*f, v*) points of the spectral maxima ($\lambda_{principal} = v_{\text{maxima}} / f_{\text{maxima}}$). The light yellow patches in the upper panels show the range of the source-receiver offset (27.5–51.7 m) used for computing the dispersion spectra in the lower panels. The light gray dots superimposed on the dispersion spectra are the (*f*, *v*) points of the spectral maxima across the frequency ranges of the spectral highlights.

We now examine the field data acquired at the BEO site. Visual inspection of the time-domain shot gathers (Figure 2.3a, 2.3b, 2.3c, and 2.3d) reveals that the low-frequency components of the wave train (~10–40 Hz) take more time than the high-frequency components (~40–130 Hz) to arrive at the receivers. This suggests that low-frequency waves propagate at lower velocities. Because these low-frequency, long-wavelength waves penetrate deeper into the ground, the field site is likely to be irregularly dispersive with embedded low-velocity features.

Next, we apply an *f-k* transform to the field data to produce dispersion spectra. Zero padding is used to enhance the spectral resolution, and a Hanning taper is applied to repress artificial ripples caused by spectral leakage. As we can see from Figure 2.3e, 2.3f, 2.3g, and 2.3h, dispersion patterns generated from the field data are similar to the synthetic example with a high-velocity surficial layer (model 3; see the previous section)—the spectral highlights are a series of discrete peaks that show an inversely dispersive trend. Such similarity between the synthetic example and the field data has important implications: First, the field data contains dominant higher-order modes; second, the subsurface structure at the study site is inversely dispersive.

Through the dispersion analysis, the evidence points to the likely presence of embedded low-velocity features at the BEO site. Moreover, as shown in the dispersion

spectra (Figure 2.3e, 2.3f, 2.3g, and 2.3h), the phase velocity of the low-frequency waves (10–50 Hz) varies in the range of around 300–1000 m/s, which is substantially lower than literature values of ~1000–2000 m/s for frozen ground (Akimov 1973, Tsuji et al. 2012). Note that permafrost at the BEO site is expected to reach depths of more than 300 m (Jorgenson et al. 2008), which is much deeper than the maximum penetration depths of multichannel surface-wave surveys employing small impact sources.

2.2.4 Conventional inversion methods using dispersion curves

Conventional inversion methods seek models that can reproduce observed dispersion curves as closely as possible. The challenge in applying these methods to our field data is due to difficulties in the extraction and proper use of dispersion curves.

Depending upon how dispersion curves are retrieved during data processing and how they are used in the inversion, the conventional methods can be classified as modal-curve methods, modal-curve methods incorporating amplitude responses, and effective dispersion-curve techniques. Modal-curve methods require separation and identification of individual modes (e.g., Beaty et al. 2002, Xia et al. 2003). Although such methods are readily applicable for wavefields that are dominated by the fundamental mode, they are susceptible to mode misidentification problems when multiple modes are present (Zhang and Chan 2003). To reduce the risk of mode misidentification, modal-curve methods incorporating amplitude responses use modal amplitude responses to aid in identifying individual modes. This method facilitates inversion for irregularly dispersive media (Hayashi 2012, Ikeda et al. 2012, Lu and Zhang 2006, Lu et al. 2007); a highly relevant example is the study of Tsuji et al. (2012) that identifies unfrozen zones enclosed in glacial sediments by using this method. However, two limitations are worth noting: First, this technique becomes inapplicable in situations where modal curves cannot be unambiguously separated; second, it does not consider the effect of data acquisition and processing procedures, even though these factors affect the modal amplitudes measured from dispersion spectra. The last method, the effective dispersion-curve method, does not require mode identification. The spectral maxima of a dispersion spectrum at each frequency are combined into an effective dispersion curve, and then the inversion looks for models that can reproduce this observed effective curve (e.g., O'Neill et al. 2003). The method avoids mode identification and includes the effects of data acquisition and processing, but it does not fully use energy distributions of the dispersion spectra and thus relies primarily upon the kinematic characteristics of surface-wave datasets.

Whereas all the methods mentioned so far require explicit matching of observed and model-predicted dispersion curves (modal curves or effective curves) in the inversion, Maraschini et al. (2010) proposed an implicit fitting procedure for multimodal dispersion curves (referred to as Maraschini method herein). This method requires the picking of a set of multimodal dispersion curves (rather than one effective curve), but eliminates the need for assigning mode numbers to individual curves—by virtue of a novel form of the misfit function that is based upon the determinant of the Haskell-Thomson matrix: For a given model, its modal curves essentially are a set of (f, v) points at which the determinant of the Haskell-Thomson matrix goes to zero; conversely, in the Maraschini method, the inversion solves for models that can minimize the same determinant at the observed (f, v) points (i.e., all the points on the picked multimodal dispersion curves). Because the computational cost is low and no mode identification is needed, the Maraschini method has shown promise in a variety of engineering and exploration

applications (e.g., Bergamo et al. 2011, Boiero et al. 2013, Maraschini and Foti 2010). However, while mode numbering is avoided, the method still heavily relies on accurate picking of dispersion curves; and hence it becomes inapplicable when mode superposition is severe and spectral resolution is limited.

In addition to dominant higher-order modes, leaky modes further complicate the dispersion analysis and inversion for irregularly dispersive media. Velocity reversals form imperfect wave guides, where some energy in the guided modes escape across layer boundaries and convert to other modes—hence the name leaky modes (Sheriff 2002). Physically, leaky modes cause additional modulations in the energy distributions of the wavefield. Numerically, leaky modes correspond to complex roots of the Rayleigh secular equation. Most of the existing root-finding methods for calculating dispersion curves cannot handle leaky modes directly, unless numerical approximations are applied at costs of accuracy (O'Neill and Matsuoka 2005, Pan et al. 2013). One exception that we are aware of is the approach of Pavlakovic et al. (1997), which traces most of dispersion curves in the complex wavenumber domain. It has been used to calculate theoretical dispersion curves for nondestructive testing of pavements—an inversely-dispersive medium commonly encountered in practice (Ryden and Lowe 2004, Ryden and Park 2004). Although calculating theoretical modal curves in the complex wavenumber domain can better capture the effect of leaky modes in the modeling step, difficulties in the accurate extraction of observed dispersion curves remain the major roadblock for dispersion-curve-based methods (Ryden and Park 2006).

To summarize, when applied to multimodal wavefields, the limitations of the dispersion-curve-based inversion methods stem from their reliance on the kinematic characteristics of the surface-wave propagation. For irregularly dispersive media, however, the energy distribution (including the effects of higher-order modes, leaky modes, and the data acquisition and processing procedure), in addition to the kinematic information, is crucial for the inversion of the multimodal surface-wave data. Therefore, we must consider applying alternative inversion methods to our field data.

2.2.5 Full-wavefield inversion methods using dispersion spectra

Full-wavefield methods using dispersion spectra are able to exploit the complete signal content of surface waves while avoiding mode identification requirements (Forbriger 2003a, 2003b, Ryden and Park 2006). Hence, we use a full-wavefield method for the inversion of our field data, and we will present the details in the next section.

2.3 Method

2.3.1 A general procedure for full-wavefield inversion of surface waves

Our inversion strategy utilizes a derivative-free global-local search scheme to select a model that minimizes a full-wavefield objective function. The objective function is based upon the misfit between the observed and the model-predicted dispersion spectra, and the model is parameterized as a small number of horizontal layers overlying a half-space. The small dimensionality of the resulting problem allows this combination of an expensive objective function and the global-local search scheme to converge at reasonable computational costs. In this section, we describe the formula of the objective function, the hybrid search scheme, the forward modeling procedure, and the model parameterization.

Objective function: dispersion spectra misfit

The objective function takes the form of the root-mean-square deviation (RMSD):

$$M(\mathbf{m}) = \sqrt{\frac{\sum_{i=1}^{N_f}\sum_{j=1}^{N_v}\left(S_{ij} - O_{ij}\right)^2}{N_f N_v}} \quad (2.1)$$

where model parameters such as layer thicknesses and S-wave velocities are the elements of the model vector **m**; M represents the RMSD that measures the overall size of the misfit between the synthetic dispersion spectrum (S) for an estimated model **m** and the observed counterpart (O); N_f is the number of sampling points along the f axis (frequency) of the dispersion spectrum, and N_v is the number of sampling points along the v axis (velocity) of the dispersion spectrum. Note that we apply a global normalization to both the synthetic and the observed dispersion spectrum—that is, each dispersion spectrum is normalized by its maximum spectral amplitude. In this way, relative amplitudes of the dispersion spectra are preserved (no trace normalization is applied), so that the energy partitioning across the multimodal wavefield is used in the inversion. An important observation is that the evaluation of M requires a full-wavefield modeling operation (S); this step is responsible for the large computational cost of our inversion approach.

Optimization techniques: derivative-free global-local hybrid method

The inversion procedure can be posed as a bound-constrained optimization problem, for which we seek the optimal model **m** that minimizes the multivariable objective function $M(\mathbf{m})$:

Minimize $\quad M(\mathbf{m}); \quad [\mathbf{m}]_n = \{m_i\}$

Subject to $\quad m_i^{(l)} \le m_i \le m_i^{(u)}, \qquad i = 1, 2, \ldots, n$

where $m_i^{(l)}$ and $m_i^{(u)}$ denote the lower and upper bound of the search region for each model parameter, respectively. Because the inverse problem is nonlinear, its objective function usually has multiple local minima rather than a single well-defined global minimum (Mueller and Siltanen 2012, Snieder 1998); and the topography of the objective-function hypersurface may be rugged or even include discontinuities. Moreover, the partial derivatives of the objective function with respect to the model parameters are not analytically available. Consequently, many commonly used algorithms that require derivative information (e.g., gradient descent and Newton's method) are inapplicable for this study.

To avoid the limitations described above, we utilize derivative-free approaches that only require evaluations of the objective function. Among the commonly used derivative-free methods, stochastic global-search algorithms are widely applied in surface-wave literature, including Monte Carlo methods (Maraschini and Foti 2010, Socco and Boiero 2008), Genetic Algorithms (Hayashi 2012, Ikeda et al. 2012, Lu and Zhang 2006, Lu et al. 2007, Tsuji et al. 2012), Simulated Annealing (Beaty et al. 2002, Ryden and Park 2006), and the Neighborhood Algorithm (Douma and Haney 2013, Wathelet et al. 2004). By contrast, the use of deterministic algorithms is not yet as common among surface-wave applications. Nevertheless, different from most stochastic algorithms, the performance of deterministic algorithms usually have a weaker

dependence on the fine-tuning of the algorithmic parameters; the use of deterministic algorithms thus deserves further exploration for surface-wave inversion. In this study, we investigate two deterministic algorithms for the inversion of our field data; and we combine these two algorithms sequentially into a global-local hybrid approach to take advantage of their individual strengths.

Hybrid "Global + Local" method.—This optimization approach begins with the application of the Multilevel Coordinate Search (MCS) algorithm (Huyer and Neumaier 1999), whose main function is to move the search towards globally optimal regions. We use a MATLAB implementation of the algorithm developed by Neumaier (2000). MCS is a largely direct method that searches for a global minimum by recursively splitting the search space into smaller sub-regions. The level *s*, which is a rough measure of the number of times a sub-region has been processed, guides a multilevel search that balances global exploration (splitting sub-regions with large unexplored territory) and local exploitation (splitting sub-regions with good objective function values). MCS also includes an optional local-search enhancement that uses surrogate models to approximate local features (i.e., model-based local search). Although this enhancement is designed to accelerate convergence, its effect in many applications is the opposite (Pošík et al. 2012): the local-search enhancement can be so slow that the maximum allowable number of function calls often is reached before a satisfactory optimum is found. Therefore, we choose to neglect this option in MCS. Instead, we use a secondary direct-search method as the local-search enhancement to improve the solution returned by MCS.

Direct local-search enhancement.—The Nelder-Mead (NM) downhill simplex method is applied as an additional local-search enhancement to improve the solution obtained from MCS. The NM solver used in this study is *fminsearch* from the MATLAB Optimization Toolbox. The NM method, first introduced by Nelder and Mead (1965), is a direct local-search method. To minimize an n-dimensional objective function, the NM method starts with a simplex (an n-dimensional convex hull bounded by (n−1)-dimensional hyperplanes and defined by n + 1 linearly independent vertexes) constructed around a given initial "guess" (e.g., $[\mathbf{m_0}]_n$). At each iteration, the objective function values are computed at the vertexes of the simplex, and the worst vertex (with the highest objective function value among the current vertexes) is found. Next, the NM method tries to replace the worst vertex by a better point to create a new simplex. Candidate replacement points are obtained by transforming the worst vertex through reflection, expansion, or contraction about the centroid of the current simplex. In this way, the NM algorithm continues to move downhill towards a local minimum. An excellent description of the NM method can be found in Press et al. (1992).

As with all local-search methods, the NM method requires a good starting model to converge toward the global optimum. By using MCS and NM in series, the MCS method provides a good starting model for the NM method—a so-called "hot start" procedure, which improves the overall efficiency and accuracy of the optimization process. In the rest of this paper, we use the phrase "MCS-NM hybrid method" as the name of the optimization techniques (Appendix A2 contains a list of the key parameters used in the optimization).

Forward modeling of the wavefield and parsimonious model parameterization

Forward modeling of the wavefield is a two-step procedure: A synthetic shot gather is first generated for a given model using the same acquisition geometry as the

field data; the shot gather is then transformed into a dispersion spectrum. Because the computation of the synthetic shot gather is time-consuming, and the number of model parameters needs to be relatively small for the selected optimization method, we adopt a parsimonious parameterization of the velocity structure that is represented as a horizontally layered elastic model. Although viscoelastic media are likely to be more realistic representations of the subsurface, elastic models are used to avoid increasing the problem dimension. The validity of using elastic inversion will be addressed in a later section.

2.3.2 Specific settings for the field-data application

Key parameters determined from the observed dispersion spectra: the optimal f-v window and the investigation depths

To apply the full-wavefield inversion to the field data, we first need to tailor the setup of the inversion according to some key parameters that are determined from the observed dispersion spectra—namely, the spectral range of the usable field-data signals, which dictates the optimal *f-v* window used for evaluating the objective function (Equation 2.1); and the range of investigation depths allowed for the field data, which serves as prior information for the model parameterization. This section provides details about these key parameters.

First, based upon the dominant energy distributions of the observed dispersion spectra, we select the optimal *f-v* window used in the inversion: The frequency range is 10–130 Hz, and the velocity range is 300–2800 m/s (Figure 2.3).

Next, in preparation for assessing the investigation depths allowed for the field data, we estimate the range of resolvable wavelengths using three criteria: the signal content of the dispersion spectra, the spatial sampling of the acquisition geometry, and the principal wavelengths associated with the spectral maxima. The signal content of the dispersion spectra, bounded by the optimal *f-v* window, allows us to make a first-order estimate of the range of the detectable wavelengths, which is ~2–200 m ($\lambda_{\min} = v_{\min} / f_{\max}$; $\lambda_{\max} = v_{\max} / f_{\min}$). Within this range, however, only a subset of the wavelengths is practically resolvable, owing to the limited spatial sampling that is dictated by the acquisition geometry: Receiver spacing (Δx) of 1.1 m yields a minimum resolvable wavelength ($\lambda_{\min} \approx \lambda_{Nyquist} = 2\Delta x$) of ~2 m; and the total array length determines a maximum resolvable wavelength ($\lambda_{\max} \approx x_{\max}$) of ~50 m. In addition, the principal wavelengths of the wavefield—estimated based upon the (*f*, *v*) points of spectral maxima by using $\lambda_{principal} = v_{\max ima} / f_{\max ima}$—also provide complementary constraints for the range of the resolvable wavelengths. As shown in Figure 2.3e, 2.3f, 2.3g, and 2.3h, the maximum value of the principal wavelengths is around 50 m, which is consistent with the maximum resolvable wavelength dictated by the array length. In short, the range of the resolvable wavelengths is ~2–50 m.

Then, by following the one-half wavelength rule-of-thumb, we can assess the range of investigation depths based upon the range of the resolvable wavelengths: Assuming a scaling factor of 1/2 between the resolvable wavelengths and the associated resolvable depths (defined as the depth at which V_S can be resolved with reasonable accuracy) (Park et al. 1999, Rix and Leipski 1991), the range of the investigation depths

is ~1–25 m. Note that such rules are primarily applicable to fundamental-mode surface waves. By comparison, higher-order modes have stronger sensitivity to deeper units than the fundamental mode of the same wavelength (Xia et al. 2003); and hence, the maximum investigation depth for our field data may extend deeper, especially for detecting the strong contrast between frozen and unfrozen strata.

Forward modeling of the full wavefield: the source wavelet and the Green's function

In this study, the zero-offset trace of each shot gather is used as an empirical source wavelet. Strictly speaking, the zero-offset trace itself already is the convolution of the true source wavelet and the Green's function. Nevertheless, because the Green's function is not known prior to the inversion, the true source wavelet cannot be effectively retrieved. Despite this limitation, the zero-offset trace performs well as the source wavelet, especially in providing the appropriate frequency content and wave shapes for the model-predicted wavefield.

For each shot gather, the Green's functions in response to a vertical point force (mimicking the sledge hammer impact) are generated by the wavenumber integration method (also referred to as reflectivity method or discrete wavenumber method in seismology literature) (Herrmann 2004), which is a full-wavefield technique applicable to horizontally layered media. In the end, to complete the wavefield computation, the Green's function is convolved with the source wavelet to produce a synthetic shot gather.

Parsimonious model parameterization: two layer over a half-space elastic model

We adopt an elastic model comprising two uniform layers over a half-space for a parsimonious subsurface representation. Besides computational efficiency considerations, the rationales for this parameterization also come from characteristics of the wavefield and prior knowledge of the subsurface structure.

The horizontally layered model is a reasonable abstraction of the subsurface because of the characteristics of the observed wavefield. Surface waves are primarily sensitive to average velocity structures underneath the source and the receiver array. This assumption may not be valid when marked lateral variations or heterogeneities are present, as surface waves could be back-propagated by lateral velocity variations or backscattered by short-wavelength heterogeneities (e.g., Yilmaz and Kocaoglu 2012). In the recorded data, these back-propagation and back-scattering could in turn manifest themselves as wavefield distortions that carry the signatures of the localized variations and heterogeneities. The field data in the frequency range of 10–130 Hz, however, do not show such distortions in either *x-t* or *f-k* domain. Although lateral variations and heterogeneities inherently exist in the subsurface, the horizontally layered model is a justifiable simplification of the velocity structures concerning the inversion of our field data. Prior knowledge is a combination of geological and geophysical information. Geological prior information come from existing studies examining soil cores from Barrow, which suggest an ice-rich uppermost layer. Geophysical prior information are derived from the results of an electrical resistivity tomography (ERT) profile along the same survey line, which can be simplified as two-layer structure consisting of a high electrical resistivity layer at the top (> 2,500 ohm-m; thickness varies from 0.5 to more than 5 m) and an underlying low electrical resistivity layer (as low as ~10 ohm-m) (Hubbard et al. 2013). In this way, the two layers in the seismic velocity structure correspond to the high and the low electrical resistivity features. However, ERT loses

resolution for structures deeper than 6 m below the surface because of its limited depth penetration in this particular case (B. Dafflon, personal communication, 2012), whereas the seismic surface waves used in this study allow a maximum investigation depth of at least 25 m (detailed in an earlier section titled "Key parameters determined from the observed dispersion spectra: the optimal *f*-*v* window and the investigation depths"). For the purpose of increasing the depth extent of the geophysical investigation, as well as providing independent information for the subsurface characterization, the seismic velocity model includes a half-space beneath the two-layer structure.

2.4 Synthetic tests

To test the validity of our full-wavefield inversion approach, we conduct a series of tests using synthetic data generated from a reference model. The main objectives of the synthetic experiment are to determine model parameters for the inversion based upon the results of the sensitivity analysis; and to examine the performance of the MCS-NM hybrid method.

2.4.1 The reference model and its wavefield

We use a two layer over a half-space model shown in Table 2.1 as the reference model. Note that we specifically design this model to be irregularly dispersive. In order to match the frequency content of the synthetic data with that of the field data, we use one of the empirical source wavelets (with a centroid frequency of 68 Hz and a half-peak bandwidth of 13−82 Hz) obtained from the field data as the source wavelet for the synthetic tests. We then convolve this source wavelet with the Green's function of the reference model to construct the reference wavefield.

2.4.2 Sensitivity analysis of the model parameters

To determine how many model parameters should be used and which parameters are significant, we first examine the objective function's sensitivity to different model parameters. Considering only the elastic properties, we begin with eight candidate model parameters h_1, V_{S1}, V_{P1}/V_{S1}, h_2, V_{S2}, V_{P2}/V_{S2}, V_{S3}, and V_{P3}/V_{S3} (where h denotes the layer thickness, V_P denotes P-wave velocity, V_S denotes S-wave velocity; and the subscripts 1, 2, and 3 denote the top layer, the middle layer, and the half-space, respectively), and examine their contributions to the objective function.

We first look into the influence of each candidate model parameter by examining 1D cross sections of the objective function (Equation 2.1). We perturb each of the model parameters by ±50% relative to its reference value while keeping the remainder of the seven parameters fixed. The results are shown in Figure 2.4. In each of the 1D cross sections, the depth and sharpness of the "valley" is proportional to the sensitivity of the corresponding model parameter. Three observations can be extracted from this synthetic test: First, the asymmetric shape of each "valley" and the varying depths of these 1D cross sections suggest that different parameters contribute differently to the objective function; second, many of these 1D cross sections contain "quasi-plateaus"—flat portions of the objection function that are nearly insensitive to perturbations in model parameters (e.g., the nearly flat portions of the 1D cross section in Figure 2.4b, 2.4f, 2.4g, and 2.4h), suggesting the ill-posed nature of the inverse problem; third, V_{P3}/V_{S3} (the V_P/V_S ratio of the half-space) is the least sensitive parameter among all the candidate model parameters,

and thus it is not used in the inversion. The number of candidate model parameters is now reduced to seven (h_1, V_{S1}, V_{P1}/V_{S1}, h_2, V_{S2}, V_{P2}/V_{S2}, and V_{S3}).

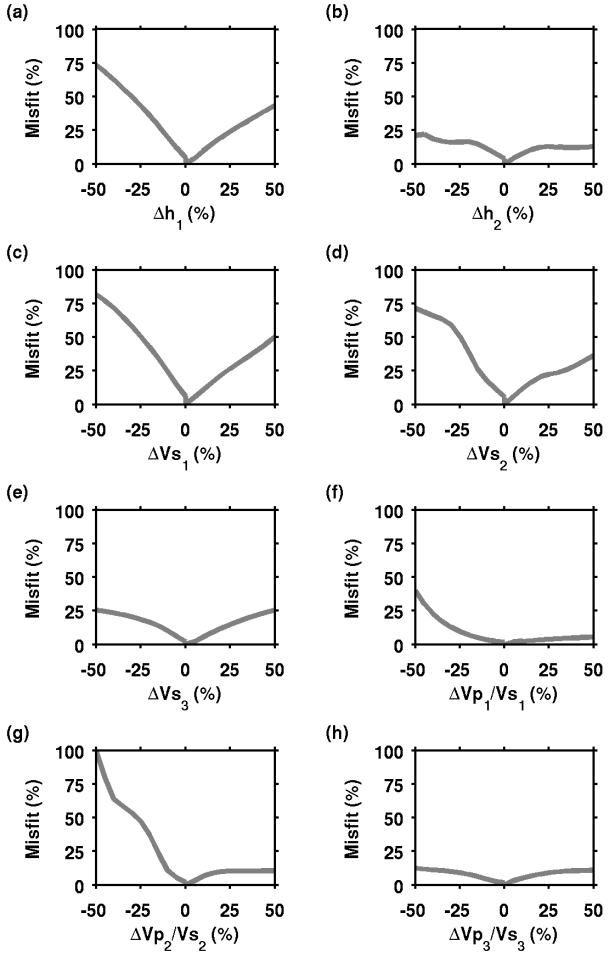

Figure 2.4 1D cross sections of the objective function $M(\mathbf{m})$ (Equation 2.1). The vertical axes correspond to normalized misfit. The horizontal axes correspond to relative parameter perturbations in the range of ±50% with respect to the reference values (zero values correspond to reference values in Table 2.1).

We then examine 2D cross sections of the objective function to learn more about the characteristics of the inverse problem. We group model parameters into pairs and simultaneously perturb each parameter pair by ±45% relative to the reference value while keeping the other five parameters fixed. Results obtained from six of these parameter pairs are shown in Figure 2.5. Three characteristics of the inverse problems are illustrated by this test: First, "quasi-plateaus" are present in these 2D cross sections (e.g., the nearly flat portions of the 2D cross section in Figure 2.5d and 2.5e), again suggesting that the inverse problem is ill-posed; second, the objective function has local minima, which indicates the necessity of using global-search methods for the inversion; third, the model parameters are correlated (e.g., the curved valley in Figure 2.5a) and thus the inverse problem is inseparable.

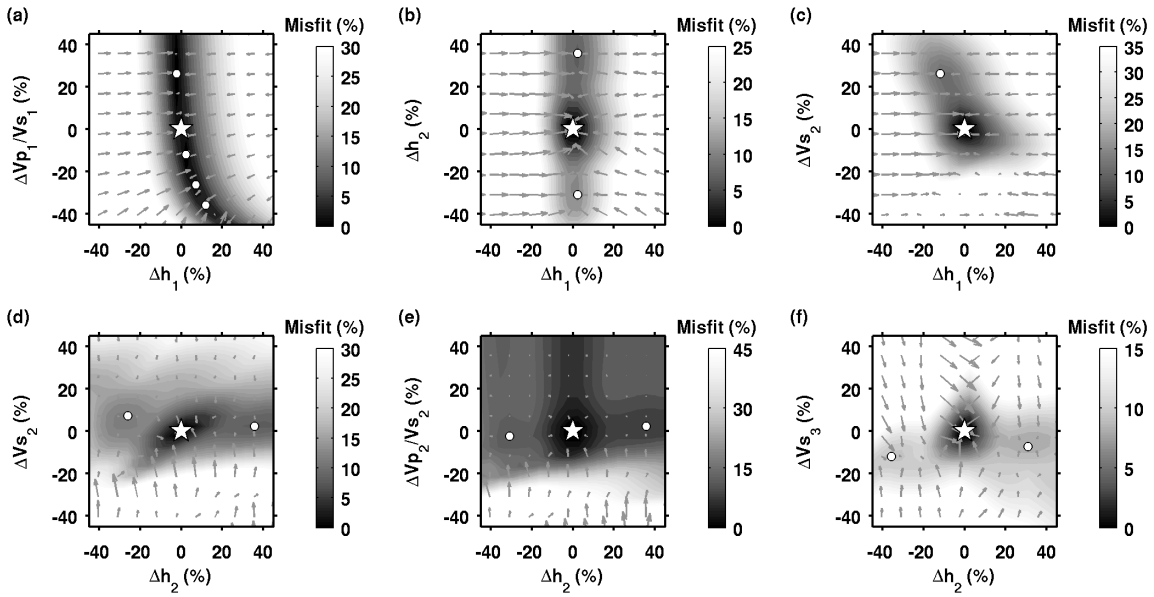

Figure 2.5 2D cross sections of the objective function $M(\mathbf{m})$ (Equation 2.1). The horizontal and vertical axes correspond to relative parameter perturbations in the range of ±45% with respect to the reference values shown in Table 2.1. The varying shades of gray represent the values of the misfit function. The color scale is clipped at 40% of the maximum misfit-function value for each cross section. Grey vectors indicate the gradient of the objective function with their lengths and directions. Valleys and local minima (labeled with white dots) are visible. The global minima are marked by white stars.

Although examining the objective functions within a higher dimensional context could provide more information, it is both difficult to visualize and expensive to compute. 1D and 2D cross sections of the objective function, though incomplete, already provide enough knowledge for us to make decisions on what model parameters to use in the inversion.

Among the seven candidate model parameters, we can eliminate one more parameter: Because we can use first arrivals of the field data to determine the P-wave velocity of the top layer (V_{P1}), we do not directly invert for V_{S1}. Instead, we invert for V_{P1}/V_{S1}, and from there, we then obtain V_{S1} by using the relation $V_{S1} = V_{P1}/(V_{P1}/V_{S1})$.

To summarize, the sensitivity analysis helps us to make the decision on model parameters that will be inverted for: They are six parameters consisting of h_1, V_{P1}/V_{S1}, h_2, V_{S2}, V_{P2}/V_{S2}, and V_{S3}.

2.4.3 Performance test of the full-wavefield method

To examine the performance of the MCS-NM hybrid method (MCS = Multilevel Coordinate Search method; NM = Nelder-Mead downhill simplex method), we conduct full-wavefield inversion using the dispersion spectrum of the reference model (Table 2.1) as the synthetic data. We first launch the MCS solver starting from search bounds shown in Table 2.2. After 327 iterations, MCS converges to an optimum with 70% of misfit reduction. Then, starting from the MCS solutions, we use the NM solver for the local-search enhancement. After 361 additional iterations, we successfully obtain the globally optimal solutions with the NM solver (Table 2.1). The entire inversion procedure takes

approximately 2.5 hours (wall-clock time) on a Linux workstation equipped with a quad-core 3.07 GHz Intel Xeon processor. The iteration history of the MCS-NM hybrid method is shown in 2.6a. The convergence improvement generated by the NM local-search enhancement is evident.

Table 2.1 Reference two layer over a half-space elastic model.

Layer index	h (m)	V_S (m/s)	V_P/V_S
1	2.5 (2.5010)	2300.0	2.8 (2.8007)
2	10.0 (9.9969)	560.0 (559.8657)	4.0 (4.0011)
3	∞	670.0 (669.9601)	4.0

Parameter values obtained from the inversion are given in parentheses.
The density of all of the layers is fixed at 2000.0 kg/m^3 throughout the test.

Table 2.2 Search bounds of MCS for the synthetic experiment.

Model parameters m	**Lower bound $\mathbf{m^{(l)}}$**	**Upper bound $\mathbf{m^{(u)}}$**
h_1 (m)	1.0	5.0
V_{P1}/V_{S1}	1.4	4.0
h_2 (m)	2.0	20.0
V_{S2} (m/s)	300.0	2000.0
V_{P2}/V_{S2}	1.4	5.0
V_{S3} (m/s)	300.0	2000.0

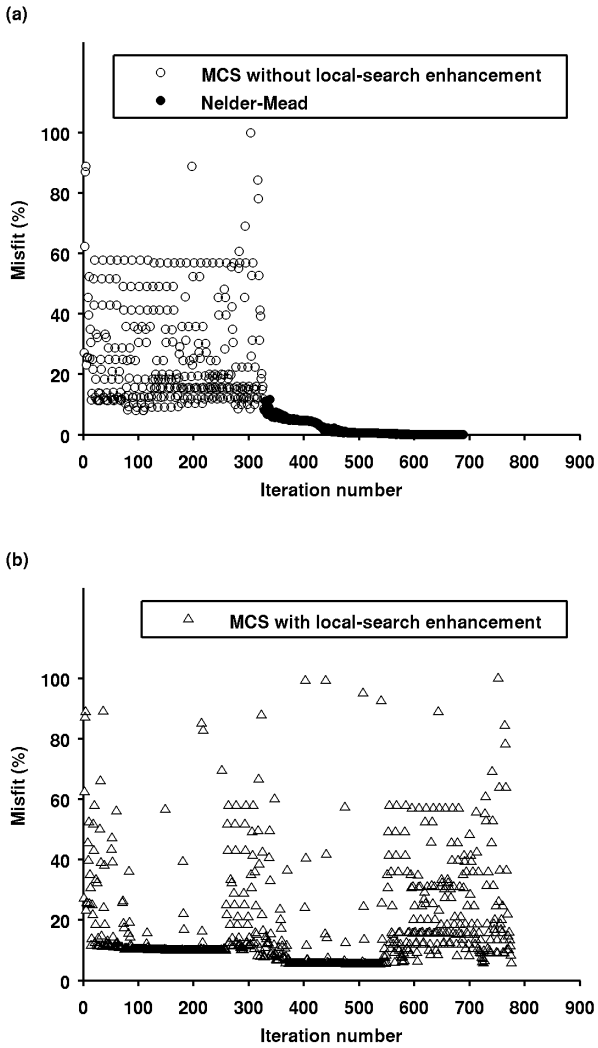

Figure 2.6 Performance comparison between the MCS-NM hybrid method and the MCS method with local-search enhancement: (a) iteration history of the MCS-NM hybrid method; (b) iteration history of the MCS method with local-search enhancement (maximum allowable number of iterations is set as 5).

To gain insight into the performance of the optional local-search enhancement in MCS, we also conduct an additional inversion run with the same search bounds but using MCS with local-search enhancement rather than the MCS-NM hybrid method. To avoid excessively long runtime spent in the local-search enhancement step, we use a strong constraint on the local-search parameter (the maximum number of local searches is set as 5). Even with this constraint, MCS still spends a large number of iterations on the local search. After 776 iterations, which is 88 iterations more than the total number of iterations used by the MCS-NM hybrid method, MCS still does not converge to an optimum of the same quality as the one obtained from the MCS-NM hybrid method (Figure 2.6b).

In summary, the results of the synthetic experiment indicate the validity of the full-wavefield method, and that the use of the MCS-NM hybrid method brings marked improvements to the optimization procedure.

2.4.4 Effects of noise and attenuation on the full-wavefield inversion

In contrast to the error-free synthetic example shown above, inversion of field data is always subjected to both data errors and model errors. Data errors can be introduced from a variety of sources, including both random (e.g., wind, electrical spikes) and coherent noise (e.g., scattering from lateral heterogeneity) sources. Model errors occur when the model parameterization, owing to its simplicity, is insufficient for describing a subsurface that is inherently complex and heterogeneous. Because both data and model errors are inevitable in real inversion, we need to test the robustness and validity of the full-wavefield method in the presence of these errors. For this purpose, we conduct a series of synthetic tests to examine the effects of random noise—one representation for data errors, as well as possible biases introduced by neglecting viscoelastic attenuation—a probable source of model errors, on the full-wavefield inversion.

Effects of random noise

The synthetic example described previously shows the best attainable results because the data are noise-free. To examine whether the inversion is robust in the presence of noise, we carry out a series of tests using the same reference model as what is used in the noise-free test (Table 2.1): We first generate two sets of noisy synthetic data by adding 20% and 45% Gaussian noise to the noise-free synthetic data, for which the two noise levels are chosen to be comparable to and worse than that of the field data, respectively (Figure 2.7). We then invert these two sets of noisy data using the full-wavefield method. Model parameters inverted from these noisy data (Table 2.3) show slight deviations from the reference values—as expected in the presence of noise contamination. However, the amount of deviation is very low (no larger than 4.8%), which demonstrates the robustness of the method in the presence of Gaussian random noise.

Table 2.3 Model parameters inverted from noisy synthetic data.

Model parameters **m**	Inverted model from noisy data (20% Gaussian noise)	Inverted model from noisy data (45% Gaussian noise)
h_1 (m) [2.5]	2.5099	2.4530
V_{P1}/V_{S1} [2.8]	2.8557	2.7638
h_2 (m) [10.0]	10.2122	10.4834
V_{S2} (m/s) [560.0]	570.4122	578.5332
V_{P2}/V_{S2} [4.0]	3.8893	4.0638
V_{S3} (m/s) [670.0]	680.2520	684.3838

Parameter values of the reference model are given in square parentheses.

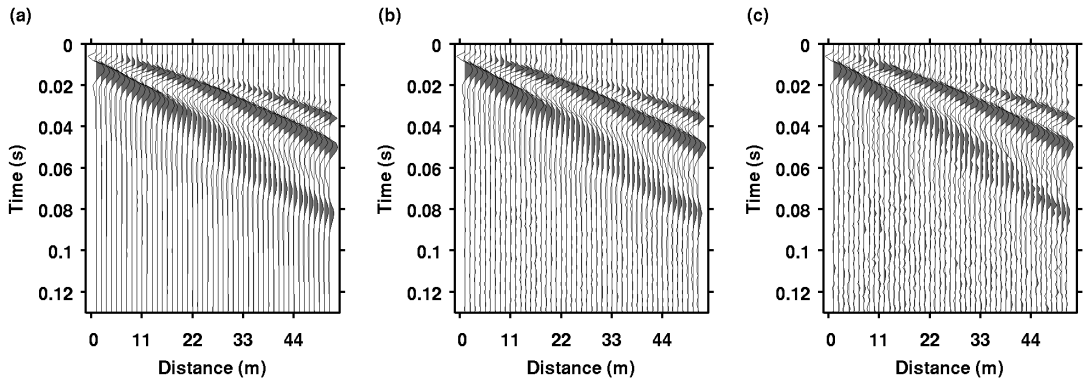

Figure 2.7 Synthetic data sets: (a) Noise-free shot gather generated by wavenumber integration method using reference model parameters listed in Table 2.1. 20% and 45% Gaussian noise are added to the same shot gather, resulting in S/N of (b) 14 dB and (c) 7 dB (the signal-to-noise ratio $S/N = 10\log_{10}\left(\sum_{i=1}^{N_t} A_{Si}^2 \Big/ \sum_{i=1}^{N_t} A_{Ni}^2\right)$, where A_S denotes the amplitude of the signal, A_N denotes the amplitude of the noise, and N_t denotes the total number of points in each trace of the shot gather).

Effects of viscoelastic attenuation

The synthetic examples shown above consider purely elastic models. Nevertheless, near-surface sediments are often strongly attenuating—a factor that could significantly modulate the energy distributions of dispersion spectra, and thus a simultaneous inversion of velocity and attenuation structures may seem attractive. For such an inversion, however, the increased problem dimensionality can dramatically increase runtime of the direct-search method. For this reason, although neglect of attenuation can potentially introduce biases to the resulting velocity structure, elastic inversion is often selected for computational efficiency reasons. In this section, we explore probable ranges of attenuation within which elastic inversion remains viable—in the context of near-surface structures in permafrost.

To investigate the validity of our elastic inversion strategy in the presence of attenuation, we conduct a series of elastic inversions to invert synthetic data generated from viscoelastic models. We then compare the inverted velocity structure against the reference values to examine the extent of biases introduced by the neglect of attenuation. Based upon the same reference model shown in Table 2.1, we first construct viscoelastic models for this test by assigning uniform quality factor Q (assuming $Q_P = Q_S$ for P- and S-waves) to each layer. Following the heuristic rule that high velocities often accompany high Q values, and vice versa, we use a high Q value for the high-velocity top layer and a low Q value for both the low-velocity middle layer and the low-velocity half-space (i.e., $Q_1 > Q_2 = Q_3$). We fix the high Q value at 200, which is comparable to field-measured Q values of ~250 for hydrate-rich sediments (Sain and Singh 2011, Sain et al. 2009)—here used as an analog for ice-rich permafrost. Next, we vary the low Q value between 50 and 10 so as to evaluate the range of Q values within which elastic inversion can recover model parameters with satisfactory accuracy, despite the presence of attenuation.

The test results (Table 2.4) indicate that elastic inversion remains accurate (with biases no greater than 5.7% in the inverted model parameters) if the low Q value of the viscoelastic model does not fall below ~24. This lower limit of Q for applying elastic

inversion is within the range of Q values bounded by the two "end-member" sediments (surficial water-saturated sands and silt-clays) as summarized in Hamilton (1976): Q_P of 24–45 and Q_S of 7–31 for sands; and Q_P of 105–314 and Q_S of 10–31 for silt-clays (mud). These ranges of Q values are likely to be comparable to Q values in ice-poor permafrost (e.g., partially-frozen or unfrozen permafrost). Considering the lower limit of ~24 for Q, elastic inversion remains valid unless very low Q values are present. In this study, we only consider elastic inversion by assuming that very low Q values are absent in permafrost structures relevant to our field site.

Table 2.4 Model parameters obtained from elastic inversion of the synthetic data that are generated from viscoelastic models.

Model parameters **m**	$Q_{low} = 50$	$Q_{low} = 30$	$Q_{low} = 24$	$Q_{low} = 20$	$Q_{low} = 10$
h_1 (m) [2.5]	2.5943	2.5846	2.5665	1.5943	1.5796
V_{P1}/V_{S1} [2.8]	2.8325	2.8126	2.7913	1.4368	1.4430
h_2 (m) [10.0]	9.5525	9.4605	9.4305	42.7143	21.4553
V_{S2} (m/s) [560.0]	557.7641	565.4795	571.8087	658.7902	700.5756
V_{P2}/V_{S2} [4.0]	4.1543	4.1844	4.1830	3.2013	3.2287
V_{S3} (m/s) [670.0]	668.2552	670.5021	672.8193	705.3940	711.2991

Parameter values of the reference model are given in square parentheses.

2.5 Field data inversion

After validating the full-wavefield method through the synthetic tests, we apply it to the inversion of our field data acquired at the BEO site.

2.5.1 Performance evaluation of the full-wavefield method

We first evaluate the performance of the optimization procedure in the field-data experiment. Starting with the search bounds shown in Table 2.5, the total number of iterations range from 570 to 950 for a given shot gather, which corresponds to around 4–11 hours of runtime (wall-clock time). Figure 2.8 shows an example of the iteration history obtained from the shot gather corresponding to section b in Figure 2.1c. Similar to the algorithmic behavior observed in the synthetic experiments, the MCS-NM hybrid method balances global exploration and local exploitation. Although the overall patterns of the iteration history are similar to the synthetic case, the hybrid method, when applied to the field data, generally spends a larger number of iterations on broad MCS exploration in comparison to the iterations required for the NM local-search enhancement. This may be explained by the more rugged objective-function hypersurface as expected in the presence of data error.

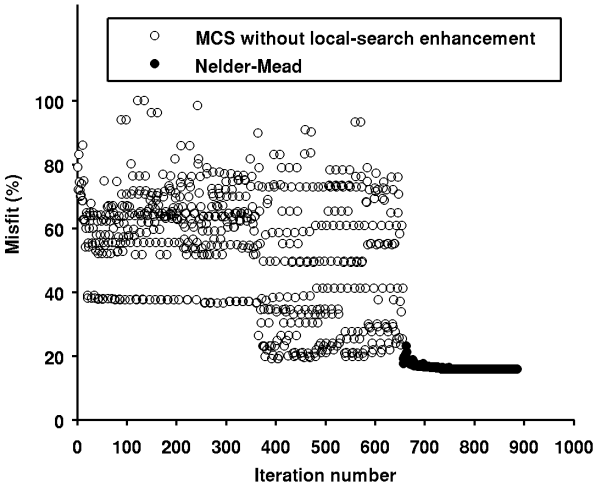

Figure 2.8 Iteration history of the MCS-NM hybrid method when applied on the field data acquired at section b of the survey line (see Figure 2.1c).

Table 2.5 Search bounds of the MCS (Multilevel Coordinate Search) solver used in the field-data experiment.

Model parameters m	**Lower bound $\mathbf{m^{(l)}}$**	**Upper bound $\mathbf{m^{(u)}}$**
h_1 (m)	1.0	5.0
V_{P1}/V_{S1}	1.1	3.0
h_2 (m)	2.0	20.0
V_{S2} (m/s)	300.0	2000.0
V_{P2}/V_{S2}	1.1	3.0
V_{S3} (m/s)	300.0	2000.0

Next, we check the quality of the optimal solutions by examining the resultant data fits. Moreover, even though the inversion is based upon dispersion spectra in the *f-v* domain, we also examine the waveform fit in the *x-t* domain. A representative example of the data fits is given in Figure 2.9 (corresponds to section b of the survey line shown in Figure 2.1c). In the *f-v* domain (Figure 2.9d and 2.9e), the dominant "two-patch" pattern of the dispersion spectra are consistent between the synthetic and observed dispersion spectra. For the low-frequency components (~10–50 Hz), although differences are present between the energy distribution of the synthetic and observed spectra (as shown by the orange and light blue patches in Figure 2.9f)—the spectral highlight of the observed spectrum is more narrow-banded and slightly richer in very low frequency content (~10–13 Hz) than the synthetic spectrum, both the shape and position of the spectral highlights match well between the model prediction and the real data; but for the high-frequency components (~60–130 Hz), the position of the spectral highlight is shifted in the synthetic spectrum, yielding the associated differences shown in Figure 2.9f (the orange and light blue patches). Likewise, in the *x-t* domain (Figure 2.9a, 2.9b, and 2.9c), while the strong low-frequency wavelets are in good agreement between the synthetic and observed shot gathers, the weaker high-frequency wavelets are not well aligned. Such

discrepancies in the high-frequency components, though undesirable, are expected because they are fairly weak in the wavefield and thus are more susceptible to biases in the inversion. Despite the less satisfactory fit to the high-frequency portion of the wavefield, the optimal model is able to predict the presence, shapes, and relative amplitudes of the major wavelets in the *x*-*t* domain, even though no direct waveform fitting is used in the inversion.

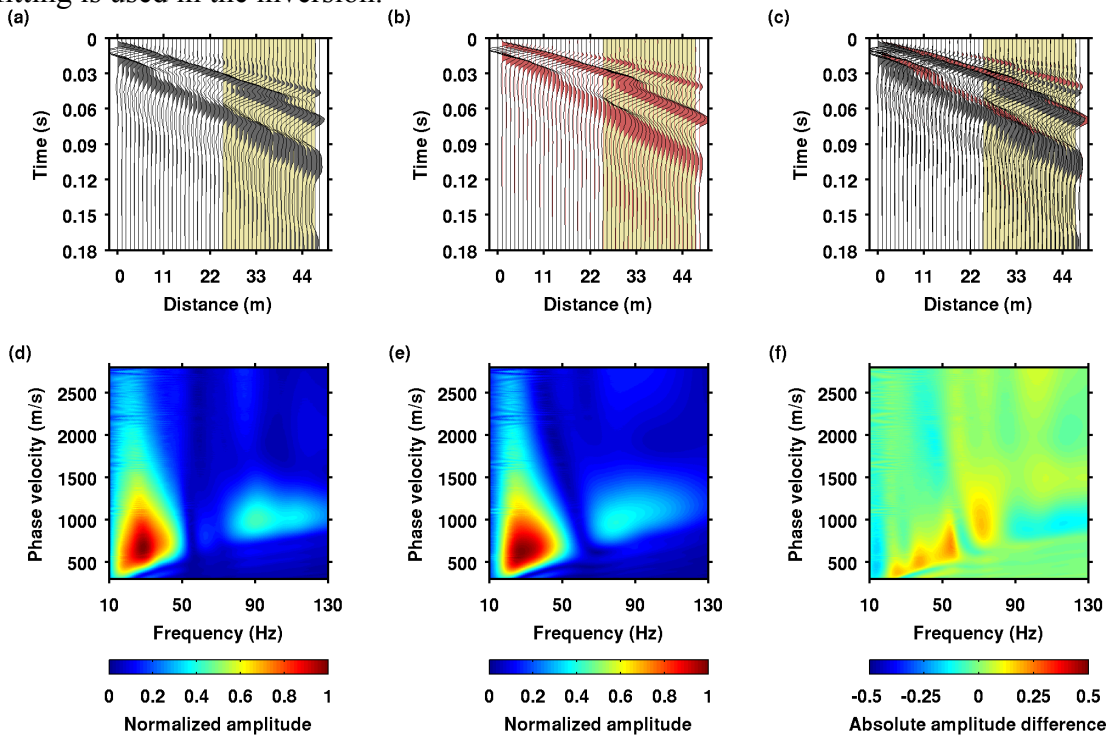

Figure 2.9 Example of data fits for the field data (section b in Figure 2.1c): The top panels show *x*-*t* domain displays (i.e., shot gathers) for (a) observed wavefield, (b) synthetic wavefield, and (c) overlay of the observed and the synthetic wavefields. The light yellow patches show the range of the source-receiver offset (27.5–51.7 m) used for computing the dispersion spectra. The bottom panels show *f*-*v* domain displays (i.e., dispersion spectra) for (d) observed wavefield, (e) synthetic wavefield, and (f) difference between the observed and the synthetic wavefields.

To summarize, the full-wavefield approach converges appropriately when applied to the field data. Even though the method is based upon dispersion spectra other than direct waveform fitting, the model-predicted wavefield compares well with the observed counterpart in both the *x*-*t* and *f*-*v* domains.

2.5.2 Results: permafrost models with embedded low-velocity zones

After confirming the effectiveness of the full-wavefield method when applied to the field data, we conduct the six-parameter inversion to invert the data. Here we examine the resulting models in this section.

In order to gain knowledge about both the vertical and lateral characteristics of the inverted S-wave velocity structures, we compile the model estimates into Table 2.6. The most striking features shared by these model profiles are the pronounced low-velocity zones (~300–680 m/s) that underlie the thin high-velocity top layer (with

velocities of ~1700–2600 m/s and thicknesses of ~3.5–4 m). We cannot resolve the maximum depths of the low S-wave velocity zones because of the limited investigation depths of the wavefield, but we are confident that these zones extend at least down to ~25 m below the surface.

Table 2.6 Model parameters inverted from the field data.

Section index	Layer index	h (m)	V_P (m/s)	V_S (m/s)	V_P/V_S
a	1_a	3.5	3134.9[1]	1692.2	1.85
	2_a	13.1	914.2	396.3	2.31
	3_a	∞	976.7	348.2	2.80[2]
b	1_b	3.5	3026.8[1]	2395.2	1.26[*]
	2_b	1.8	1215.4	687.6	1.77
	3_b	∞	846.9	302.5	2.80[2]
c	1_c	3.8	2978.1[1]	1813.5	1.64
	2_c	18.6	1015.6	480.2	2.11
	3_c	∞	1012.9	361.7	2.80[2]
d	1_d	4.1	3244.6[1]	2617.4	1.24[*]
	2_d	18.1	1045.7	448.8	1.99
	3_d	∞	1032.8	368.9	2.80[2]

Density of all the layers is fixed at 2000.0 kg/m^3 throughout the inversion. V_P of the middle layer and the half-space, which are indirect estimates derived from the inverted V_S and V_P/V_S ($V_P = V_S\left(V_P/V_S\right)$), may carry large uncertainties due to surface waves' low sensitivity to V_P/V_S.

[1] V_P of the top layer are fixed at the measured values obtained from first arrivals.

[2] V_P/V_S of the half-space is fixed at 2.80 throughout the inversion.

[*] This parameter may be poorly constrained.

In order to evaluate the extent to which we can constrain the model estimates obtained from the inversion, we compute approximate uncertainty envelopes in the following way: We perturb each model estimate around its original value and compute the corresponding objective-function values for the perturbed model profiles; next, we choose threshold objective-function values that are 10% larger than the minimum misfit; in the end, we use the parameter values associated with the misfit threshold as the upper- and lower-bounds of the uncertainty envelopes. Here we report minimum and maximum bounds of the parameters among all four sections listed in Table 2.6: (1) −0.5 to +1.2 m for h_1; (2) −0.35 to +0.70 for V_{P1}/V_{S1} (translates to −880 to +830 m/s for V_{S1}); (3) −16.5 to +8.0 m for h_2; (4) −107 to +182 m/s for V_{S2}; (5) −0.45 to +0.35 for V_{P2}/V_{S2}; (6) −70 to 127 m/s for V_{S3}. In all six parameters, h_2 carries the largest uncertainty. This is mainly due to the very small velocity contrast between the middle layer and the half-space (both layers have velocities that are much lower than the top layer), which yields the low sensitivity of the objective function with respect to h_2; and it is consistent with the appearance of the 1D objective-function cross section demonstrated in the synthetic

experiment (Figure 2.4b). V_{S1} values also have large uncertainties, which could be a result of the method's relatively low sensitivity to the high-frequency portion of the wavefield. Velocity values of the low-velocity zones (V_{S2} and V_{S3}), however, have narrow uncertainty envelopes and thus are well constrained.

We also qualitatively evaluate the model estimates by comparing the seismic velocity models with results obtained from a different geophysical method—the ERT profile (Figure 2.10). Although the boundaries between high- and low-velocity layers do not match the boundaries between high- and low-resistivity features in a precise fashion, the first-order layering structures between seismic velocity (V_S) and electrical resistivity are in general agreement. Furthermore, the consistent results between these two different geophysical methods indicate that the low-velocity zones are likely to also have very low electrical resistivity (~10 ohm-m) (Hubbard et al. 2013).

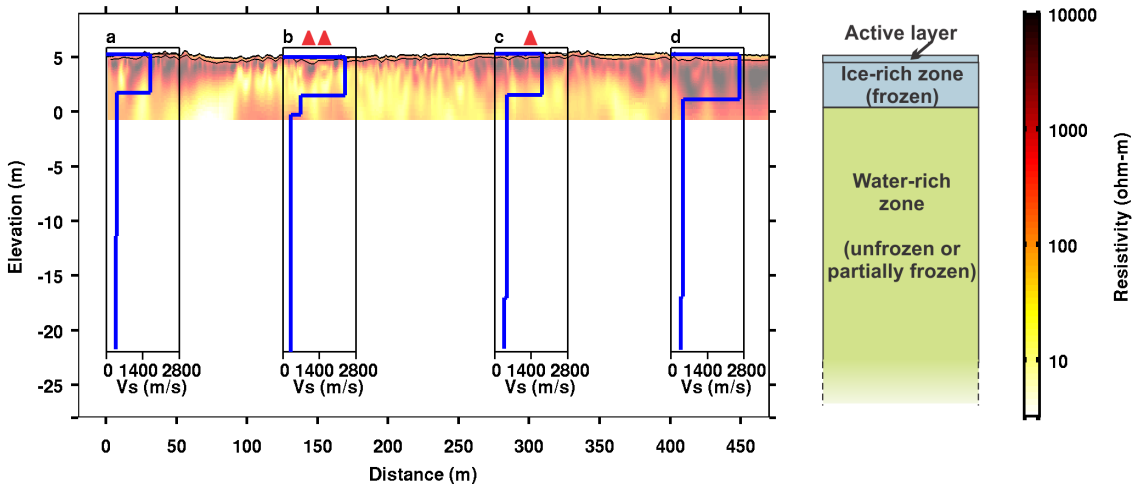

Figure 2.10 Comparison of S-wave velocity profiles and the electrical resistivity tomography (ERT) results (Hubbard et al. 2013). Shear-wave velocity (V_S) profiles a, b, c, and d correspond to locations shown as section a, b, c, and d in Figure 2.1c. The red triangles show the locations of three core samples. The schematic on the right shows the conceptual permafrost model with embedded water-rich zones.

Beyond the first-order layering, more detailed comparisons between the ERT profile and the seismic models are neither possible nor meaningful at this point. This is because of their fundamentally different inversion schemes and their different sensitivities to water-content changes. First, the ERT profile is intrinsically smooth as a result of the 2nd-order Tikhonov regularization used in the tomographic inversion; whereas seismic profiles—based upon a layered-model parameterization (two layer over a half-space)—present the subsurface as distinct layers. Second, for a given amount of changes in water content, electrical properties (strongly depend on fluids that carry ions) generally show more pronounced variations than seismic properties (mainly transmit energy through the solid matrix of the medium); and such sensitivity difference could be amplified in the presence of dissolved salts.

In addition, seasonal differences in the acquisition time further impede an exact comparison between the ERT profiles and the seismic models. The electrical resistivity data were acquired near the end of the thaw season at Barrow (end of September)

(Hubbard et al. 2013), whereas the seismic data were acquired near the end of the freeze season (mid-May). In response to the atmospheric temperature changes, seasonal variations in ground temperatures, though decreasing with increasing depths, are present from the surface all the way down to ~15–20 m below the surface (V. Romanovsky, personal communication, 2013). As a result, the boundary between the shallower and deeper permafrost layers could vary in response to these seasonal changes. Because electrical resistivity is much more sensitive to small changes in water content than seismic velocities—especially in the presence of dissolved salts, a detailed comparison between the ERT profile and the seismic models is not possible.

Despite that an exact comparison is presently unfeasible, the consistency in the first-order layering between the ERT profile and the seismic models provides key information about the permafrost subsurface—particularly, the presence of the embedded low-velocity and low-resistivity zones that may only be partially frozen or unfrozen. Moreover, it suggests the possibility for a joint inversion of concurrent seismic and electrical data in the future.

2.6 Discussion

Given the sub-zero ground temperatures—around −8 °C to −10 °C in nearby boreholes in the depth range of ~3–25 m (V. Romanovsky, personal communication, 2012), the low-velocity zones at depth are unusual features: These well-constrained zones exhibit S-wave velocities that are as low as 300–680 m/s, whereas ordinarily S-wave velocity of ice-rich frozen ground should be close to the velocity in pure ice (~1800 m/s) (Tsuji et al. 2012). The low S-wave velocity values could be reasonable in ice-depleted ground that is either dry or water-saturated. But the low-velocity zones of our study site are not likely to be dry because of the collocated low electrical resistivity values (~10 ohm-m; about 10–1000 times lower than typical values observed in permafrost). As a result, low values both in electrical resistivity and seismic velocity point to an alternative interpretation: These embedded low-velocity zones are likely to be water-rich ground that are saturated with water or an ice/water mixture.

Under sub-zero temperatures of −8 °C to −10 °C, high salt content is a plausible mechanism for preventing water from freezing through its freezing-point depression effect. For example, assuming that the dissolved salts are made entirely of NaCl, a pore-water salinity of 140 g/L (four times of the typical seawater salinity) can lower the freezing point of soils down to −8 °C according to the empirical equation developed by Velli and Grishin (1983) (Appendix A1). Therefore, the low-velocity (and low-resistivity) zones may contain saline pore-waters and thus remain perennially unfrozen or only partially frozen under sub-zero temperatures. The salts could have originated from sea water contained in marine deposits—the predominant source of the unconsolidated sediments at Barrow (Black 1964). In extreme cases, salt content may be sufficiently high that these saline layers or zones remain perennially unfrozen while still constituting part of the permafrost (a class of features often referred to as “cryopegs” in permafrost literature).

Subsequent to the surface-wave acquisition campaign, three core samples were extracted along the same survey line (see symbols on Figure 2.10; core depths are 1.65 m, 2.55 m, and 3.10 m, respectively), which provide evidence in support of the presence of saline pore-waters at depth. These three cores, apart from the differences in the depth

extent of their ice-rich top sections, have broadly similar profiles with partially frozen basal sections starting from the depths of around 1.4–2.6 m. Preliminary core-sample analysis shows that the electrical conductivity of the pore fluid extracted from the partially frozen section is as low as 1.5–2.0 S/m (equivalent to a resistivity range of 0.5–0.7 ohm-m; comparable to typical seawater resistivity of ~0.2 ohm-m) (Dafflon et al. 2014). Despite the fact that these core samples do not reach deep enough to directly sample the embedded low-velocity zones that are uncovered by our surface-wave data, the saline basal sections are suggestive of a pronounced saline-permafrost zone at depth. In addition, prior studies have reported many observations of cryopegs and/or saline permafrost in the Barrow vicinity (Brown 1969, Meyer et al. 2010, e.g., O'Sullivan 1966, Williams 1970, Yoshikawa et al. 2004). Therefore, the presence of saline permafrost appears to be the most plausible cause for the observed low-velocity zones.

The extensive presence of saline permafrost at the BEO site, if confirmed, may impact the estimates of organic carbon degradation as well as biogenic gas fluxes (CO_2 and CH_4) from deeper permafrost strata. Because substantial amount of water remains liquid in saline permafrost at sub-zero temperatures, cold-adapted microorganisms could maintain metabolisms with the aid of liquid water. Studies by Gilichinsky et al. (2005), for example, have found active microorganisms in marine cryopegs from Siberia that may have survived for 43,000 years at −10 °C.

In addition to seismic field survey and deep coring, laboratory testing of seismic velocities in saline permafrost could provide rock-physics insight to facilitate seismic interpretation efforts. Several previous laboratory studies have approached the effect of dissolved salts in consolidated permafrost (Pandit and King 1979), unconsolidated permafrost (King et al. 1982, Matsushima et al. 2011), and ice-brine mixtures (Matsushima et al. 2008, e.g., Spetzler and Anderson 1968a). Although they all come to the consensus that freezing-point depression of salts can keep seismic velocities low even at sub-zero temperatures, the salinities used in these studies is generally low (mostly lower than typical seawater salinity) and the range of the tested salinity is quite narrow.

2.7 Conclusion

In summary, our study demonstrates that the dispersion analysis and the full-wavefield inversion of surface waves are effective for detecting and delineating embedded low-velocity zones in permafrost. Although surface-wave methods are generally applicable even when velocity reversals are present in the ground (i.e., seismic velocities do not always increase with depths), velocity reversals embedded in permafrost can be unusually drastic, considering the large velocity contrasts (~70%–80%) between the frozen and unfrozen materials. Consequently, higher-order modes dominate the wavefield, and leaky modes further complicate the energy distributions in the wavefield. In this case, it is impossible to identify or pick individual surface-wave modal curves, and thus the conventional, dispersion-curve-based inversion methods become unsuitable. In contrast to the conventional methods, the full-wavefield approach used in our study does not rely on individual modal curves. Moreover, our method uses the complete signal content of the wavefield—including higher-order modes, leaky modes, the energy distribution, and all the acquisition and processing effects—to constrain the velocity structures. With the full-wavefield method, we are able to infer embedded low-velocity zones from inversely dispersive surface-wave data acquired from our study site at Barrow,

Alaska. The low-velocity zones may correspond to saline unfrozen or partially frozen zones enclosed in permafrost.

Our full-wavefield approach is currently limited by the high computational cost, the nonlinear nature of the inverse problem, and the simplicity of model parameterization. Computing the full-wavefield is much more time-consuming than computing modal curves. The irregular and possibly drastic velocity variations in permafrost also increase the nonlinearity of the inverse problem, which yields slow convergence of the optimization procedure. Lastly, in order to alleviate "the curse of dimensionality" (with increasing number of model parameters, runtime rapidly increases while the quality of the solutions deteriorates), parsimonious model parameterization must be used. As a result, velocity models obtained through the full-wavefield method are simple, and thus fine-scale features may not be effectively resolved.

Despite these limitations, the full-wavefield method is a promising technique for quantitative delineation of permafrost. Embedded low-velocity zones, which are challenging imaging targets for conventional seismic prospecting, can be effectively inferred from the field data. The resulting velocity models, although simple, provide key information about physical properties of the subsurface. In addition, if more detailed velocity structure is desirable, the full-wavefield method could provide starting models for further refinement via techniques such as classical time- and frequency-domain waveform inversion.

3. Wavefield inversion of surface waves using Particle Swarm Optimization (PSO) for seismic delineation of saline permafrost: a case history from the Barrow peninsula, AK

3.1 Introduction

The primary purpose of this study is to use multichannel surface-wave methods to delineate seismic-velocity structures and spatial extents of saline permafrost across the Barrow Environmental Observatory (BEO), a 7,466-acre research reserve that is located at the northernmost part of the Alaskan Arctic Coastal Plain. This study also has a broader goal on method developments: given that the permafrost structures at the BEO could be representative of a considerable portion of the permafrost across the Arctic coastal tundra, we can use the BEO as a testing ground for developing surface-wave workflows that are applicable in other areas along the Arctic coast.

This study centers upon active-source surface-wave datasets (the seismic source is a 30 lbs sledge hammer) that were acquired in our field survey in the winter of 2014. This survey is a follow-up to the pilot survey conducted in the winter of 2012. The pilot survey provided surface-wave datasets that revealed a striking presence of saline permafrost at BEO, which manifest themselves in the seismic velocity profiles as embedded low-velocity layers that lie 3–5 meters below the surface (detailed in Dou and Ajo-Franklin (2014) and Chapter 2). This finding is significant, because it suggests that saline permafrost is likely to be pervasive in the BEO, and considering that coastal areas are generally optimal for forming saline permafrost due to the proximity of seawater, saline permafrost could be widespread across the Arctic coastal tundra. However, the limited spatial coverage provided by the pilot survey (a 400-meter-long survey line) was insufficient for determining if saline permafrost is indeed pervasive. To better understand the lateral extent of saline permafrost in the BEO, we conducted the 2014 survey along a 4300-meter-long transect that extends from the coast to the inland boundary of the BEO.

In addition to the lateral extent, we also wanted to better constrain the vertical extent and the depth-dependent variations of the velocities within the saline permafrost units. The former provides crucial scale parameters for estimating the overall impact of saline permafrost in a warming climate. The latter is closely related to the depth-dependent variations of pore-water salinity, which in turn could shed light on the evolution history of the saline permafrost.

To apply surface-wave methods meeting the objectives described above requires using datasets that satisfy a number of criteria: 1) The signal content of the datasets must be adequately rich so as to produce velocity profiles that contain reliable details; 2) The maximum investigation depths (i.e., the depth range that can be adequately sampled by surface waves) allowed by the datasets must be deeper than the bottom of the saline

permafrost layers. For multichannel surface-wave surveys that use off-end[3] linear arrays, the signal content and investigation depths of the shot gathers are dictated by the receiver spacing and the array lengths (Socco et al. 2010, Socco and Strobbia 2004). Small receiver spacing is necessary for sampling short-wavelength signals that are key in resolving small-scale velocity structures. Longer arrays facilitate the recording of long-wavelength signals that can help deepen the investigation depths of the datasets. In this study, we chose a receiver spacing of 1 m, which is close to the what was used in the 2012 pilot survey, and a maximum array length of 84 m, which is 60% longer than the array length used in the 2012 pilot study.

Besides the extended data coverage, this study also benefits from the use of the cylindrical slant stack in surface-wave dispersion analyses. Commonly used methods such as (Cartesian) slant stack and frequency-wavenumber (*f-k*) transform are based upon plane-wave decomposition of the wavefield. To keep the plane-wave approximation valid, near-offset records need to be excluded because the curvature of the wavefront cannot be ignored (Park et al. 1999). Consequently, only a subset of the signals associated with the far offsets could be used in the dispersion analyses. By contrast, cylindrical slant stack is accurate for all offsets because it naturally takes into account the curvature of the wavefront (Forbriger 2003a). As a result, all the signals along a line are available for use in the dispersion analyses, which can help better constrain the inversion results.

The presence of embedded saline permafrost yields wavefields with complicated dispersion characteristics that render conventional surface-wave inversion methods ineffective. In conventional inversion methods, the objective function is the misfit between the observed and model-predicted modal curves. Hence, modal curves must be extracted from the observed dispersion spectra prior to the inversion. In the presence of embedded saline permafrost, however, severe velocity reversals result in complicated dispersion spectra containing a large number of closely spaced overtones (e.g., Lu et al. 2007, O'Neill et al. 2003, Ryden and Park 2006). Because it is difficult to identify and/or retrieve modal curves from these multimodal spectra, conventional methods become inapplicable. Alternatively, instead of using the modal-curve misfits, we adopt a full-wavefield approach that uses the misfits between the observed and the model-predicted dispersion spectra as the objective function. This unconventional approach has been tested and proven effective in our previous work reported in Dou and Ajo-Franklin (2014) and presented in Chapter 2 of this dissertation. The main limiting factor is the high computational costs, because a complete wavefield needs to be computed at each iteration of the forward modeling.

In this study, although the forward modeling step remains computationally costly, we improve the efficiency of the inversion by using particle swarm optimization (PSO). PSO is a population-based stochastic global optimization method that was first introduced by Eberhart and Kennedy (1995). It is fast-converging, easy to comprehend, straightforward to implement, and readily parallelizable (Brownlee 2012, Poli et al. 2007, Shaw and Srivastava 2007). As a metaheuristic algorithm, PSO requires very few tuning parameters, and typical values of the tuning parameters often work well across a broad range of problems. Owing to these merits of PSO, we are able to increase the number of

[3] "Off-end" means that the seismic source is placed inline and beyond the end of the linear geophone array.

unknowns in our nonlinear inverse problem, which in turn helps resolve more detailed velocity structure.

3.2 Field site and acquisition layout

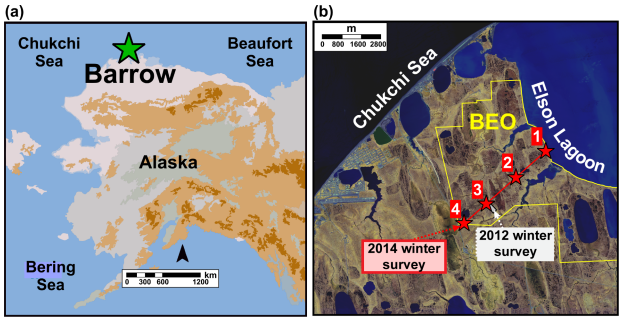

Figure 3.1 Maps of the study area near Barrow, Alaska: (a) the Barrow area within Alaska (green star). (b) The 4300-meter-long survey transect (red line) running across the Barrow Environmental Observatory. Red stars (1–4) denote the locations of the multichannel surface-wave survey.

The Barrow Peninsula, located at the northern extremity of the Arctic Coastal Plain in Alaska, is underlain by continuous permafrost to estimated depths of more than 300 m. The sediments are primarily of marine origin. In early May of 2014, we conducted an active multichannel surface-wave survey (sledge hammer source) along a 4300-m (2.7-mi) northeast-southwest trending transect that extended from the coastal to the interior areas of the peninsula. We acquired surface-wave gathers—each with a maximum offset of 84 m and receiver spacing of 1 m—from four nearly equidistantly distributed subsections of the transect (Figure 3.1).

3.3 Method

3.2.1 Dispersion analysis using cylindrical slant stack (modified Hankel transform)

We use a two-step wavefield transformation procedure as described in Forbriger (2003a) to transform the multichannel wavefield from the offset-time (*x*-*t*) domain to the slowness-frequency (*p*-*f*) domain. In the following we explain the steps that are involved.

We start from a multichannel surface-wave shot gather that comprises N seismic traces $u(t,x_k)$ recorded at offset x_k, where $k=1,2,\cdots,N$ is the trace number. We first replace the Cartesian form of offset x_k into its polar-coordinate equivalence r_k. Next, to suppress spectral leakage and to improve spectral resolution, we apply windowing and zero padding to each of the traces. We denote the resulting wavefield as $u_{windowed}(t_{padded},r_k)$.

In the first step of the dispersion analysis, we transform the wavefield into its frequency spectrum with Fourier transform:

$$\tilde{u}(f,r_k)=\frac{1}{\sqrt{2\pi}}\int_{-\infty}^{+\infty}u_{windowed}(t_{padded},r_k)e^{-i2\pi ft}\,dt \qquad (3.1)$$

In the second step of the dispersion analysis, we apply an offset-dependent phase shift $2\pi fpr_k$ to the frequency spectrum $\tilde{u}(f,r_k)$ using a modified Hankel transform:

$$\begin{aligned}\tilde{U}(f,p) &= \int_0^{+\infty} \tilde{u}(f,r) J_0(2\pi fpr) r\, dr \\ &\approx \frac{1}{2}\sum_{k=1}^{N} \tilde{u}(f,r_k) H_0^{(1)}(2\pi fpr_k) r_k \Delta r\end{aligned} \tag{3.2}$$

where $\tilde{U}(f,p)$ is the complex slowness-frequency (*p-f*) spectrum; J_0 is Bessel function of order 0; $H_0^{(1)}$ is Hankel function of the first kind with order 0. Note that the exact relationship between Bessel function and Hankel function is $J_0 = \frac{1}{2}\left(H_0^{(1)} + H_0^{(2)}\right)$. In the modified Hankel transform, the second term $H_0^{(2)}$ is omitted because it vanishes for continuous cases (i.e., when $\Delta r \to 0$) and mainly introduces aliasing artifacts for discrete cases (i.e., realistic receiver spacing Δr) (Forbriger 2003a).

When looping through a range of possible slowness values *p*, signals that travel with a certain phase velocity $v = 1/p$ at frequencies *f* will stack constructively in the summation described in Equation 3.2 and thus manifest themselves as spectral highlights in the amplitude spectrum $\left|\tilde{U}(f,p)\right|$. We then conduct a simple matrix transpose (from *p-f* to *f-p*) and re-parameterize slowness *p* into phase velocity *v* (*v=1/p*). This leads us to the familiar form of the dispersion spectrum presented in frequency-velocity (*f-v*) domain.

Note that the cylindrical slant stack shown in Equation 3.2 is very similar as the commonly used Cartesian slant stack. The only difference is that the kernel of the integral transform is changed from the Cartesian form $e^{i2\pi fpx_k}$ into the cylindrical form $H_0^{(1)}(2\pi fpr_k)r_k$. Because the curvature of the near-offset wavefront is automatically taken into account in the cylindrical slant stack, the number of usable traces in a shot gather is markedly increased. Hence, the accuracy and useful signal content of dispersion spectra are improved.

3.2.2 Spectra-based objective function

As explained earlier in the introduction, we cannot use the conventional form of the objective function in our inversion. Instead, we use the same form of spectra-based objective function as described in Dou and Ajo-Franklin (2014):

$$M(\mathbf{m}) = \sqrt{\frac{\sum_{i=1}^{N_f}\sum_{j=1}^{N_v}(S_{ij} - O_{ij})^2}{N_f N_v}} \tag{3.3}$$

where **m** is the model vector constituted of parameters such as layer thicknesses and S-wave velocities. M is the root-mean-square-deviation (RMSD) that measures the misfit between the synthetic dispersion spectrum S and the observed counterpart O. N_f is the number of sampling points along the frequency axis and N_v is the number of sampling points along the velocity axis. Note that the computation of the synthetic dispersion spectrum *S* requires full-wavefield modeling that is computationally expensive. Hence, computational costs are the major limiting factor for surface-wave inversion of irregularly dispersive media that are similar to our BEO site, namely structures that exhibit strong velocity reversal with depth.

3.2.3 Forward modeling

To forward model a synthetic shot gather, we need to convolve the source wavelet with the Green's function of the model (i.e., the impulse response of the model). As we did in our prior study reported in Dou and Ajo-Franklin (2014) and in Chapter 2, we use the zero-offset trace of the observed shot gather as the empirical source wavelet, and we compute the Green's function of the layered model in response to a vertical point force (mimicking a seismic hammer impact) using the wavenumber integration method of Herrmann (2004).

3.2.4 Model parameterization

Our model parameterization follows Occam's razor philosophy: That is, we set up the minimum number of unknowns that allows the model to have adequate complexity. In this study, we hope to resolve the depth extent and depth-dependent variations of velocities within the saline permafrost layer. Hence, the unknowns of the inverse problem should at least include the depths of the top and bottom of the saline layer, and the depth-dependent velocity variations within the layer. Moreover, as surface-wave inversion is mostly sensitive to S-wave velocities, we reduce the number of unknowns by using fixed V_P/V_S and density ρ. After taking all these factors into consideration, we use a three-layer configuration (Figure 3.2) in which the top layer and the half-space basement have uniform velocities, whereas the mid-layer has depth-dependent velocity variations that are depicted by a cubic Hermite spline with four nodes. Note that spline-based mid-layer is approximated by a series of 1-meter-thick sublayers (i.e., similar as a piecewise discretization of curves with small segments of straight lines) to which the wavenumber integration method remains applicable. In the end, our inverse problem has nine unknowns to be inverted for (Table 3.1).

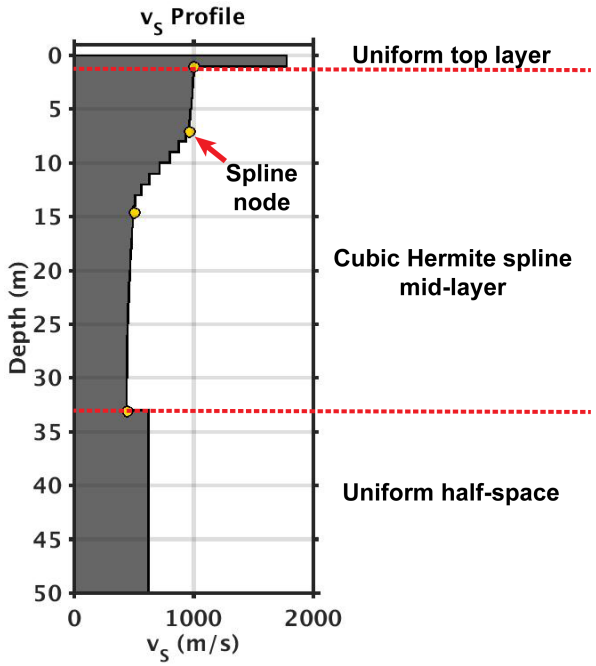

Figure 3.2 An example of the model parameterization. The yellow dots in the mid-layer denote the nodes of the cubic Hermite spline. V_S=S-wave velocity.

Table 3.1 Model parameters.

Layer index	Characteristics	Variables	Fixed parameters	
			Parameter	Value
1	Uniform layer	(1) h_1	V_{P1}^a Line1	3186.0 m/s
			Line2	3079.1 m/s
			Line3	3409.8 m/s
			Line4	3307.3 m/s
			V_{P1}/V_{S1}	1.732
2	Cubic Hermite spline with four nodes	Node 1: (2) V_{S2}^{node1} Node 2: (3) V_{S2}^{node2} (4) h_2^{node2} Node 3: (5) V_{S2}^{node3} (6) h_2^{node3} Node 4: (7) V_{S2}^{node4} (8) h_2^{node4}	V_{P2}/V_{S2}	4.0
3	Uniform half-space	(9) V_{S3}	V_{P3}/V_{S3}	1.732 or 4.0[b]

h is layer thickness (in m). V_S is S-wave velocity (in m/s). V_P is P-wave velocity (in m/s). V_P/V_S is V_P to V_S ratio. The density of all of the layers is fixed at 2000.0kg/m^3.

[a] V_{P1} values are obtained from traveltime of the direct P arrivals.

[b] When $V_{S3} \geq 1500.0$ m/s, $V_{P3}/V_{S3} = 1.732$; when $V_{S3} < 1500.0$ m/s, $V_{P3}/V_{S3} = 4.0$.

3.2.5 Particle swarm optimization (PSO)

To solve the inverse problem, we look for model parameters that can minimize the objective function. Our full-wavefield approach yields a non-linear inverse problem whose objective function usually contains many local minima (as shown in Dou and Ajo-Franklin (2014)). It is therefore necessary to use global optimization methods to search for the solutions. Moreover, note that partial derivatives of our spectra-based objective function cannot be directly estimated, which renders gradient-based optimization methods inapplicable. Instead, we use derivative-free methods that do not require partial derivatives of the objective function in the optimization process.

In this study, we use a MATLAB implementation of particle swarm optimization (PSO) algorithm developed by Chen (2014). PSO is a population-based stochastic global optimization method that was first introduced by Eberhart and Kennedy (1995). It was

inspired by the group foraging behaviors of animals such as bee swarms, fish schools, and bird flocks.

We can compare the optimization process of PSO to a flock of N birds searching for food. The bird flock forms a *swarm*, in which each individual bird is a *particle*. The location of the food is analogous to the solution of the inverse problem. At the kth iteration of the search process, each particle moves around the search space with its position $p_i^{(k)}(i=1,2,\cdots,N)$ influenced by its own best past position $p_i^{(BEST)}$ and the best past position of the whole swarm $p_g^{(BEST)}$. The particle velocity used for updating particle position from the previous position $p_i^{(k-1)}$ to the new position $p_i^{(k)}$ is computed using:

$$v_i^{(k)} = w^{(k)} v_i^{(k-1)} + c_p r_1 (p_i^{(BEST)} - p_i^{(k-1)}) + c_g r_2 (p_g^{(BEST)} - p_i^{(k-1)}) \tag{3.4}$$

where $w^{(k)}$ is the inertia coefficient that is introduced to control the exploration ability of the swarm: larger values of $w^{(k)}$ allow larger value of velocity $v_i^{(k)}$, hence promoting wider exploration of the search space, and vice versa; c_p is the cognitive learning factor that controls the biases toward the personal best position $p_i^{(BEST)}$ of the particle, and c_g is the social learning factor that controls the biases toward the global best position $p_g^{(BEST)}$ in the swarm; r_1 and r_2 both are random numbers between 0 and 1.

A particle's position is updated using:

$$p_i^{(k)} = p_i^{(k-1)} + v_i^{(k)} \tag{3.5}$$

At any intermediate search step, each particle has a memory of its own personal best position and the global best position achieved by all the particles in the swarm. By making use of these personal and group memories, PSO conducts a combination of exploration and exploitation of the search space. Over time, the particles cluster toward the optima.

The PSO algorithm can be summarized into the following steps:

1) Initialize the N particles with random positions $p_i^{(0)}$ and velocities $v_i^{(1)}$ that are confined within the predefined boundary.
2) Evaluate the objective function values $M(p_i^{(k-1)})$ at particle position $p_i^{(k-1)}$, where $k=1,2,\cdots,N$.
3) Update the particle's personal best position $p_i^{(BEST)}$ and the swarm's global best position $p_g^{(BEST)}$.
4) Compute the velocity vectors $v_i^{(k)}$ using Equation 3.5, and then update the position of the particle to $p_i^{(k)}$ by using its previous position $p_i^{(k-1)}$ and the velocity $v_i^{(k)}$ (Equation 3.6).
5) Repeat steps 2–4 until the stopping criteria are met (e.g., when the predefined maximum number of iterations is reached, or when the improvement between the iteration k and k+1 becomes negligible).

We choose PSO parameters following a few heuristic rules recommended in Brownlee (2012) and the stability conditions described in Perez and Behdinan (2007):

- The number of particles should be low, around 20–40.
- The cognitive and social learning factors should satisfy:

$$0 < c_p + c_g < 4 \tag{3.6}$$

- The inertia coefficient is selected based upon:

$$w_i^{(k)} = w_{\max} - w_{\min} \frac{k-1}{k_{\max} - 1} \tag{3.7}$$

where $k_{\max}$ is the predefined maximum number of iterations; $w_{\min}$ is the predefined minimum inertia coefficient, and $w_{\max}$ is the maximum inertia coefficient defined by $w_{\max} = \max(0.9, w_{\min})$; The inertia coefficients $w_i^{(k)}$, $w_{\min}$ and $w_{\max}$ all need to satisfy:

$$\frac{c_p + c_g}{2} - 1 < w < 1 \tag{3.8}$$

Note that PSO has a few pitfalls that need to be countered, namely:

- PSO often is strongly influenced by the best particle, which could cause the particles to prematurely cluster toward the best particle and quickly converge at a local minimum (Kachitvichyanukul 2012). To increase the chance of locating the global minima, we use a counter strategy that is inspired by Tronicke et al. (2012): Instead of relying on one single run of PSO, we use the collective results obtained from multiple PSO runs, each of which has a different set of randomly selected starting positions and velocities of the particles, and different seeds of the random number generator are used in the intermediate search steps. In the end, we examine an ensemble of optima returned by all of these PSO runs and select the best solutions.
- Particles might leave the boundary of the search space and yield unphysical solutions. To counter this pitfall, we penalize the out-of-bounds particles by artificially increasing the values of the objective function. In this way, the out-of-bounds particles are reflected back into the search space.

We summarized the PSO parameters used in our full-wavefield inversion as follows:

- Number of particles in a swarm: $N = 23$
- Stopping criteria of each PSO run:
  - Maximum number of iterations: $k_{\max} = 1 \times 10^4$
  - Threshold value of minimum objective-function improvement: $\delta = 1.0 \times 10^{-6}$
- Number of PSO runs used in each inversion: $K = 15$
- Cognitive learning factor: $c_p = 1.0$
- Social learning factor: $c_g = 2.0$

- Inertia coefficients: $w_{\min} = 0.4$

3.4 Application to Field Data

3.4.1 Characteristics of the field data

Figure 3.3 shows field data acquired along the BEO transect. The dispersion spectra, though differ in detail, all have spectral highlights that tilt upward, illustrating that high-frequency constituents of the wavefields have higher phase velocities than the low-frequency constituents. Such dispersion characteristics are directly observable in the offset-time (*x*-*t*) domain displays of the shot gathers. Therefore, consistent with our pilot study reported in Dou and Ajo-Franklin (2014), the inversely dispersive wavefields indicate the presence of embedded saline permafrost layers that are partially frozen or unfrozen.

Besides the inversely dispersive trends, the long-period, late-arriving wavelets in the shot gathers are worth noting (marked by the shaded areas in Figure 3.3). Different from the earlier arrivals that are continuously present from near- to far-offset traces, the late-arriving wavelets only start to emerge in intermediate- to far-offset traces. We speculate that these late arrivals could be related to the velocity contrasts at the bottom of the saline permafrost layer. However, identifying or interpreting these arrivals is not straightforward.

To better understand the implications of these late arrivals, we conduct a synthetic test as shown in Figure 3.4 and Figure 3.5. We use two models: Model 1 has no velocity contrast between the mid-layer and the half-space (Figure 3.4b); Model 2 has a 180 m/s velocity increase at the depth of 33 m (Figure 3.5b). The resulting shot gathers (Figure 3.4a and 3.4b) are largely similar, but the shot gather generated from model 2 contains long-period, late-arriving wavelets that are similar as the late arrivals in the field data. The differences in the dispersion spectra are also telling: whereas the spectrum associated with model 1 has a largely continuous spectral highlight, the spectral highlight associated with model 2 shows modulations and appears to be patchy. The patchy appearance of the dispersion spectrum is consistent with the field data (line 2, 3, and 4 in Figure 3.3). Therefore, we conclude that the late arrivals indeed are caused by the velocity increase at the bottom of the saline permafrost.

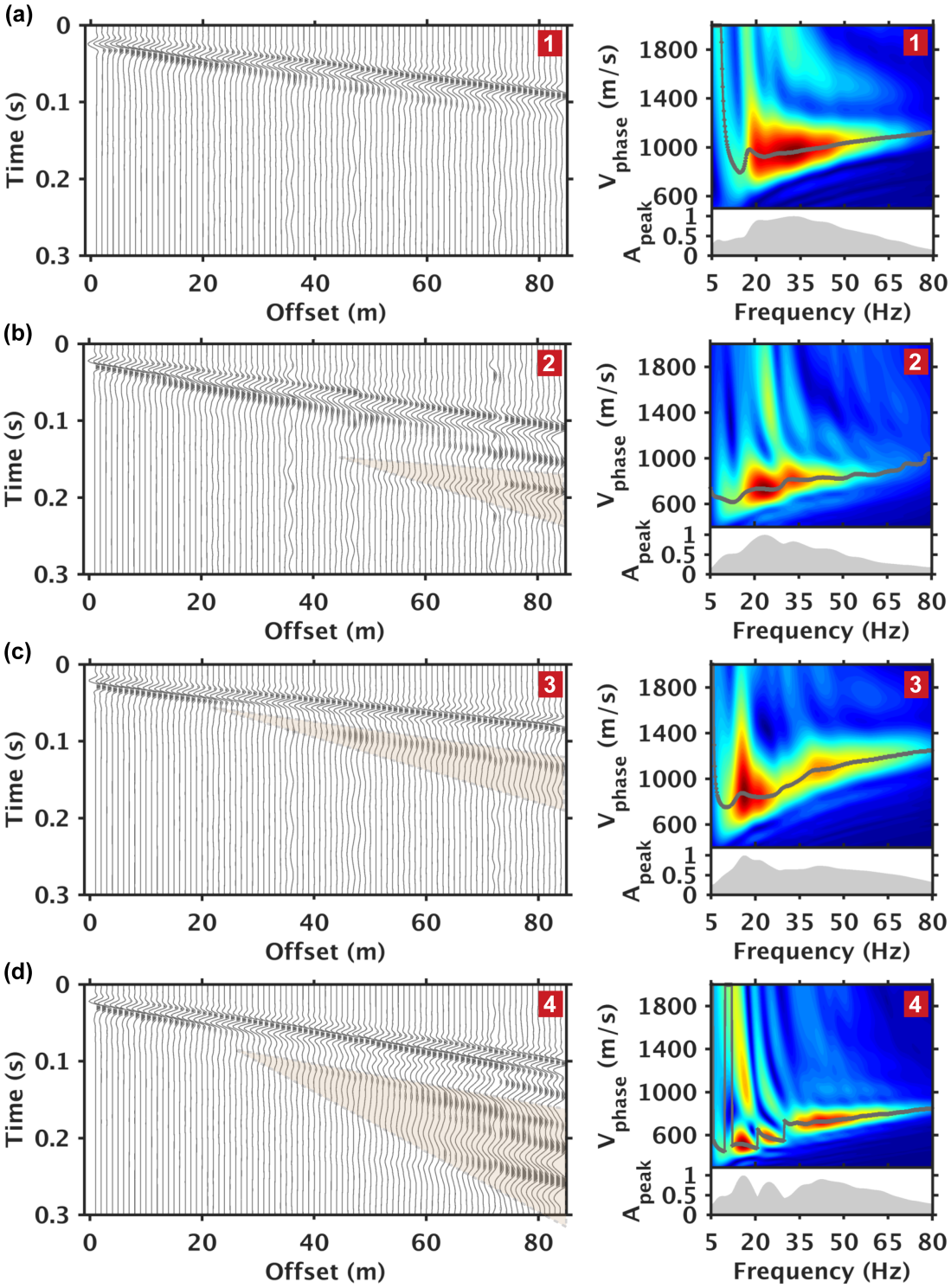

Figure 3.3 Displays of the observed wavefield. Left: shot gathers in offset-time (*x*-*t*) domain. Right: dispersion spectra in frequency-velocity (*f*-*v*) domain. Panel (a), (b), (c), and (d) correspond to line 1, 2, 3, and 4 in Figure 3.1. The shaded areas shown in the shot gathers mark the presence of long-period, late-arriving wavelets that may be related to the presence of positive velocity contrasts at depth. The gray lines shown in the dispersion spectra denote the spectral peaks at each frequency, and the relative amplitudes of these

spectral peaks are displayed in the subpanel underneath the dispersion spectra.

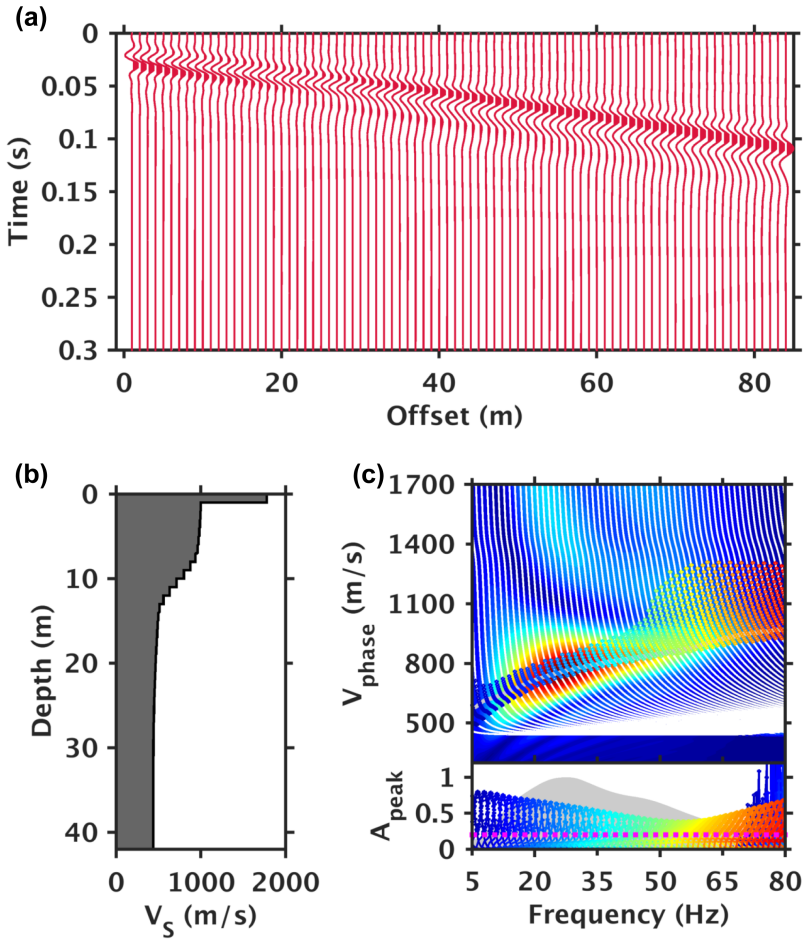

Figure 3.4 Synthetic test results using model 1 that has no velocity contrast between the spline-based mid-layer and the uniform half-space at the bottom. (a) Synthetic shot gather displayed in the offset-time (*x*-*t*) domain, (b) V_S profile of model 1, and (c) dispersion spectrum in the frequency-velocity (*f*-*v*) domain. The shaded area (c) shows the amplitude of the spectral peak at each frequency. The colored curves in (c) show the model-predicted modal dispersion curves and the surface displacement distribution.

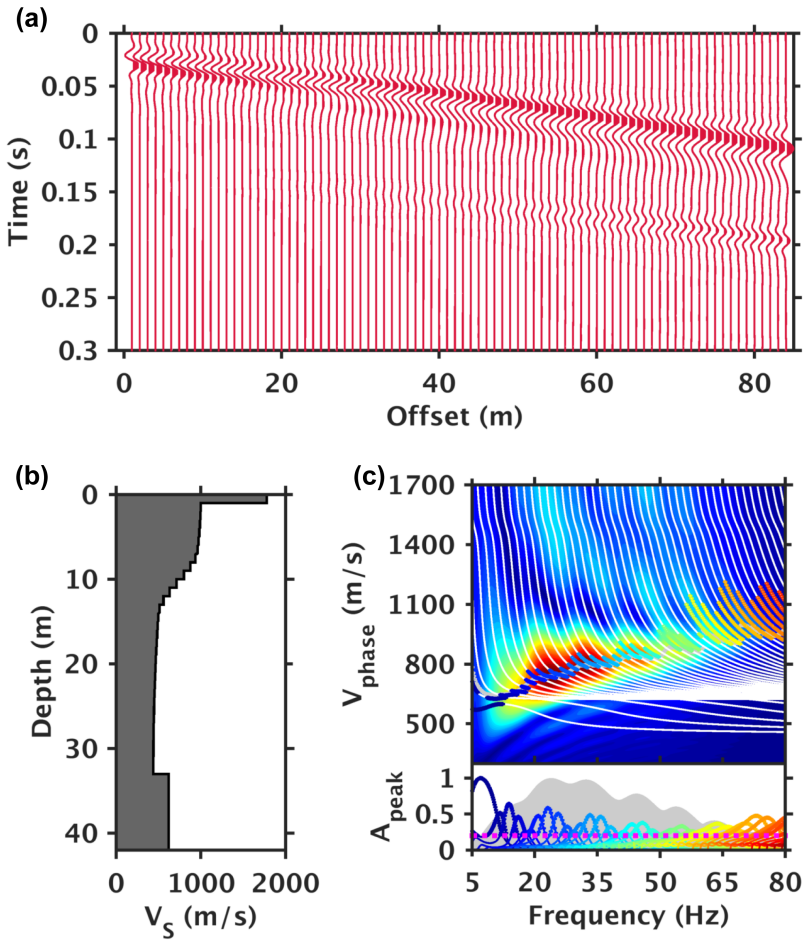

Figure 3.5 Synthetic test results using model 2 that has a velocity increase of 180 m/s between the spline-based mid-layer and the uniform half-space. (a) Synthetic shot gather displayed in the offset-time (*x*-*t*) domain, (b) V_S profile of model 2, and (c) dispersion spectrum in the frequency-velocity (*f*-*v*) domain. The shaded area (c) shows the amplitude of the spectral peak at each frequency. The colored curves in (c) show the model-predicted modal dispersion curves and the surface displacement distribution.

3.4.2 Boundaries of the PSO search space

We set up the boundaries of the PSO search space based upon the following criteria:

- The receiver spacing: The minimum layer thickness contained in the model is dictated by the minimum resolvable wavelength of the wavefield, which is in turn limited by the receiver spacing ($\lambda_{min} \approx \Delta x = 1$ m) (Socco and Strobbia 2004). Hence, our model uses stacks of 1-meter-thick sublayers to discretize the spline-based mid-layer, and the lower bound of the top layer thickness is also set to be 1 m.
- The array length: The investigation depth (i.e., the maximum allowable penetration depth of the wavefield) of the field data approximately equals to the maximum resolvable wavelength, which is limited by the array length (depth $_{max} \approx \lambda_{max} \approx x_{max} =$

84 m) (Richart et al. 1970). The bottom of the embedded saline layer, if detectable, should fall above the allowable investigation depth. Hence, the upper bounds of the thickness parameters of the spline nodes must collectively place the bottom of the mid-layer at a depth that is above the investigation depth. In this study, we use an upper bound value of 20.0 m for all the thickness parameters of the mid-layer, which place the maximum depth of the mid-layer at 66 m.

- The range of resolvable phase velocities and V_{S1} values: As shown in Figure 3.3, the resolvable phase velocities of the wavefield fall in the range of 300–2000 m/s, which approximates the lower and upper bounds of the V_S values. An additional constraint for the V_S upper bound come from the V_S values of the high-velocity, frozen layer (denoted as V_{S1}) that are derived from the measured V_{P1} values (shown in Table 3.1) and the assumed $V_{P1}/V_{S1}(=1.732)$ by using $V_{S1} = V_{P1} \big/ (V_{P1} \big/ V_{S1})$. The resulting V_{S1} values are 1839.5 m/s, 1777.8 m/s, 1968.7 m/s, 1909.5 m/s for line1, 2, 3, and 4, respectively. By integrating this information, we set the V_S search bound to be 200–1000 m/s for the mid-layer and 200–2000 m/s for the half-space at the bottom.

Table 3.2 Lower and upper bounds of the PSO search space.

Layer Index	**1**	**2**							**3**
Model parameter	h_1 (m)	V_{S2}^{node1} (m/s)	h_2^{node2} (m)	V_{S2}^{node2} (m/s)	h_2^{node3} (m)	V_{S2}^{node3} (m/s)	h_2^{node4} (m)	V_{S2}^{node4} (m/s)	V_{S3} (m/s)
Lower bound	1.0	200.0	2.0	200.0	2.0	200.0	2.0	200.0	200.0
Upper bound	6.0	1000.0	20.0	1000.0	20.0	1000.0	20.0	1000.0	2000.0

Table 3.3 Lower and upper bounds for the PSO initialization.

Layer Index	**1**	**2**							**3**
Model parameter	h_1 (m)	V_{S2}^{node1} (m/s)	h_2^{node2} (m)	V_{S2}^{node2} (m/s)	h_2^{node3} (m)	V_{S2}^{node3} (m/s)	h_2^{node4} (m)	V_{S2}^{node4} (m/s)	V_{S3} (m/s)
Lower bound	2.0	300.0	5.0	300.0	5.0	300.0	5.0	300.0	500.0
Upper bound	4.0	700.0	15.0	700.0	15.0	700.0	15.0	700.0	1000.0

We summarize the lower and upper bounds of the PSO search space in Table 3.2, and we use a subset of this search space to restrict the lower and upper bounds of the PSO particle initialization (Table 3.3).

3.4.3 Computational considerations

To maximize the efficiency of the optimization with the computational resources that we have, we enabled the parallel option of the PSO codes and distribute the 23-

particle search on 23 processors (1.2 GHz GenuineIntel processor). To prevent being biased by premature clustering of the particles, we launched a series of 15 PSO runs, each using a different set of randomly selected starting particle positions and velocities, as well as different seeds of the random number generators for intermediate steps. In the end, we examine an ensemble of optima returned by all of these PSO runs and select the best solutions.

Here we provide an overview of the computational costs. For a given PSO run, each of the 23 particles in the swarm went through 138–392 search steps over the course of 2.8–8.4 hours (wall-clock time; 1.0–1.4 minutes per search step). With a total number of 15 PSO runs, each set of the full-wavefield inversion took 61.6–84.7 hours to go over 2911 to 3882 search steps, with the total number of sampled model profiles ranging from 66953 to 87722 (i.e., 2911×23–3882×23). For a 9-variable inversion, such computational costs are hefty, despite that using the parallel implementation of the PSO algorithm has improved the overall efficiency. The most costly part of the inversion is the forward modeling of the full wavefield. However, presently no faster alternatives are available to markedly speed up the forward modeling.

3.4.4 Inversion results

We compile the inversion results in Table 3.4. All four sets of optimal model profiles have the same first-order feature: A low-velocity mid-layer is sandwiched between a high-velocity thin layer on the top and a moderate-velocity half-space at the bottom. To examine whether the characteristics of the V_S profiles exhibit any correlations with how far away the survey lines are away from the coastline, we display these profiles in Figure 3.6 with a layout that is arranged according to the coastal proximity. We can conclude based upon Figure 3.6 that such correlations are not found in our inversion results.

In addition, we also want to gain insight into the amount of uncertainties in the inversion results. Nevertheless, unlike the Monte Carlo search method that is unguided and thus is adequately stochastic for statistical inferences, PSO is self-guided and heavily affected by the best particle in the swarm. As a result, despite the stochastic nature of PSO, quantitative appraisals of the results are not possible unless a large amount of PSO runs can be conducted to provide a sizable ensemble of the optima for statistical inferences. An example of such appraisal strategy is shown in Tronicke et al. (2012), in which 100 PSO runs are conducted to estimate the inversion uncertainties. Given the high computational costs of our full-wavefield inversion, this appraisal strategy is overly expensive. Instead, we focus mainly on quantitative appraisals of the inversion results.

We evaluate the reliability of the inversion results based upon three criteria:

1) How compact or spread-out the ensemble of the good models is. In Figure 3.6, we display an ensemble of models whose associated objective function values are within the top 10% among all the trial models sampled by PSO. The more spread-out the model ensemble is, the higher the uncertainties are, and vice versa. Figure 3.6 shows that the top 20 m of all the model ensembles are compact. The deeper portions of the model ensembles are more spread-out, indicating that the resolving power of the inversion is worsening with depth. the resolving power of the inversion is worsening with depth.
2) The manner in which the optimal model profiles cluster. The clustering of the model

profiles within the ensemble reflects the landscape of the objective-function error surfaces. A largely continuous cluster (line 2 and 3 in Figure 3.6) indicates that the error surfaces may have one predominant "basin" around the optima. The presence of a few separated clusters (line 1 and 4 in Figure 3.6) indicates that the error surfaces are likely to be very rugged, which makes the inversion more susceptible to non-uniqueness issues.

3) How well the PSO optima can predict the wavefield. Figure 3.7, 3.8, 3.9, and 3.10 show the data fits provided by the most optimal solutions (i.e., the black profiles shown in Figure 3.5). Note that although the objective function of the inverse problem is constructed using the dispersion spectra in the frequency-velocity (*f*-*v*) domain, the corresponding shot gathers in the offset-time (*x*-*t*) domain also exhibit good agreement between the data and the model predictions. The match is particularly good for earlier arrivals in the shot gathers. The long-period, late-arriving wavelets are partially predicted by the models, but the model-predicted shot gathers are generally simpler than the data, indicating that the deeper subsurface structures may contain more features than what the current model parameterization can depict.

Although the inverted model profiles do not provide perfect fits to the data, they are able to predict predominant features of the wavefields. Given that our full-wavefield inversion requires very little prior information while being able to provide good data fits, the method is a powerful tool for seismic delineation of saline permafrost.

Table 3.4 Summary of the inverted V_S profiles.

Line index	Layer description	depth (m)	V_S (m/s)
1	Uniform top layer	0–5.0	1839.5
	Spline-based mid-layer	5.0–13.4	301.1–997.7
	Uniform half-space	13.4–∞	1165.4
2	Uniform top layer	0–1.0	1777.8
	Spline-based mid-layer	1.0–33.1	438.9–999.4
	Uniform half-space	33.1–∞	619.8
3	Uniform top layer	0–5.7	1968.7
	Spline-based mid-layer	5.7–29.8	372.3–920.4
	Uniform half-space	29.8–∞	889.6
4	Uniform top layer	0–1.8	1909.5
	Spline-based mid-layer	1.8–41.0	528.8–998.0
	Uniform half-space	41.0–∞	939.2

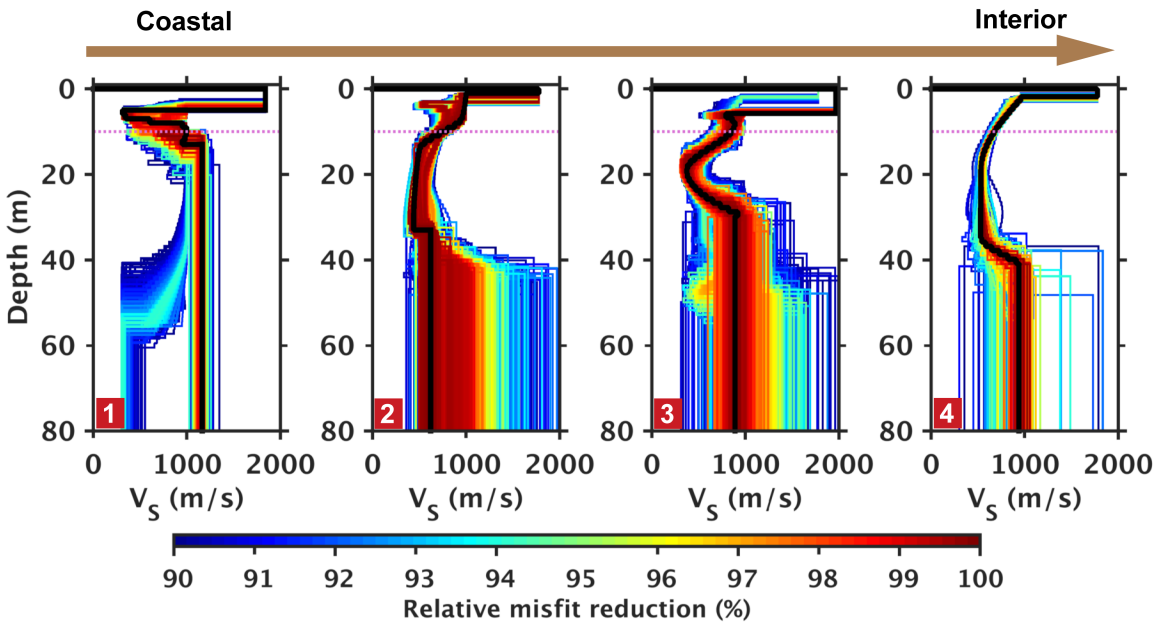

Figure 3.6 Side-by-side displays of the optimal model ensembles, each containing the 10% of the model profiles sampled by PSO. The black, bold profile denotes the global optima returned by PSO. The purple dashed lines mark the depth of the zero annual amplitude (~10 m).

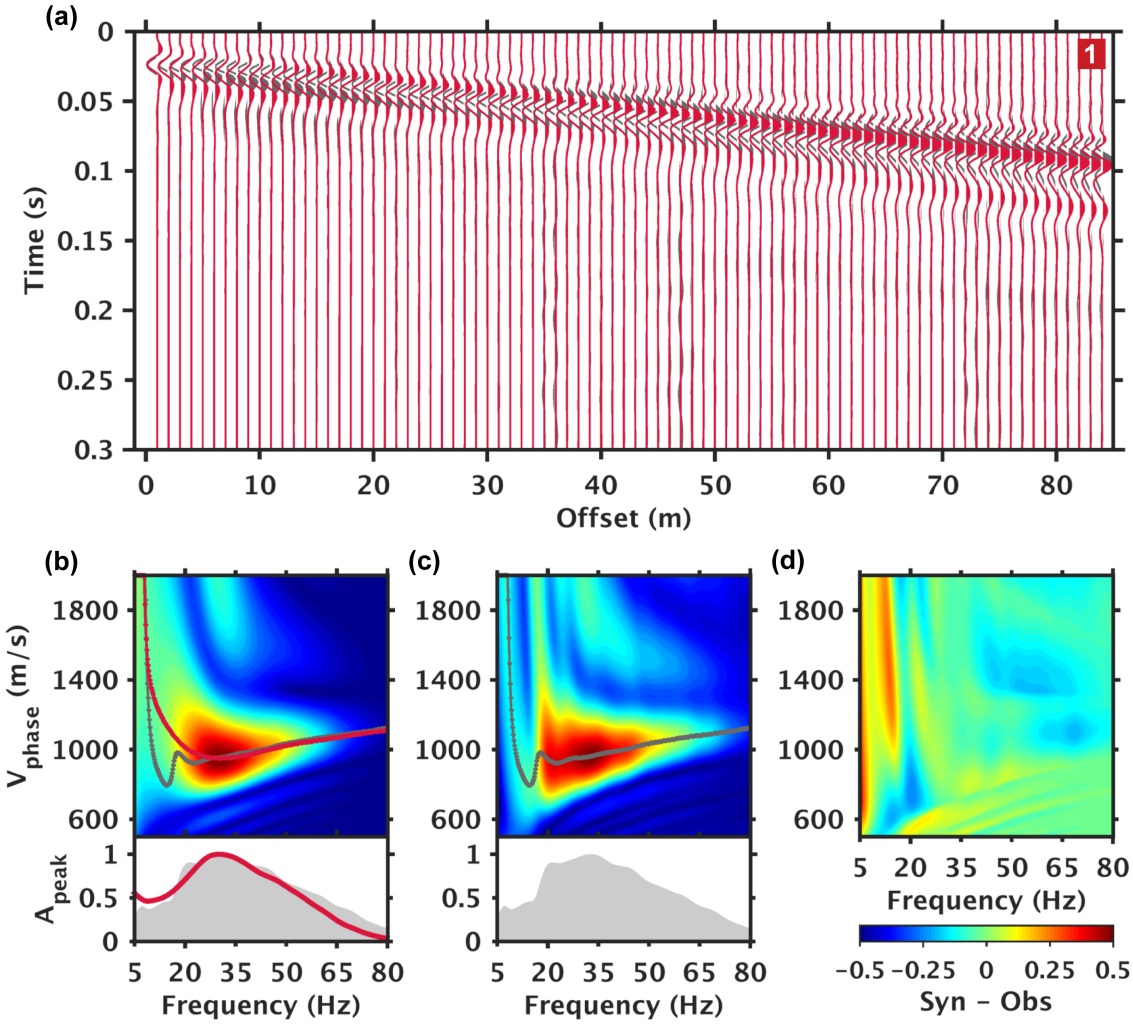

Figure 3.7 Data fits illustration for line 1 in Figure 3.1. (a) Overlay of the observed (in gray) and the synthetic (in red) shot gathers. (b) Dispersion spectrum of the synthetic wavefield (pseudocolor image) and overlapping comparisons between the observed (in gray) and the synthetic (in red) spectral maxima. (c) Dispersion spectrum and spectral maxima of the observed wavefield. (d) Difference between the observed and the synthetic dispersion spectra.

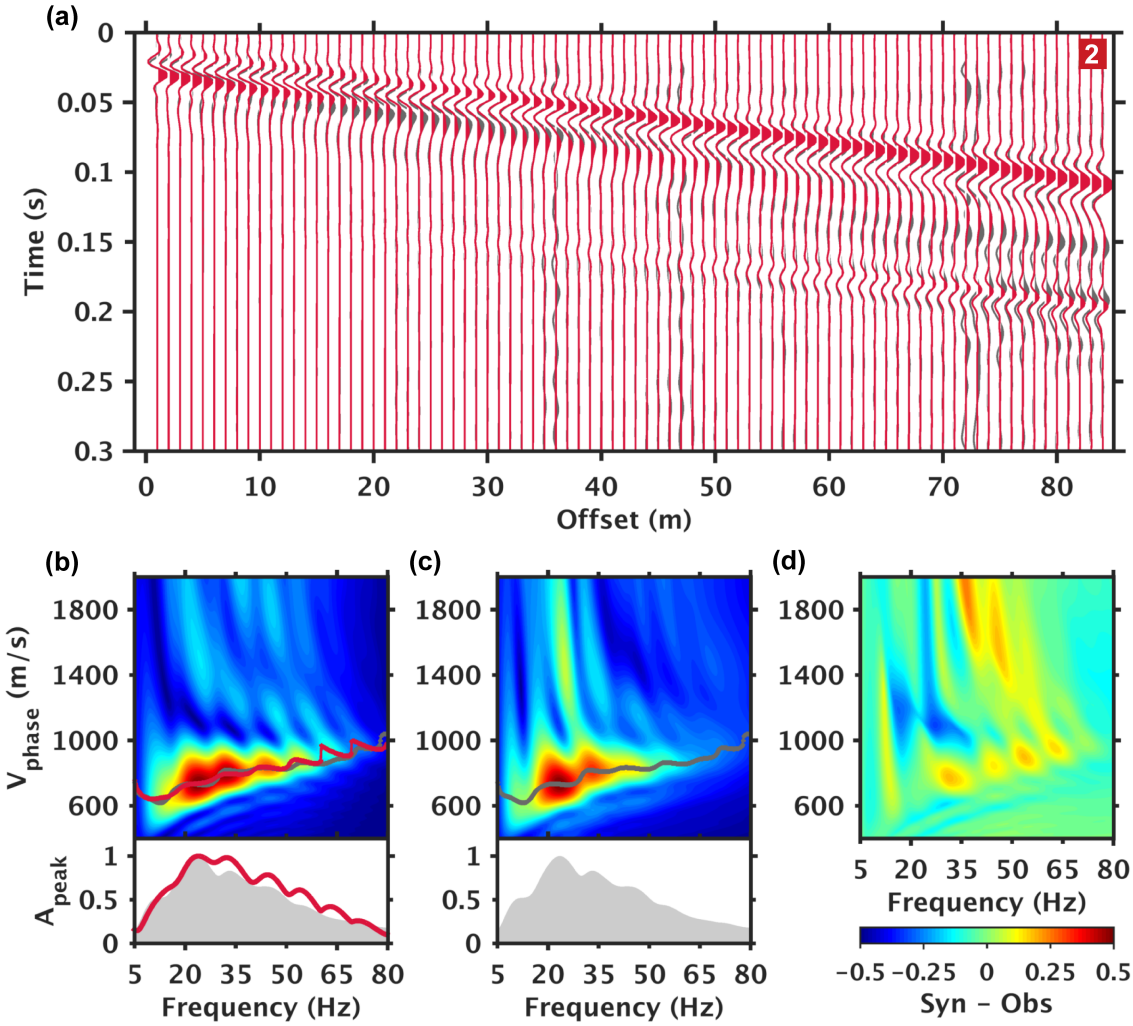

Figure 3.8 Data fits illustration for line 2 in Figure 3.1. (a) Overlay of the observed (in gray) and the synthetic (in red) shot gathers. (b) Dispersion spectrum of the synthetic wavefield (pseudocolor image) and overlapping comparisons between the observed (in gray) and the synthetic (in red) spectral maxima. (c) Dispersion spectrum and spectral maxima of the observed wavefield. (d) Difference between the observed and the synthetic dispersion spectra.

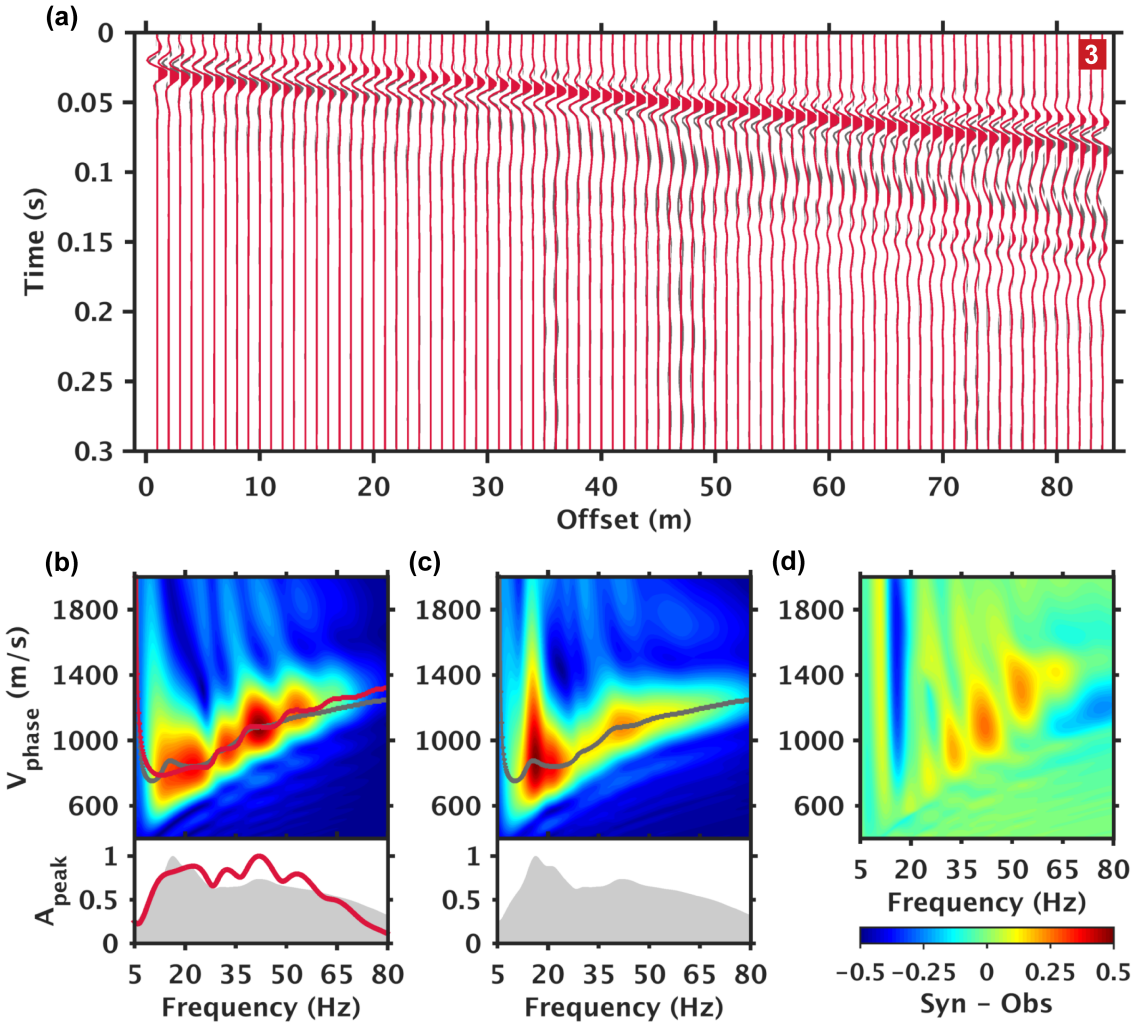

Figure 3.9 Data fits illustration for line 3 in Figure 3.1. (a) Overlay of the observed (in gray) and the synthetic (in red) shot gathers. (b) Dispersion spectrum of the synthetic wavefield (pseudocolor image) and overlapping comparisons between the observed (in gray) and the synthetic (in red) spectral maxima. (c) Dispersion spectrum and spectral maxima of the observed wavefield. (d) Difference between the observed and the synthetic dispersion spectra.

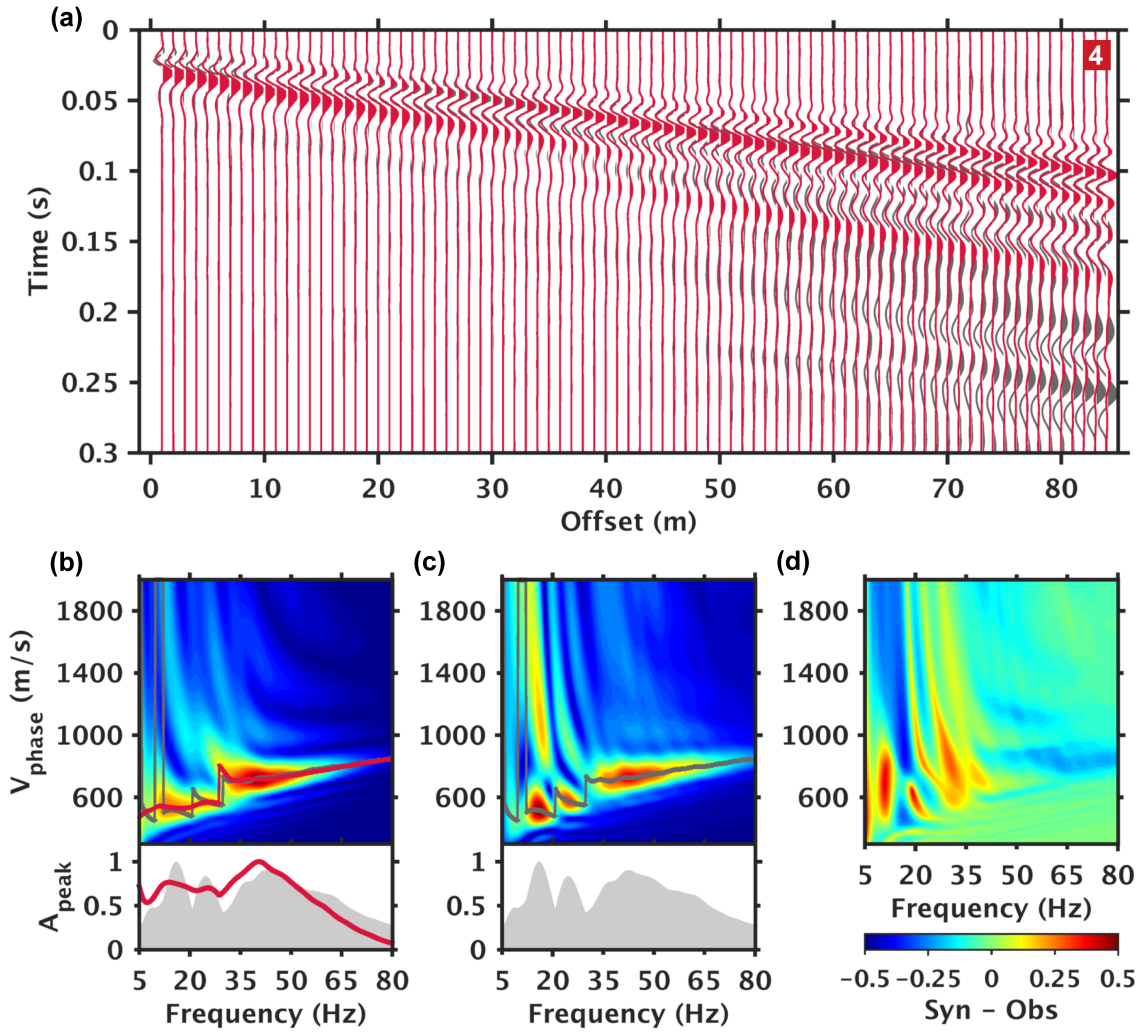

Figure 3.10 Data fits illustration for line 4 in Figure 3.1. (a) Overlay of the observed (in gray) and the synthetic (in red) shot gathers. (b) Dispersion spectrum of the synthetic wavefield (pseudocolor image) and overlapping comparisons between the observed (in gray) and the synthetic (in red) spectral maxima. (c) Dispersion spectrum and spectral maxima of the observed wavefield. (d) Difference between the observed and the synthetic dispersion spectra.

3.5 Discussion

3.5.1 Influences of attenuation on the plausible depth extent of the saline permafrost layer

The high computational costs of the full-wavefield inversion limit the number of model parameters we can invert for. Following the rule of parsimony, we have excluded attenuation parameters from the inversion and focus only on the elastic parameters. However, laboratory studies have reported that strong attenuation is present in saline sediments that are partially frozen (Matsushima et al. 2011a). It is therefore necessary to address possible influences of attenuation on the inversion results.

In particular, we are interested in the trade-offs between the attenuation of the mid-layer and the velocities of the basal half-space, as the latter are indicative of whether or not the bottom of the saline permafrost layer has been detected. If the basal velocities are comparable to those of the high-velocity top layer, the half-space should be non-saline and frozen, and thus the top of the half-space would coincide with the bottom of the saline permafrost layer. The half-space velocities in our elastic inversion results (Figure 3.6 and Table 3.4), however, are 36.6%–65.1% lower than the top-layer velocities, while the corresponding ground temperatures are as low as −9°C to −5°C (Figure 3.11; V. Romanovsky, personal communication, 2013). One explanation for such low velocities is that the half-space corresponds to partially frozen saline permafrost. In other words, the bottom of the saline permafrost layer is deeper than the investigation depth allowed by our field data. An alternative explanation is that the inverted half-space velocities are lower than the true velocities as a result of neglecting attenuation in the inversion.

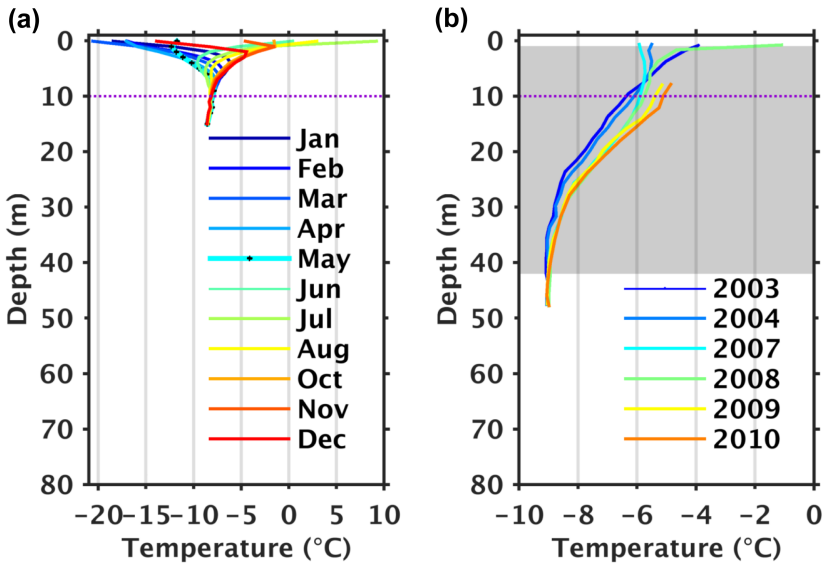

Figure 3.11 Temperature measurements at nearby borehole (Barrow 2; V. Romanovsky, personal communication, 2013). (a) Month-to-month temperature measurements. (b) Average annual ground temperature. The purple dashed lines denote the depth of the zero annual amplitude (~10 m). Shaded area in (b) marks the depth range of the low-velocity mid-layer (1.0 to 41.0 m) in the inversion results.

To examine the possible influences of attenuation, we set up a synthetic test using the following three models that only differ from each other in their basal half-space velocities and mid-layer attenuation:

- Model 1 (Figure 3.12b): Elastic model with identical velocities between the top layer and the half-space at the bottom.
- Model 2 (Figure 3.13b): Viscoelastic model with low Q values in the mid-layer ($Q_{P2} = Q_{S2} = 10$) and the same velocity structure as model 1.
- Model 3 (Figure 3.14b): Elastic model with half-space velocity that is only slightly higher than the portion of the mid-layer that is immediately above.

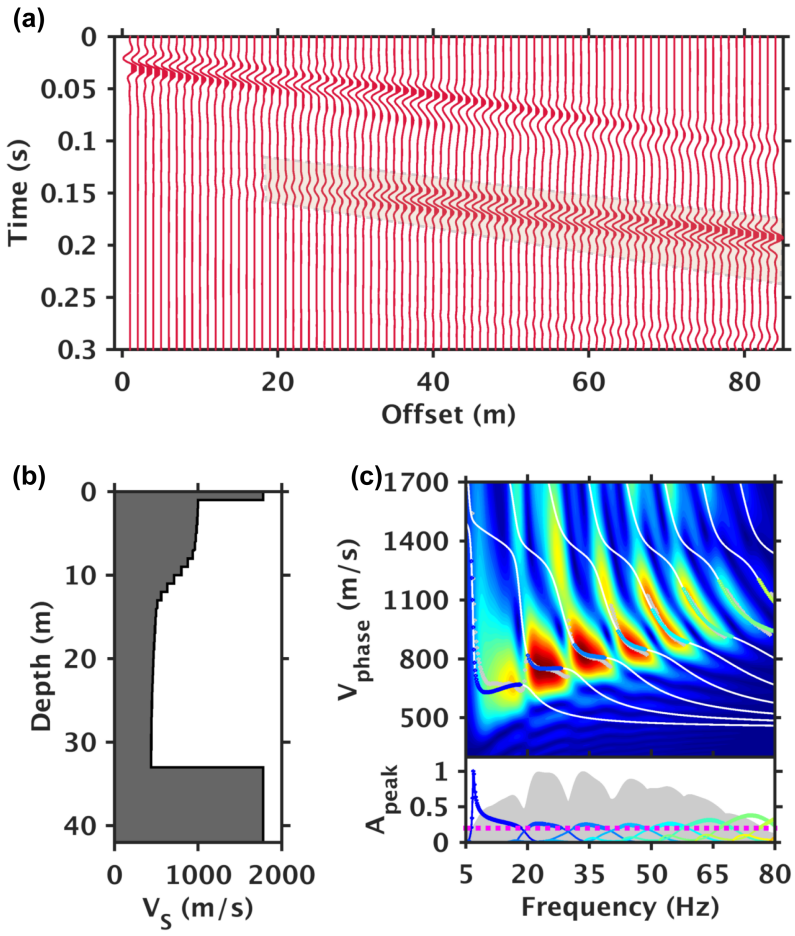

Figure 3.12 Synthetic tests for examining possible influences of attenuation: model 1—elastic model with identical velocities between the top layer and the half-space at the bottom). (a) The synthetic shot gather in the offset-time (*x*-*t*) domain. The shaded area marks late arrivals that signal the presence of a positive velocity contrast at depth. (b) The S-wave velocity (V_S) profile. (c) The synthetic dispersion spectrum (pseudocolor image) superimposed with theoretical modal curves (white lines). The lower panel in (c) shows the observed spectral peak at each frequency (shaded with gray); the colored curves show the model-predicted modal dispersion curves and the surface displacement distribution. The colored dots in the upper panel of (c) denote the (*f, v*) positions of the modes whose model-predicted surface displacement exceed a pre-defined threshold of detectability (marked with the purple dashed line in the lower panel).

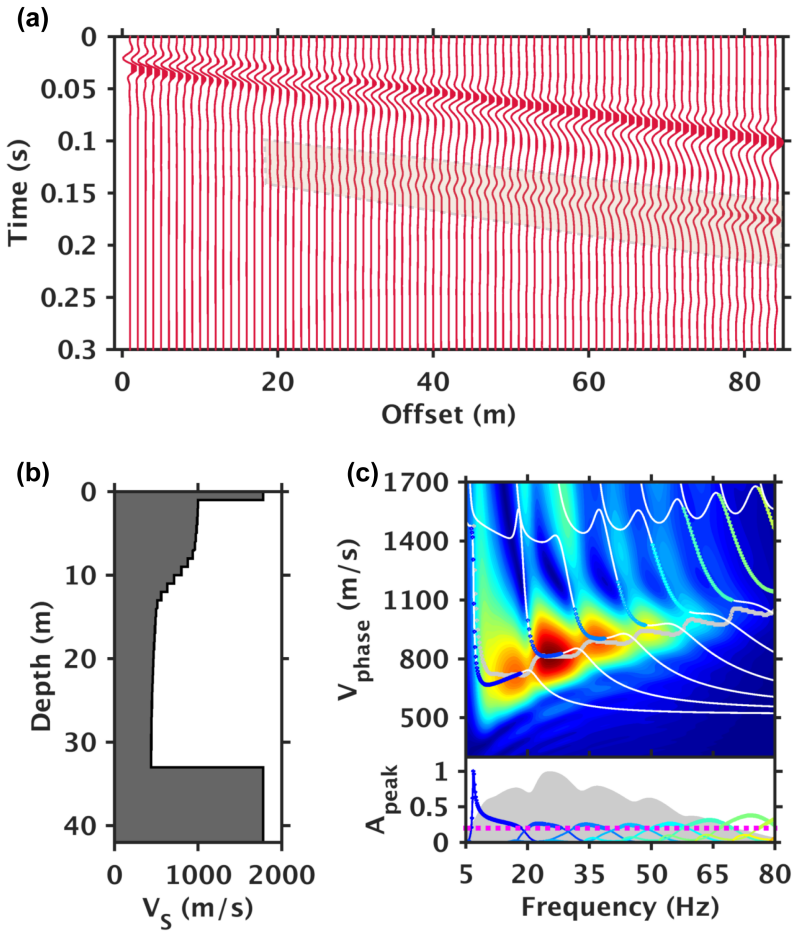

Figure 3.13 Synthetic tests for examining possible influences of attenuation: model 2—Viscoelastic model with low Q values in the mid-layer ($Q_{P2} = Q_{S2} = 10$) and the same velocity structure as model 1. (a) The synthetic shot gather in the offset-time (*x*-*t*) domain. The shaded area marks late arrivals that signal the presence of a positive velocity contrast at depth. (b) The S-wave velocity (V_S) profile. (c) The synthetic dispersion spectrum (pseudocolor image) superimposed with theoretical modal curves (white lines). The lower panel in (c) shows the observed spectral peak at each frequency (shaded with gray); the colored curves show the model-predicted modal dispersion curves and the surface displacement distribution. The colored dots in the upper panel of (c) denote the (*f, v*) positions of the modes whose model-predicted surface displacement exceed a pre-defined threshold of detectability (marked with the purple dashed line in the lower panel).

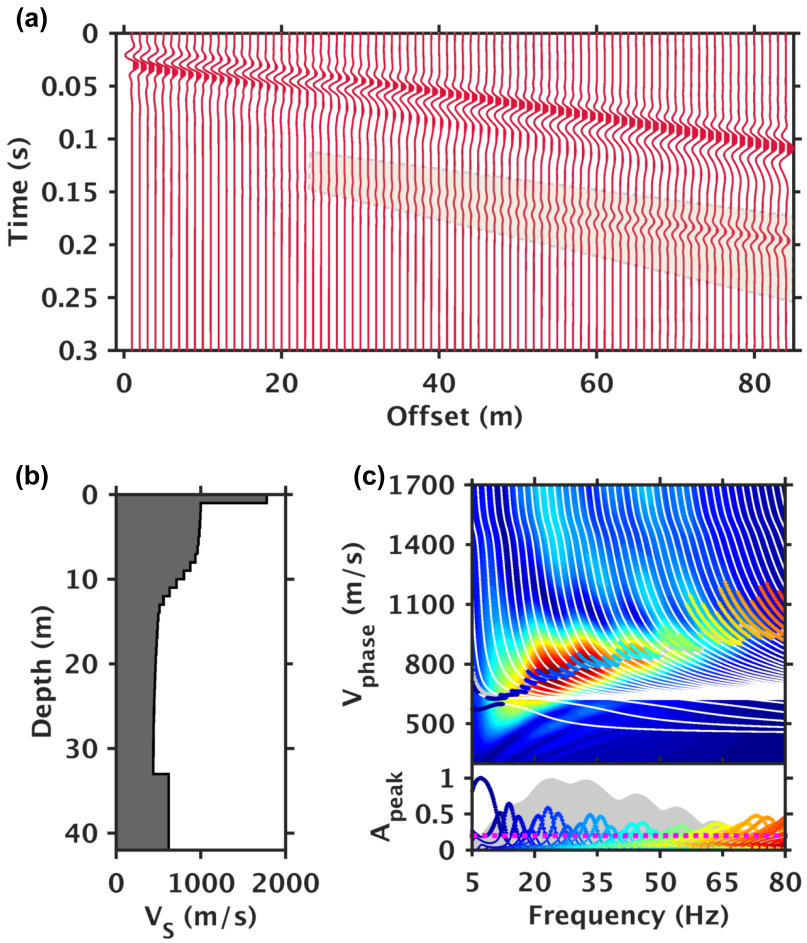

Figure 3.14 Synthetic tests for examining possible influences of attenuation: model 3—elastic model with half-space velocity that is only slightly higher than the portion of the mid-layer that is immediately above). (a) The synthetic shot gather in the offset-time (*x*-*t*) domain. The shaded area marks late arrivals that signal the presence of a positive velocity contrast at depth. (b) The S-wave velocity (V_S) profile. (c) The synthetic dispersion spectrum (pseudocolor image) superimposed with theoretical modal curves (white lines). The lower panel in (c) shows the observed spectral peak at each frequency (shaded with gray); the colored curves show the model-predicted modal dispersion curves and the surface displacement distribution. The colored dots in the upper panel of (c) denote the (*f*, *v*) positions of the modes whose model-predicted surface displacement exceed a pre-defined threshold of detectability (marked with the purple dashed line in the lower panel).

The test results show that the elastic model with a high-velocity basal half-space (model 1) yields a shot gather containing late arrivals that are distinctly strong (Figure 3.12 a), and a dispersion spectrum that is dominated by highly discrete spectral highlights (Figure 3.12c). By contrast, as shown in Figure 3.3, the observed shot gathers show late arrivals that are discernible but relatively weak, and the spectral highlights of the corresponding dispersion spectra are smoother and largely connected. Such mismatch in

the wavefield characteristics suggests that under the elastic assumption, a high-velocity basal half-space is implausible.

On the other hand, if we keep the same velocity configuration but assign strong attenuation to the mid-layer (model 2 in Figure 3.13b), the resulting wavefield shows similar characteristics as those of the field data (Figure 3.13a and 3.13c). Similar wavefield is also produced from model 3 (Figure 3.14b), an elastic model that has similar structure as our inversion results.

In short, strong trade-offs exist between the attenuation of the mid-layer and the velocities of the basal half-space. Unfortunately, so far we are not yet able to successfully invert for the attenuation structure using the field data. Given the limited resolving power regarding the attenuation, presently we cannot distinguish the following two categories of models:

- Models with 1) negligible attenuation, 2) relative low velocity in the basal half-space, and 3) small velocity increase near the top of the basal half-space. In this case, the bottom of the saline permafrost layer is deeper than the investigation depth ($\text{depth}_{\max} \approx \lambda_{\max} \approx x_{\max} =$ 84 m) and thus is not detected by the field data.
- Models with 1) strong attenuation, 2) high velocities in the basal half-space, and 3) large velocity increase near the top of the basal half-space. In this case, the bottom of the saline permafrost layer coincides with the top of the high-velocity basal half-space and thus could have been detected by the field data.

However, despite that we cannot draw definitive conclusions regarding the maximum depth of the saline permafrost layer, we can deduce that the bottom of the saline layer should at least be as deep as the top of the basal half-space obtained from our elastic inversion results. Such depth values, which fall in the range of 13.4–41.0 m, make the saline permafrost layer a pronounced subsurface feature that should require special treatment when estimating the overall response of the permafrost system in a warming climate.

3.5.2 What can the lack of lateral trends tell us about the evolutions of the saline permafrost layer?

As described earlier in the section "Inversion results", no noticeable correlations exist between the characteristics of the V_S profiles and how far away the survey lines are away from the coastline (Figure 3.6). We can draw the same conclusion when directly inspecting the effective dispersion curves (i.e., the (*f, v*) points of the dispersion spectral peaks at each frequency) that are extracted from the data (Figure 3.15). Given its lack of systematic lateral trends, pronounced volume, and persistent presence along the 4300-meter-long transect, the saline permafrost layer is unlikely to be solely caused by present-day seawater incursions. Instead, it is more likely to be a cumulative product of multiple transgressions and regressions of the Arctic Ocean.

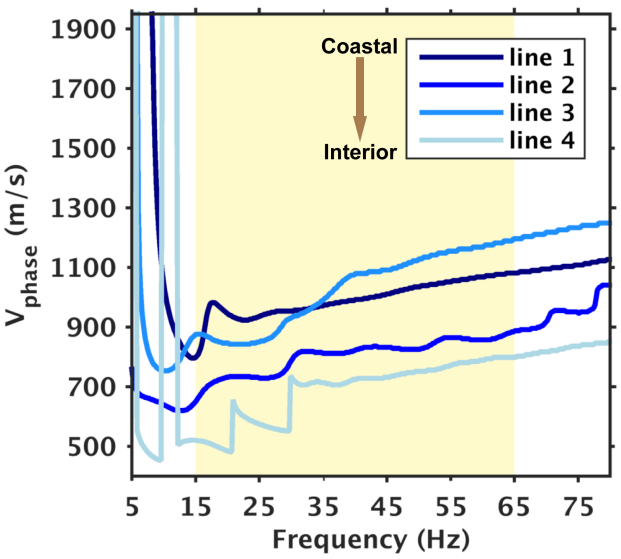

Figure 3.15 The effective dispersion curve layout (no correlation with the distance to the coast).

The repeated marine transgressions and regressions may also explain the velocity variations in the mid-layer of the inverted velocity profiles. Each occurrence of the transgressions could result in a saline, low-velocity interval, and similarly, each occurrence of the regressions could yield a less saline interval that has higher velocities. Such alternating structures could be modulated further by the surrounding hydrogeological conditions, and eventually exhibit velocity structures depicted by our inversion results.

3.6 Conclusion

To summarize, by using multichannel surface-wave methods, we are able to detect a persistent presence of embedded partially-frozen/unfrozen saline permafrost along the 4300-meter-long transect that runs across the BEO site, which demonstrates the marked lateral extent of saline permafrost at BEO. The V_S profiles obtained from the full-wavefield inversion reveal that the saline permafrost layer has pronounced vertical extent (at least ~8–39 m thick), hence making it a significant constituent of the near-surface strata at BEO. Given that, the permafrost structures at BEO could indicate that a considerable portion of the permafrost along the polar coasts could have pervasive partially-frozen saline permafrost. Because partially-frozen permafrost are highly sensitive to temperature disturbances, these coastal saline permafrost could degrade at an accelerated pace in a warming climate and eventually intensify the positive feedback between climate change and permafrost degradation. Therefore, an important implication of our results is that the presence of saline permafrost should be taken into account in climate modeling endeavors.

This study also marks preliminary success in seismic delineation of near-surface permafrost. Our workflow benefits from the use of cylindrical slant stack in the dispersion analysis, the spectra-based objective function in the inversion, and the parallel-enabled PSO algorithm in solving the inverse problem. The cylindrical slant stack naturally takes into account the curvature of the near-offset wave front. As a result, unlike

plane-wave-based methods that often require near-offset traces to be excluded so as to avoid near-field biases, the cylindrical slant stack allows proper use of the near-offset traces and thus increases the usable signal content of the data. The spectra-based objective function makes surface-wave methods applicable to irregularly dispersive wavefields for which the conventional, dispersion-curve-based methods become ineffective. The parallel-enabled PSO algorithm markedly improves the efficiency of the inversion, and thus allows the inverse problem to include more model parameters for a more detailed subsurface depiction.

However, we also face two major challenges. First, acquiring seismic data in permafrost environment is labor-intensive and time-consuming, which limits the data coverage that is achievable in non-industrial seismic surveys. Second, the computational costs of the full-wavefield approach are high. To keep the computation affordable, model parameterization must be parsimonious, which inherently limits the resolving power of the inversion.

Despite the limitations mentioned above, this study demonstrates that our workflow is effective in detecting and delineating saline permafrost while requiring little prior knowledge about the subsurface. In short, the workflow has a promising outlook for seismic applications concerning near-surface permafrost.

4. A rock physics investigation of unconsolidated saline permafrost: P-wave properties from laboratory ultrasonic measurements

Submitted as: Dou, S., S. Nakagawa, D. Dreger, and J. Ajo-Franklin, A rock physics investigation of unconsolidated saline permafrost: Geophysics (*submitted*).

4.1 Introduction

Saline permafrost is widespread in subsea and coastal areas of the Arctic, where residual salts originate from marine deposits and/or seawater incursions (Brouchkov 2002, 2003, Hivon and Sego 1993, Ingeman-Nielsen et al. 2008, Osterkamp 1989). Due to freezing-point depression caused by dissolved salts, saline permafrost is typically not fully frozen unless the eutectic point (~−21°C for NaCl solution) is reached. Given that mean annual Arctic ground temperatures are rarely lower than the eutectic point of such solutions, natural saline permafrost is typically only partially frozen.

As a system in which both pore water and ice phases coexist in a delicate equilibrium, partially frozen saline permafrost is highly sensitive to temperature disturbances. Unlike non-saline permafrost that is largely stable at sub-zero temperatures, saline permafrost can start thawing at temperatures that are well below 0 °C. Moreover, saline permafrost has a lower mechanical strength because less ice is available for bonding the sediment grains together. Consequently, saline permafrost is very susceptible to deformation and thaw-induced settlement (Hivon and Sego 1995, Nixon and Lem 1984, e.g., Ogata et al. 1983) and presents a geotechnical hazard for infrastructure. Brouchkov (2003) reported that 25%–50% of the buildings along the Russian Arctic coast have deformed and cracked because of construction on top of deforming strata including saline-permafrost.

In order to better assess and mitigate geohazards related to saline permafrost, knowledge of their spatial distributions is required. In this context, subsurface mapping utilizing geophysical approaches is indispensable. In addition, if we are to predict the future impacts of saline permafrost degradation in a warming climate, associated properties including ice content and salinity are required due to their central role in determining response to thermal perturbations (e.g., Daanen et al. 2011). Seismic methods are capable of mapping permafrost structures at spatial scales of geotechnical interest (tens to hundreds of meters both laterally and vertically). In previous permafrost studies, seismic velocities are used for property inference (e.g., Hilbich 2010, Miller et al. 2000, Ramachandran et al. 2011) due to the positive correlation between the ice content and the seismic velocities: Generally, the higher the ice content, the higher the velocities observed in prior studies (e.g., Nakano and Arnold 1973, Zimmerman and King 1986). Moreover, seismic velocities are often correlated with compressive strength in permafrost soils, a key parameter in engineering practice (Schön 2011). Besides velocities, seismic attenuation values (e.g., Q) are also sensitive to the ice content (Matsushima et al. 2011a,

2011b, e.g., Nakano and Arnold 1973) and thus might assist in better delineating permafrost structures.

For mapping saline permafrost, the ice-content dependencies of seismic properties are especially critical, since differences in ice content are realizable through the associated differences in seismic properties. Saline permafrost, given its lower ice content, can be detected as a low-velocity anomaly within a high-velocity background of non-saline permafrost (Collett and Bird 1988, 1993, Dou and Ajo-Franklin 2014).

For estimating the pore-water salinities of saline permafrost, seismic methods can also be useful, because seismic properties and salinities are related via the ice content. That is, we should be able to infer salinities from seismic properties by relaying the following two relationships: (1) the salinity- and temperature-dependent variations of ice content and (2) the ice-content dependencies of seismic properties. The former can be established with the help of the phase diagrams of salt solutions (e.g., Andersland and Ladanyi 2004, Hivon and Sego 1995). The latter, a key component in the rock physics of saline permafrost, should be established based upon seismic data that correspond to a broad range of ice content. Laboratory experiments, by allowing measurements to be conducted under controlled conditions, can provide data for this purpose.

Prior experiment studies have largely focused on consolidated sedimentary rocks (Desai and Moore 1967, Pandit and King 1978, 1979, Sondergeld and Rai 2007), whereas predominant portions of near-surface saline permafrost units consist of unconsolidated sediments. To date, only two published laboratory studies address the effects of pore-water salinity on unconsolidated frozen sediments: King et al. (1982) provides data on subsea permafrost samples while Matsushima et al. (2011a) explores the properties of brine-saturated quartz sand. Both studies demonstrated that the presence of saline pore water can cause marked reductions in seismic velocities. Nevertheless, because only limited ranges of temperatures and salinities were tested, these studies are unable to provide a dataset for a systematic examination of seismic properties in unconsolidated saline permafrost.

In this study, we conducted laboratory ultrasonic measurements to investigate P-wave properties of saturated, unconsolidated saline permafrost. Our primary goal was to produce data probing seismic properties over wide ranges of salinities and temperatures. We used coarse-grained sand packs saturated with water or NaCl solutions of various concentrations (0.0–2.5 M; 0–13 wt%) to systematically examine the influences of pore-water salinities. In addition, we carried out measurements on a fine-grained saline permafrost core sample (0.7 M; 42 wt%) to evaluate surface and pore-size mediated effects (i.e., supercooling of pore water caused by capillary and adsorption effects) in fine-grained sediments. During each set of the measurements, we acquired P-wave signals continuously at 10-minute intervals while slowly changing the sample temperatures over the range from 10 °C to −30 °C.

To better understand the key rock physics relationships between ice content and seismic measurables, we analyze the observed P-wave properties of the sand samples as functions of ice content. The resulting datasets, along with their implications on the probable pore-scale distributions of ice, provide a valuable basis for rock physics modeling, which in turn paves the way for inferring salinities of saline permafrost from seismic measurements.

4.2 Experiment system, materials, and procedure

4.2.1 Ultrasonic pulse-transmission system

An ultrasonic pulse-transmission system (Figure 4.1) was utilized for our laboratory experiments. An upright cylindrical acrylic column (internal diameter, 65.3 mm; height, 150 mm) was used both as a sample container and a mounting frame for ultrasonic and temperature sensors. Two levels of instrument ports were attached to the sidewall of the column at the heights of 42 mm and 73 mm (relative to the base of the column). Each level consisted of two ultrasonic transducer ports and one thermocouple port: The two transducer ports, one for the transmitter and the other for the receiver, were positioned at the opposite sides about the symmetry axis of the column, so that the acquired signals were P waves propagating along the diameter direction of the cylindrical sample; the thermocouple port, through which a thermocouple probe was inserted into the sample, was placed at 90 degrees away from the transducer ports.

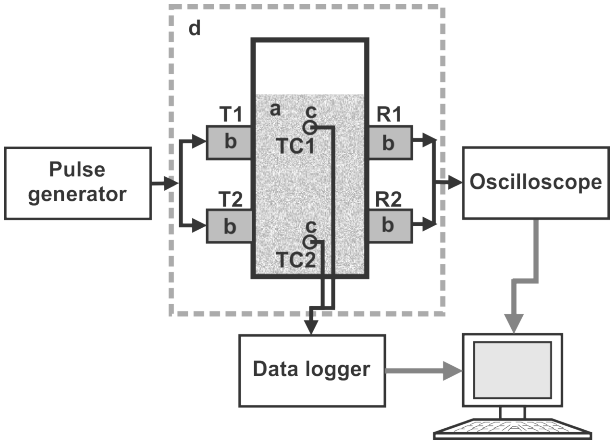

Figure 4.1 Schematics of the ultrasonic pulse-transmission system. a, sample column; b, ultrasonic transducers; c, thermocouples; d, benchtop freezer; T, Transmitters; R, Receivers; TC, Thermocouples.

A square-wave pulse generator (Panametrics 5077PR) was utilized to provide high-voltage (100−400 V), high-frequency (central frequency 1 MHz) excitation signals for the ultrasonic transducers. Immersion-type transducers (central frequency, 1MHz; Panametrics V303-SU), which allow good acoustic coupling between the transducers and the saturated samples, were used for transmitting and receiving ultrasonic signals. The through-transmission ultrasonic signals were acquired using a digital oscilloscope (Tektronix TDS 210) and saved on a control PC for analysis.

4.2.2 Experimental materials

Pore-water salinities and surface effects (i.e., unfrozen water retention caused by capillary and adsorption effects) both influence ice content in saline permafrost. To isolate the influences of pore-water salinity, we first made measurements on coarse sand samples for which surface effects are largely negligible. Then, to examine the influences of surface effects in the presence of saline pore water, we also carried out measurements on a fine-grained saline permafrost core sample (extracted from the Barrow Peninsula on

the Alaskan Arctic Coastal Plain), in which the silt and clay particle size fractions could yield pronounced surface effects that impact freeze/thaw behavior.

Saturated, coarse-grained Ottawa sand

Standard 20−30 Ottawa sand (quartz; graded between No. 20 and No. 30 sieves, grain size 600−850 μm, D_{50} ~720 μm) was used to make fully saturated sand packs. Five saline sand samples, each saturated with NaCl solution of desired salinity, were used in five individual tests that targeted various levels of pore-water salinities. The salinities of the five NaCl solutions were chosen to represent brackish (0.1 M and 0.3 M, lower salinity than seawater), moderately saline (0.6 M, typical salinity of seawater), and hypersaline (1.0 M and 2.5 M, higher salinity than seawater) permafrost. In addition, a non-saline sample (saturated with distilled water) was used as a baseline for contrasting the results in the presence and absence of dissolved salts. The initial porosity of the saturated sand packs was ~36 vol%.

Saturated, fine-grained saline permafrost core sample

The fine-grained saline permafrost core sample used in our experiment is classified as a silty-clayey sand (D_{50} ~53μm) consisting of 52 vol% of sand, 30 vol% of silt, and 18 vol% of clay (information about the texture analysis is detailed in Appendix A1). The sample was taken from the bottom section (depth 1.85−2.80 m) of a 3-meter-long permafrost core that was extracted from the Barrow Peninsula on the Alaskan Arctic Coastal Plain. At the time of coring, the *in situ* ground temperatures were as low as −10 °C to −8 °C, but the core sample was only partially frozen because its pore water is saline.

To prevent complications related to heterogeneity and sample saturation state, the core sample was processed via re-saturation, homogenization, repacking, and vacuum de-air steps. The core sample was first thawed in a 4°C refrigerator. From the fully thawed sample, the electrical conductivity of the pore water was measured. Next, a small amount of a NaCl solution whose electrical conductivity matched that of the pore water was mixed into the thawed sample for re-saturation. The mixture was thoroughly homogenized and then packed into the column. Finally, a vacuum was applied to the sample to remove any residual air. The post-packing electrical conductivity of the pore water was measured to be 69.6 mS/cm. Assuming NaCl is the predominant salt, this conductivity value is equivaluent to a salinity of 0.7 M (slightly higher than typical salinity of seawater). The initial porosity of the repacked core sample was ~50 vol%.

4.2.3 Experimental procedure

Temperature control and monitoring

The column was placed inside a benchtop freezer containing a built-in temperature controller. In each set of the measurements, the freezer temperature was changed between 10 °C and −30 °C. The rates of the temperature change were kept slow (1°C every 2−4 hours) so that the sample approached a uniform temperature distribution. Sample as well as freezer temperatures were continuously recorded using a high-resolution data logger (Agilent 34970A) at 5-minute intervals.

Ultrasonic data acquisition

A computer-controlled oscilloscope was programmed to continuously acquire P-wave signals at 10-minute intervals. To increase the signal-to-noise ratio of the acquired signals via waveform stacking, a pulse generator was tuned to generate trigger pulses with a high repetition rate (100 pulses per second), which enabled a high stack count (128 vertical stacks). Each post-stack waveform was recorded by the oscilloscope at a sampling rate of 10 ns over a duration time of 75 μs.

Freeze-only and freeze-thaw measurements

The measurements were conducted under freeze-only or freeze-thaw conditions. For the freeze-only measurements, P-wave signals were acquired only when the sample underwent freezing (i.e., the sample temperatures were decreased from 10 °C to −30 °C). For the freeze-thaw measurements, P-wave signals were acquired while the sample was going through a freeze-thaw cycle (i.e., the sample temperatures were decreased and then increased between 10 °C and −30 °C).

In this experiment, the freeze-only measurements were conducted on five coarse sand samples (initial pore-water salinity = 0.0 M, 0.1 M, 0.3 M, 0.6 M, and 1.0 M), whereas the freeze-thaw measurements were only conducted on one coarse sand sample (initial pore-water salinity = 2.5 M) and the fine-grained saline permafrost core sample. To make the best use of available experimental time, freeze-thaw measurements were only selectively carried out to examine the characteristics of the freeze-thaw hystereses. Since freeze-thaw hysteresis effects are often more pronounced for fine-grained sediments (Nakano and Froula 1973), freeze-thaw measurements were conducted on the fine-grained saline permafrost core sample (target) and one of the coarse sand samples (reference).

4.3 Results

Here we present the results of our laboratory ultrasonic measurements as functions of temperature. We first focus on the results of the freezing measurements, which consist of the freeze-only measurements and the freezing subset of the freeze-thaw measurements. We organize these results into three subsections, each corresponding to one of the key factors that control the behavior of the data: (1) the progressions of the water-to-ice phase transitions, (2) the salinities of the pore water, and (3) the presence of fine-grained particles. Near the end of this section, as part of the analysis centering around the effects of grain size—in particular, the influences of the surface effects in the fine-grained saline permafrost core sample, we move on to analyzing the results of the freeze-thaw measurements, in which we use the behavior of the freeze-thaw hystereses as an indicator of the surface effects. Examples shown in this section are for the top sensor pair due to the high degree of uniformity shown between the two measurement locations.

4.3.1 The influences of water-to-ice phase transitions

As the temperatures of the samples gradually dropped below freezing, the freezing resulted in marked changes in the acquired P-wave signals. These changes, while being unique to each sample, exhibit shared features that are correlated with the physical states of the pore water/ice. In this subsection, we use P-wave signals obtained from one of the saline coarse sand samples (initial pore-water salinity = 0.6 M) as examples to demonstrate the influences of the water-to-ice phase transitions.

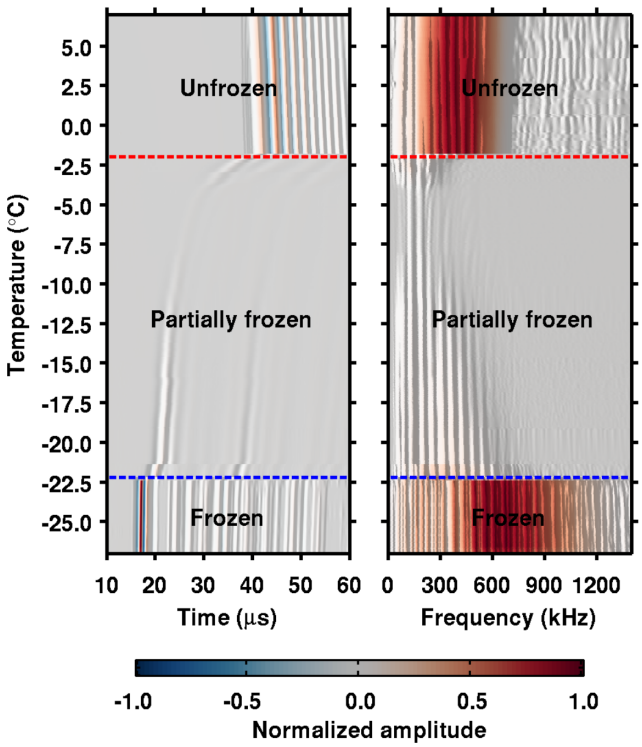

Figure 4.2 The evolution of the P-wave waveforms (left panel) and the corresponding amplitude spectra (right panel) over the course of a freeze-only measurement conducted on one of the saline coarse sand samples (initial pore-water salinity = 0.6 M). Relative amplitudes of the signals are preserved.

As can be seen in Figure 4.2, the temperature-dependent variations of the signal amplitudes (both the waveforms and the spectra) can be divided into three distinct segments, each corresponding to a specific state of the sample: (1) the intermediate amplitudes correspond to the unfrozen state (from 10.0°C to −2.0°C), (2) the low amplitudes correspond to the partially frozen state (from −2.0°C to −22.2°C), and (3) the high amplitudes correspond to the fully frozen state (below −22.2°C). The boundaries between the adjacent segments are sharp, which result from a rapid decrease and increase of the amplitudes near the freezing point (−2.0°C) and the eutectic point (−22.2°C), respectively.

Figure 4.3 shows a subset of traces to provide a more detailed view of waveform shape and spectral content. When the temperatures are above freezing, the signals are nearly unresponsive to the temperature changes (7.0 °C and −1.0 °C in Figure 4.3). Once the temperatures fall below freezing, the signal shapes become distinctly different at different temperatures. The first cycle of the waveform arrives at successively earlier time as the temperature decreases, illustrating the monotonic increases in P-wave velocities. By contrast, the associated changes in the spectral contents do not show such monotonicity. Instead, the high-frequency contents of the spectra first diminish at temperatures that are immediately below the freezing point (e.g., −2.3 °C and −3.5 °C in Figure 4.3), and then gradually grow back as the temperatures decrease further (e.g., −12.6 °C in Figure 3). In the end, when the temperatures are below the eutectic point (e.g.,

−25.6 °C in Figure 3), the waveforms become impulsive and compact, and the spectra include a considerable amount of higher frequencies.

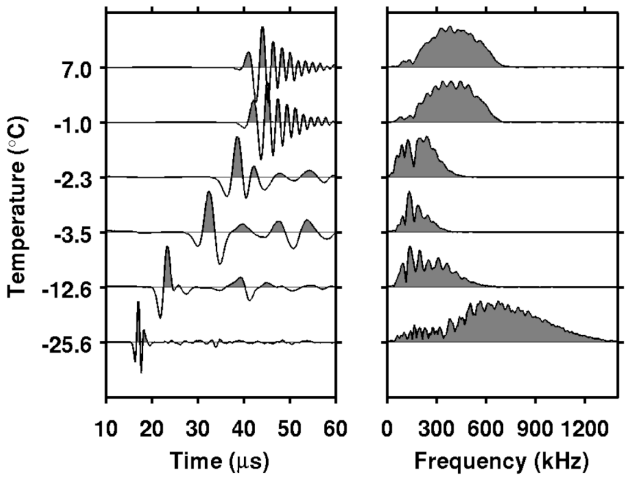

Figure 4.3 A subset of the normalized P-wave waveforms (left panel) and the corresponding amplitude spectra (right panel) extracted from a freeze-only measurement conducted on one of the saline coarse sand samples (initial pore-water salinity = 0.6 M).

4.3.2 The influences of pore-water salinity

Dissolved salts not only lower the freezing point of pore water, but also change how the amount of ice varies with respect to sub-freezing temperatures. As a result, P-wave properties of the samples respond strongly to the presence of dissolved salts. To systematically examine the influences of pore-water salinities, we combine all the data obtained from the six coarse sand samples (five saline samples and one non-saline sample) and present them as functions of temperature and initial pore-water salinity (Figure 4.4).

We first look at the data obtained from the saline samples, for which the freezing process consists of two stages. The first stage starts at the freezing point and ends at the eutectic point. This stage is progressive, because the dissolved salts remain in the residual pore water and thus further depress the freezing point. The second stage corresponds to temperatures that are immediately below the eutectic point. This stage is rapid, because the salts quickly precipitate out of the residual pore water and thus can no longer suppress freezing. To examine the characteristics of this two-stage freezing, and to compare the behaviors of the data between before and after freezing, we use two reference temperatures, 0 °C (the freezing point of water) and −21.3 °C (the eutectic point of NaCl aqueous solution), as dividers to break down the results into three parts, each of which corresponds to a distinct stage of the cooling process:

1) Above 0 °C, all of the samples were unfrozen and thus were equivalent to binary mixtures of sediment grains and brine. In spite of the large differences in the initial pore-water salinities, the observed P-wave properties are largely similar among all the samples. The small intra-sample variations and inter-sample differences in the data can be attributed to the temperature- and salinity-dependent properties (compressibility, density, and viscosity) of the pore water. Overall, at this stage, the temperature-dependent variations of P-wave properties are only slightly sensitive to the initial pore-water salinities.

2) Between −21.3 °C and 0 °C the samples entered their first stage of freezing. The temperature-dependent behaviors of the P-wave properties exhibit large inter-sample differences as a result of the different initial pore-water salinities. The onset of freezing, marked by rapid rises of the velocities and sudden drops of the amplitudes and the centroid frequencies, occur at lower temperatures for samples with higher initial salinities, illustrating the positive correlation between the extent of freezing-point depression and the initial pore-water salinity. As freezing progresses further at sub-freezing temperatures, the data continue to exhibit temperature-dependent changes that are unique for each sample. In short, at this stage, the temperature-dependent variations of P-wave properties are basically dictated by the initial pore-water salinities.
3) Below −21.3 °C, the salts rapidly precipitated out of the residual pore water. Upon the loss of the dissolved salts, the second stage of freezing sets in and all the saline samples quickly became fully frozen. The onsets of freezing are marked by abrupt increases in the velocities, amplitudes, and centroid frequencies that occur immediately below −21.3 °C. As freezing progresses further at sub-eutectic temperatures, P-wave properties of all the samples soon converge towards narrow ranges, regardless of the different initial pore-water salinities. Such convergence indicates that the fully frozen samples resemble binary mixtures of sediment grains and ice. The precipitated salts, albeit being visible in the saline samples by the end of the freezing measurements, are too dilute to affect the P-wave properties. Hence, at this stage, the temperature-dependent variations of P-wave properties are largely independent of the initial pore-water salinities.

Next, we bring attention to the striking behavior of amplitudes and centroid frequency during the freezing process (Figure 4.4b). Once the temperatures fall below freezing, both the amplitudes and the centroid frequencies plunge, quickly reaching their minima within another temperature reduction of no more than ~5 °C. As the temperatures decrease further, both the amplitudes and the centroid frequencies slowly rebound, but the increase is limited before the second stage of freezing starts. As a result, the amplitudes and centroid frequencies remain low throughout the first stage of freezing, illustrating the presence of strong attenuation in the partially frozen saline samples. Interestingly, the attenuation signatures of the freezing onsets are different between the two stages. Whereas the onset of the first stage of freezing is accompanied by a sharp increase in the attenuation occurring immediately below the freezing point, the second stage of freezing starts with a rapid decline in attenuation near the eutectic point. This near-eutectic behavior of the attenuation is different from what was reported in the studies of Spetzler and Anderson (1968b) and Prasad and Dvorkin (2004), both of which examined the seismic attenuation of partially frozen brine and observed increased attenuation near the eutectic point. Such discrepancy may be related to the microstructural differences between the freezing of unconfined brine and the freezing of saline pore water.

Another curious phenomenon regarding the observed attenuation is that its sharp increase near the freezing point coincides with the rapid rise of the velocity. Such behavior of the data appears counterintuitive, given that increasing velocities often are accompanied by decreasing attenuation. In later parts of this paper, we will revisit the characteristics of the attenuation and expand the related discussion.

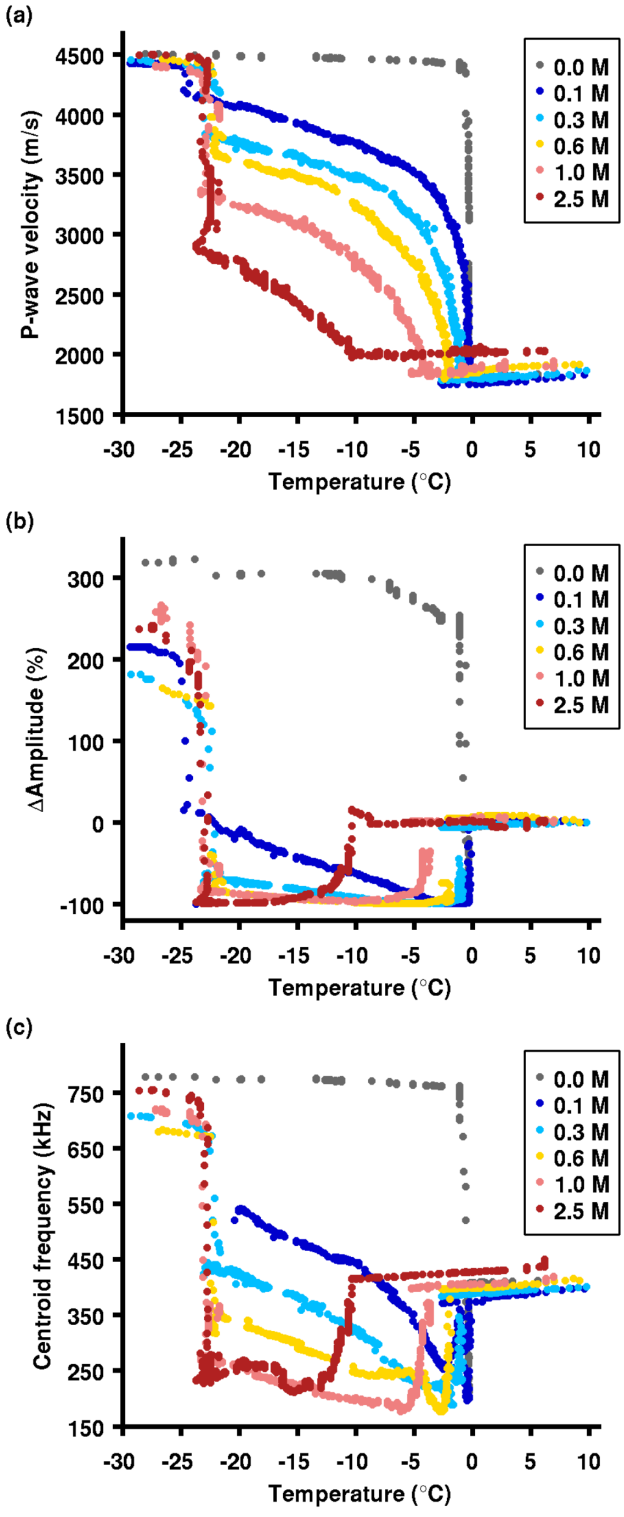

Figure 4.4 Temperature-dependent variations of P-wave properties obtained from the freezing measurements of saturated 20−30 Ottawa sand. (a) P-wave velocities, (b) relative peak-to-peak amplitudes (relative to the peak-to-peak amplitudes observed at 10°C), and (c) centroid frequencies.

Finally, we highlight the influence of the dissolved salts on P-wave properties, which is demonstrated by the drastic differences between the data obtained from the saline and non-saline samples. It is particularly remarkable that even a small amount of dissolved salts can severely reduce the P-wave velocities. For instance, for the sample with an initial pore-water salinity of a mere 0.1 M (1/6 of the typical seawater salinity), P-wave velocities are up to 12%−36% lower than those of the non-saline sample in the temperature range from −15 °C to −1 °C (Figure 4.4a).

4.3.3 The influences of fine-grained particles

In contrast with the uniformly sized coarse sand we have focused on to this point, the field core sample is a mixture of finer particles with nonuniform sizes and diverse shapes (contains spherical or angular shaped sand and silt, and platelet shaped clay, as detailed in the Appendix B1). These textural characteristics affect the porosity and the pore-scale structure of the core sample, which in turn should affect the values of the seismic measurables.

In addition, the surface effects of fine-grained particles tend to yield gradual, rampwise variations of seismic measurables with respect to near-freezing temperatures, in contrast to the steep, stepwise variations observed from coarse-grained samples (Li 2009, e.g., Nakano and Froula 1973). This is because surface effects locally depress freezing points with the smallest (nm) scale pores exhibiting the largest departure from free water; in such scenarios, capillary forces present in small pores and adsorption on grain surfaces can hold layers of water molecules in place, hence restraining these molecules from settling into ordered ice crystals. As temperature decreases further, some bound water will eventually turn into ice. But, overall, freezing/thawing becomes progressive, as bound water tends to freeze later and thaw earlier. As a result, the pore water no longer has a fixed, well-defined freezing point. Instead, freezing/thawing hovers over a range of sub-freezing temperatures, and the onsets of freezing are generally shifted towards lower temperatures.

Moreover, surface effects can cause seismic properties to exhibit freeze-thaw hysteresis, owing to the hysteretic changes in ice content. Such freeze-thaw hysteresis, often viewed as being analogous to the wetting-drying hysteresis observed in unfrozen sediments, are characteristic of the surface effects of fine-grained particles and small pores (Black and Tice 1989, Spaans and Baker 1996, Tian et al. 2014). For example, the study of Nakano and Froula (1973) has reported observations of freeze-thaw hysteresis in the temperature-dependent variations of P-wave velocities that were obtained from non-saline silt and clay. We view the presence and extent of the freeze-thaw hysteresis as an indicator of surface effects in our system.

One remaining question is whether the combination of dissolved salts and surface effects will work in concert to influence the temperature-dependent variations in ice content. The study of Yong et al. (1979) noted that dissolved salts could cause bound water films to collapse, and thus weaken the influences of surface effects. Nevertheless, the same study also pointed out that both the dissolved salts and surface effects should be taken into account when saline permafrost has high clay content and/or low pore-water salinities. The saline core sample used in our study, however, has moderate pore-water salinity (0.7 M, slightly higher than the typical seawater salinity) and relatively low clay content (18 vol%). In this case, we expect the influences of surface effects to be nearly

negligible in the presence of dissolved salts. In this subsection, we will test our expectation based upon the data obtained from the fine-grained core sample.

On freezing measurements

Figure 4.5 compares the data obtained from the freezing measurements conducted on the fine-grained saline permafrost core sample (0.7 M) against those of the coarse sand samples with neighboring pore-water salinities (0.6 M and 1.0 M). Because the salinity of the core sample is close enough to those of the two coarse sand samples, the influences of the dissolved salts should be comparable among all three data sets that are being compared here. In this way, the dissimilar behaviors of the data should help illuminate the influences of the grain-size differences.

As can be seen in Figure 4.5, the onset of the first stage of freezing, which is marked by a rapid rise in the velocities and sudden drops in the amplitudes and the centroid frequencies, occurs at −2.4 °C—a temperature that is consistent with the expected freezing point for an initial pore-water salinity of 0.7 M. Since the freezing point does not appear to be further lowered by the surface effects of the fine-grained particles, we conclude that the influences of the dissolved salts are predominant at near-freezing temperatures.

Throughout the first stage of freezing (from −2.4 °C to −21.3 °C), P-wave velocities measured from the fine-grained core sample exhibit temperature-dependent variations that are similar to those of the coarse sand samples (Figure 4.5a), indicating that the dissolved salts exert similar extent of influences on the data regardless of the grain-size differences. In addition, the amplitudes and the centroid frequencies are also markedly lower than the values associated with the nearly fully frozen stage of the sample (at temperatures that are below −32 °C), illustrating the presence of strong attenuation in the partially frozen saline core sample.

However, the influences of the smaller particle/pore size are also evident, as can be seen from the dissimilar behaviors of the data. For the fine-grained core sample, the onset of the second stage of freezing only becomes identifiable at −31.8 °C—a temperature that is well below the expected eutectic point (−21.3 °C). Moreover, in contrast with the data from the coarse sand samples that exhibit stepwise variations with respect to near-eutectic temperatures, the data of the core sample show gradual, rampwise changes following the onset of the second stage of freezing, illustrating the influences of the surface effects. P-wave velocities corresponding to the unfrozen and nearly fully frozen stages of the core sample are also lower than those of the coarse sand samples. The main cause of this difference could be that the porosity of the fine-grained core sample (~50 vol%) is higher than that of the coarse sand samples (~36 vol%).

Throughout the first stage of freezing, the temperature-dependent variations of the amplitudes and the centroid frequencies measured from the core sample are noticeably different from those of the coarse sand samples. First of all, despite that the amplitudes and the centroid frequencies both decrease and then rebound, like what was observed during the coarse sand experiments, the range of the variations are much smaller. Second, whereas the amplitudes measured from the coarse sand samples rebound very slowly after having reached the minima, the amplitudes measured from the core sample first rebound rapidly within an additional 2 °C of temperature drop. After exhibiting a small "bump" (a slight increase followed by a small decrease), the amplitudes continue to slowly increase with decreasing temperatures. These differences could be attributable to

the differences in the pore-scale structures, which are closely related to particle shapes and size distributions.

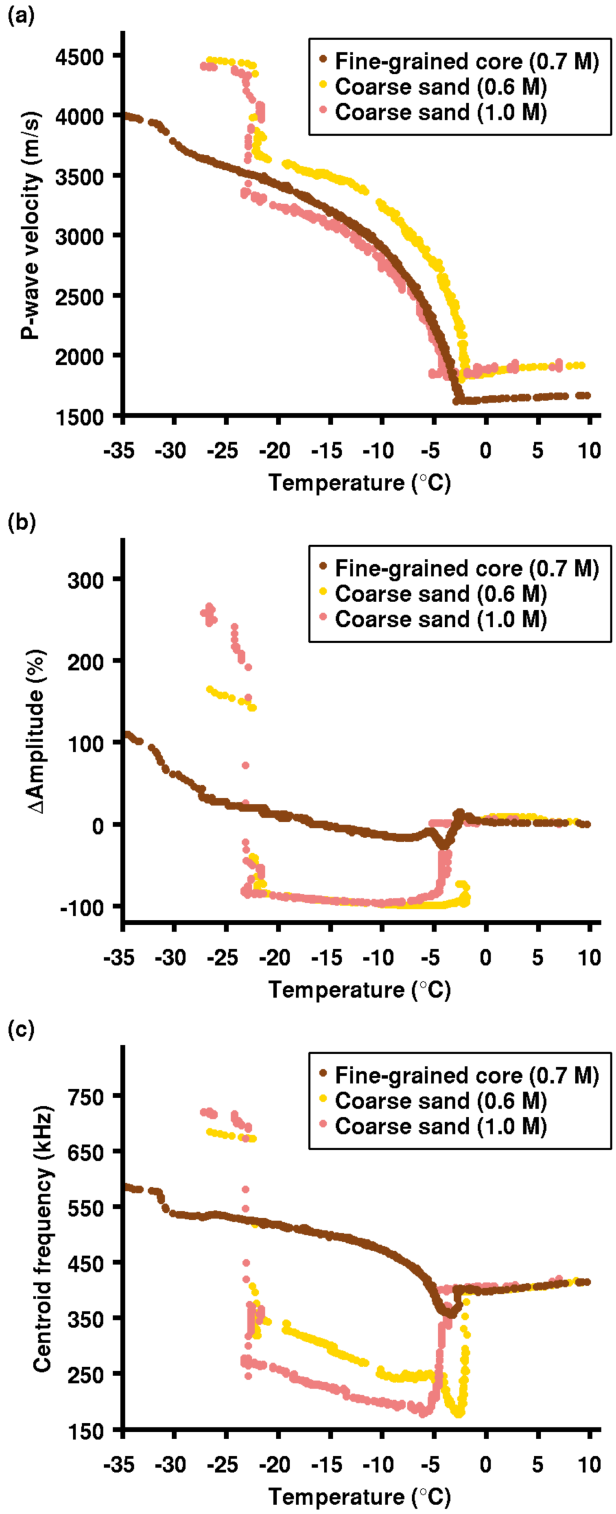

Figure 4.5 Comparisons of temperature-dependent variations of P-wave properties

obtained from the freezing measurements of the fine-grained saline permafrost core sample against those of coarse-grained Ottawa sand with neighboring pore-water salinity. (a) P-wave velocity, (b) relative peak-to-peak amplitudes (relative to peak-to-peak amplitudes observed at 10°C), and (c) centroid frequencies.

On freeze-thaw measurements

Another area for comparison is the difference in trajectory between the freeze and thaw cycles. In figure 4.6 we compare the velocity data obtained from the freeze-thaw measurements of the fine-grained saline core and the coarse sand samples (initial pore-water salinity = 2.5 M). In the temperature range from the freezing point to the eutectic point, we only see subtle freeze-thaw hystereses in both data sets. For the coarse sand sample, the low degree of hysteresis is within our expectation, since surface effects should be negligible in coarse-grained sediments. For the fine-grained saline core sample, the weak hysteresis has an important implication: Consistent with what we have expected of the fine-grained core sample (as mentioned at the beginning of this subsection), the influences of the surface effects appear to be negligible in the presence of dissolved salts.

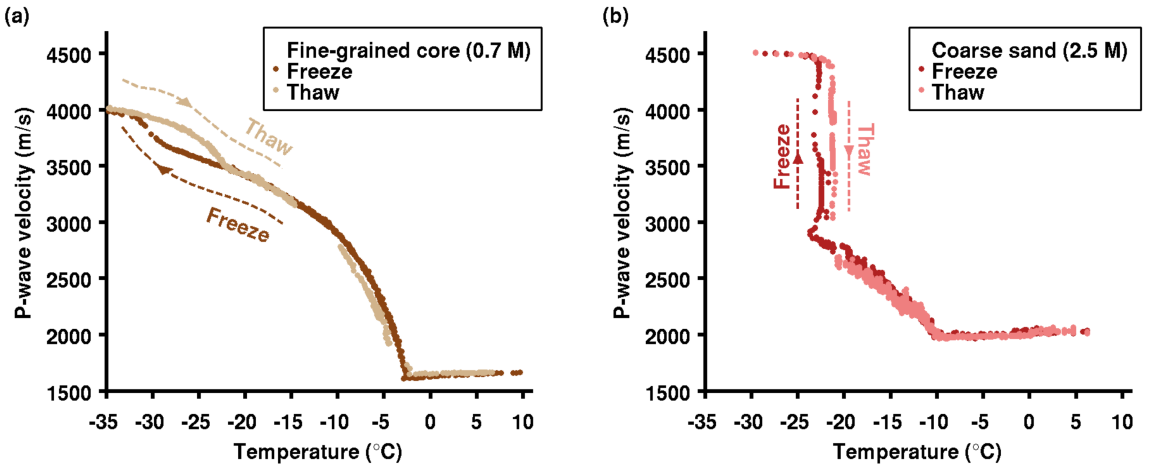

Figure 4.6 Comparisons of temperature-dependent variations of P-wave velocities between the freeze-thaw measurements of (a) the fine-grained saline permafrost core sample and (b) a brine-saturated coarse sand sample (20–30 Ottawa sand; initial pore-water salinity = 2.5 M).

At sub-eutectic temperatures, however, the velocity data of the core sample exhibit a considerable freeze-thaw hysteresis (between −31.8 °C and −21.3 °C). By contrast, only a small hysteresis can be seen in the data from the coarse sand sample (between −22.8 °C and −21.3 °C). In addition, whereas the coarse sand data show steep, stepwise changes along both the freezing and the thawing directions of the hysteresis, the data of the core sample show gradual, rampwise changes that are characteristic of the surface effects of the fine-grained particles. In short, at sub-eutectic temperatures, as the dissolved salts rapidly precipitate out of the residual pore water, we hypothesize that the influence of the surface effects become predominant in the fine-grained saline permafrost core sample.

4.4 Discussion

After having examined the influences of temperatures and salinities, we now consider the relationship between P-wave properties and ice content. As mentioned earlier, although the ice content variations are the inherent causes of the observed changes in the P-wave properties, what the data directly reveal are the apparent relationships tied to salinities and temperatures. To effectively analyze seismic properties in this context, a mapping is required to estimate ice content from initial pore-water salinities and temperature.

For the water-to-ice phase transitions occurring in the saline pore water, the phase diagram of aqueous NaCl solution is a necessary tool for estimating the ice content. However, this approach is based upon two assumptions: (1) Surface effects of the porous media are largely negligible, and (2) heterogeneous distributions of dissolved salts, though likely to be present during freezing/thawing of porous media, only have negligible effects on the ice content. In this regard, our saline coarse sand samples provide suitable bases for estimating ice content with the phase diagrams, considering that surface effects in these samples are negligible and the uniform grain/pore sizes are less likely to yield strong salt heterogeneities. Even though these sand samples are simplified representations of the natural saline permafrost, they provide a good entry point for gaining a better understanding of the rock physics relationship between the ice content and the P-wave properties.

4.4.1 Ice content estimation using phase diagrams

We use the phase diagram expressions in Potter et al. (1978) to estimate ice content from initial salinities and temperatures (Figure 4.7); a more detailed description of the procedure is presented in Appendix B2. These expressions allow us to calculate both the freezing point for a given initial salinity as well as estimate the ice content for the temperature range from the freezing point to the eutectic point.

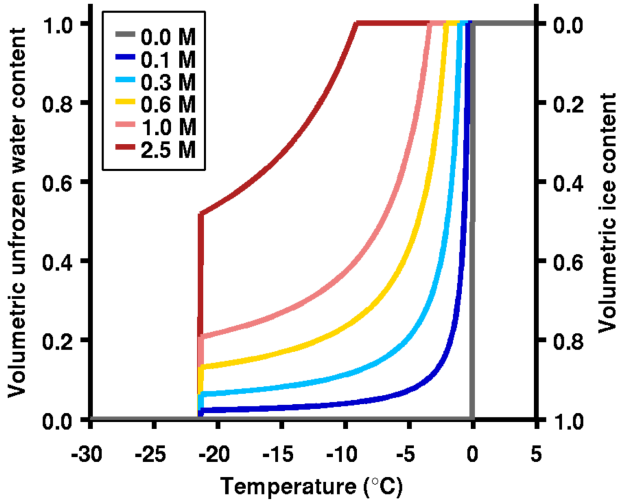

Figure 4.7 Volume fractions of unfrozen water and ice content (volumetric ice content = 1 – volumetric water content) estimated based upon the phase diagram expressions of aqueous NaCl solution in Potter et al. (1978) (Appendix B2).

Similar expressions have been utilized in prior studies providing some evidence of applicability in porous media. The study by Hivon and Sego (1995) provides successful precedents of using the phase diagram of NaCl solutions to estimate the unfrozen water content of saline frozen soils. In their study, the estimated values of the unfrozen water content of three different brine-saturated (initial pore-water salinities = 0.5 wt%, 1 wt%, and 3 wt%), partially frozen soil samples (sand, D_{50} ~ 400 μm; silty sand, D_{50} ~ 200 μm; fine silty sand, D_{50} ~ 80 μm) were compared against the measured values obtained using the time-domain reflectometry (TDR) method. For all the samples they tested, the two sets of the unfrozen-water-content values compare well with each other, suggesting that the phase diagram expressions are applicable to estimating water/ice content of saline frozen sediments.

4.4.2 Ice-content dependencies of P-wave properties

The measured P-wave properties, after being displayed as functions of ice saturation, collapse into tight trends regardless of the initial pore-water salinities as is shown in Figure 4.8. The velocity trends are particularly compact (Figure 4.8a), illustrating that the changing ice content is the controlling mechanism in the observed velocity variations. The attenuation trends (consisting of the peak-to-peak amplitude and the centroid frequency data) show slightly larger sample-to-sample differences (Figure 4.8b and 4.8c), possibly because attenuation is more sensitive to microstructure variability between the different samples.

Ice-content dependencies of P-wave velocity

P-wave velocities increase monotonically and steadily with increasing ice saturations (Figure 4.8a). Although such positive correlation between the velocities and the ice saturations are expected, the data trend is informative rather than trivial, because its shape can give us insight into the growth habits and pore-scale distributions of ice.

Ice-content dependencies of P-wave velocity can take on distinctly different shapes depending upon whether or not the initial growths of ice have preferential affinities to the sediment grains. The curves shown in Figure 4.8a correspond to several commonly-used models that depict end-member scenarios of the pore-scale distributions of ice (Dvorkin et al. 1999, Dvorkin and Nur 1996, Dvorkin et al. 1994, Helgerud 2001) base on contact cement theory. If ice growth begins on the grain surfaces, localized to contacts or coating grains, it can effectively act as a stiffening cement even at small ice contents; the resulting relationship between velocity and ice saturation will exhibit a steep increase at low ice saturations, as shown by curves 1 and 2 in Figure 4.8a.

Alternatively, if ice begins to grow at some distance away from the grain surfaces, a "pore filling" distribution, it may yield a smaller impact on frame stiffness. Such pore-filling ice can only lead to slight increases in the elastic moduli of the frozen sediments primarily by increasing the moduli of the pore fluids, hence yielding a gradual increase in the velocities as shown by curve 3 in Figure 4.8a.

However, as shown in Figure 8a, neither cementation nor pore-filling model for the pore-scale distributions of ice can explain the shape of our data trend, suggesting that the ice-nucleation sites may have no particular affinity or aversion to the grain surfaces. The ice-content dependencies of the velocities, which fall in between the predictions of the cementation and pore-filing models, have important implications for rock physics modeling: That is, the pore-scale distributions of ice may be partly cementing and partly

pore-filling. Hence, we may need to take into account an intermediate class of ice distributions when constructing rock physics models for saturated, unconsolidated saline permafrost.

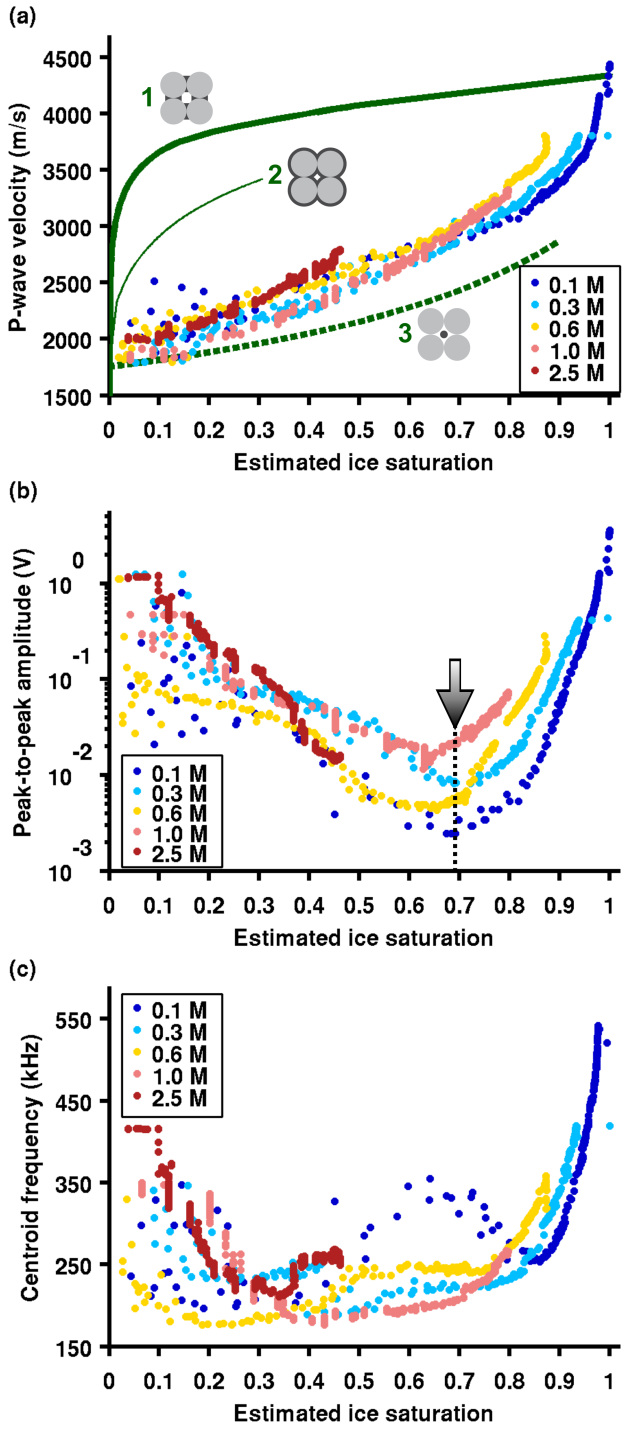

Figure 4.8 P-wave properties of brine-saturated coarse sand presented as functions of the estimated ice saturation. (a) P-wave velocity, (b) peak-to-peak amplitudes, and (c) centroid frequencies. The green curves in (a) correspond to model-predicted P-wave

velocities for three end-member rock physics models: 1, the stiffest cementation model, in which ice occurs and cements at grain contacts; 2, the second stiffest cementation model, in which ice coats and cements grains; 3, the softest pore-filling model, in which ice floats in pore space.

Ice-content dependencies of P-wave attenuation

In contrast to the monotonic increase in the velocities, P-wave attenuation first increases and then decreases with increasing ice saturations, which results in a trough distribution as can be seen in panel b and c of Figure 4.8. As mentioned previously, the increase in the attenuation is unexpected, given that attenuation typically trends lower in materials with higher velocities. A striking feature of the attenuation curves are the presence of an absorption peak at an ice saturation of ~70% (as shown by the converging minima of the amplitudes in Figure 4.8b). This particular level of ice saturation could be related to a characteristic scale within the samples. Several hypothesis exist to explain the attenuation observations but at this point they should be viewed as speculative and include,

1) Wave-induced phase transition: In a partially frozen medium, ice and water coexist in a delicate equilibrium. This metastable state could easily be disturbed by a small amount of wave energy passing through the medium, causing the proportion of ice and water to oscillate around the equilibrium value. Such phase fluctuations could absorb energy from the wave, yielding intrinsic attenuation. In this case, the characteristic length scale may be related to the wave period that is on the order of or shorter than the relaxation time of the phase fluctuations (Povey 1997, Spetzler and Anderson 1968b), which could be potentially controlled by either diffusion times or crystallization kinetics.
2) Wave-induced fluid flow: When solid and liquid phases coexist in a medium, a passing wave can create pressure gradients, causing the liquid to move relative to the solid. Internal frictions created by this relative motion can lead to intrinsic attenuation of the wave energy. In this case, the characteristic length scale should be comparable to the spatial scale of the pressure gradient (e.g., the wavelength-scale Biot attenuation, the pore-scale "squirt" attenuation, and the intermediate, mesoscopic-flow-induced attenuation) (Müller et al. 2010).
3) Elastic scattering: A partially frozen medium is highly heterogeneous. When the scale of the heterogeneities are comparable to the wavelength, elastic energy can be strongly scattered and redistributed into directions that are away from the direct propagation path between the source and the receiver, resulting in apparent attenuation of the wave energy. In this case, the characteristic scale should be related to the size of the scatterers.

For the attenuation observed in our partially frozen samples, the factors listed above may all have made some contributions. However, since it is difficult to examine the effects of each of these factors separately, the search for the predominant attenuation mechanism is a nontrivial task that is an area of active research (e.g., Carcione et al. 2007, Matsushima et al. 2011a). An in-depth discussion on this topic, however, is beyond the scope of this study.

Although much is yet to be learnt before we can fully understand the ice-content dependencies of the attenuation, high P-wave attenuation values seem to be an excellent diagnostic indicator of partially frozen saline permafrost.

4.5 Conclusion

To summarize, through our laboratory ultrasonic measurements, we have produced a rich data set for exploring how P-wave properties vary with respect to temperatures and salinities in saturated, unconsolidated saline permafrost. Moreover, this data set also enabled us to investigate the ice-content dependencies of the P-wave properties that lie in the heart of the rock physics relationships.

The temperature- and salinity-dependent variations of P-wave properties manifest marked velocity reductions in the presence of dissolved salts, and complex variations resulting from the water-to-ice phase transitions. Given the pervasive presence of saline permafrost in subsea and coastal areas of the Arctic, this improved understanding of seismic response should prove useful in subsurface mapping of such zones as well as monitoring destabilization of permafrost in warming environments.

The ice-content dependencies of P-wave properties show that whereas the velocities increase monotonically with increasing ice saturations, the attenuation is the highest in the partially frozen state. The velocity data, which cannot explained by either a purely cementing or a pore-filling model of ice distribution, indicate that the initial growths of ice may have no particular affinity or aversion to grain surfaces. The unexpected presence of strong attenuation, though yet to be fully understood, opens the possibility of incorporating seismic attenuation as a diagnostic tool for detecting and delineating saline permafrost. To move forward, it is crucial to develop rock physics models that will allow us to quantitatively estimate the ice content from the seismic measurables, given the central role of ice content both in mapping present-day distributions and in predicting future responses of saline permafrost.

5. An effective-medium model for P-wave velocities of saturated, unconsolidated saline permafrost

Submitted as: Dou, S., S. Nakagawa, D. Dreger, and J. Ajo-Franklin, An effective-medium model for P-wave velocities of saturated, unconsolidated saline: Geophysics (*submitted*).

5.1 Introduction

Saline permafrost contains soluble salts that often came from seawater. It is widespread in subsea and coastal areas of the Arctic and Antarctica (Brouchkov 2002, 2003, Hivon and Sego 1993, Ingeman-Nielsen et al. 2008, Osterkamp 1989). Characterized by its unusual mechanical, seismic and thermal properties, saline permafrost is increasingly important to the changing Arctic landscape. Unlike its non-saline counterpart, which is generally stable unless its temperature approaches 0°C, saline permafrost is highly responsive to warming even at temperatures well below 0°C (e.g., Ruffell et al. 1990). Such heightened temperature sensitivity is attributed to two profound effects: (1) dissolved salts lower the freezing point of the pore water; (2) they slow down the freezing process due to the desalting effect of ice (as crystal lattices of ice cannot incorporate salts) that rejects salt into the residual pore water, hence inhibiting further freezing. As a result, usually saline permafrost is partially frozen, a naturally "slushy" material with ice and brine coexisting in a delicate phase equilibrium that is easily perturbed.

Given this temperature sensitivity, saline permafrost is likely to thaw at an accelerated pace in a warming climate. Because dissolved salts render saline permafrost hypersensitive to temperature change, knowledge about the pore-water salinities is essential for predicting the likely responses of saline permafrost under climatic warming scenarios (e.g., Daanen et al. 2011).

Moreover, saline permafrost often is a source of geotechnical hazard, because the lower ice content in saline permafrost renders it mechanically weaker and easier to deform, given that ice is a key strengthening constituent of permafrost. Consequently, infrastructure built on saline permafrost is prone to damage because of the deformation-susceptible foundation strata (Brouchkov 2003, Hivon and Sego 1993, e.g., Ogata et al. 1983). As an example, Nixon (1988) mentions that foundation-bearing capacities are reduced by factors of 2–3 if the pore-water salinity of saline permafrost exceeds 10–20 ppt. Hence, the ability to detect and characterize saline permafrost is a key prerequisite for assessing the feasibility and design requirements for construction.

Geophysical methods are effective in inferring water/ice content in permafrost because of the marked differences in geophysical properties of ice and water (e.g., De Pascale et al. 2008, Hauck et al. 2011). Saline permafrost, given its low ice content, can be identified as a geophysical anomaly that stands out against a background of non-saline

permafrost (e.g., Collett and Bird 1988, 1993, Dou and Ajo-Franklin 2014, Hubbard et al. 2013, Schmitt et al. 2005).

Among the common geophysical parameters that are used in permafrost investigations, seismic velocities are the most relevant to engineering practice, given that the strength of geomaterials is often correlated with seismic velocities (Schön 2011). Prior studies demonstrate that increases in ice content generally map into increases in mechanical strength as well as seismic velocities (e.g., Nakano and Froula 1973, Timur 1968, Zimmerman and King 1986).

As the ice content is a key parameter for estimating present-day strength of saline permafrost as well as its future risk of thaw settlement, we also want to infer ice content from seismic velocities (e.g., Nelson et al. 2001, Nelson et al. 2002). However, quantitatively relating seismic velocities to ice content has proved challenging because microstructural distribution of pore ice often plays a determining role. As an example, if ice acts as a cement that bonds sediment grains together, a small amount of ice can effectively strengthen the frozen sediments, hence resulting in marked increases in seismic velocities. By contrast, if ice is suspended in the pore space without contacting sediment grains, it does not contribute to the overall stiffness of the frozen sediments, and increased ice content will only yield moderate increases in seismic velocities. Unfortunately the microstructural distribution of ice is rarely known for a given site. Alternatively, rock-physics-based calibrations are often necessary, for which reliable rock physics models must be built based upon high-quality datasets.

In this study, we developed an effective-medium model based upon ultrasonic P-wave data that were obtained from our previous laboratory study (Dou et al., submitted to Geophysics, 2015). The model uses a two-end-member mixing approach in which an ice-filled, fully frozen end-member and a water-filled, unfrozen end-member are mixed together to form the effective medium of the partially frozen sediments. This approach does not require parameter tuning of the mixing proportions, and unlike many existing models that assume a single characteristic pore-scale ice distribution (e.g., cementing ice, pore-filling ice, or load-bearing ice), it inherently assumes the coexistence of more than one type of pore-scale distributions of ice. The model is able to produce good data fits to the laboratory measurements, and yet the modeling workflow is simple and largely autonomous, which makes it potentially useful in field applications.

5.2 Brief overview of the laboratory measurements

The rock physics model presented in this paper is derived and tested based upon our laboratory ultrasonic data (detailed in Dou et al., submitted to Geophysics, 2015). To provide readers with necessary information about these data, we begin with a brief overview of the corresponding laboratory study.

5.2.1 Experiment objectives and materials

To gain a deeper understanding about how seismic properties of saline permafrost vary with respect to temperatures and pore-water salinities, Dou et al. (submitted to Geophysics, 2015) conducted ultrasonic P-wave measurements for saturated, unconsolidated sediment samples over broad ranges of salinities (0.0–2.5 M (0.0–130 ppt)) and temperatures (10°C to −30°C). Two types of samples were used in the experiment: six coarse-grained Ottawa sand samples saturated with distilled water or

brine of different concentrations, and a fine-grained saline permafrost core sample at its in situ salinity (extracted from the Barrow Peninsula on the Alaskan Arctic Coastal Plain) (Table 5.1). Measurements obtained from the coarse sand samples mainly reflect the influences of pore-water salinities, whereas measurements obtained from the fine-grained core sample are affected both by salinity and surface effects (i.e., unfrozen water retention that is chiefly caused by capillary effects of small pores and adsorption effects of clay minerals).

Table 5.1 Summary of the experiment materials.

Sample type	Coarse-grained Ottawa sand	Fine-grained saline permafrost core
D_{50} (μm)	720	53
Texture classification	Coarse sand	Silty-clayey sand
Texture profile	Sand (100 vol%)	Sand (52 vol%) Silt (30 vol%) Clay (18 vol%)
Mineral composition	Quartz (100 vol%)	Quartz (68 vol%) Plagioclase (11 vol%) Clay minerals[a] (18 vol%) Secondary minerals[b] (3 vol%)
Initial porosity	36 vol%	50 vol%
Initial pore-water salinity	(1) 0.0 M (2) 0.1 M (= 0.6 wt%) (3) 0.3 M (= 1.7 wt%) (4) 0.6 M (= 3.5 wt%) (5) 1.0 M (= 5.5 wt%) (6) 2.5 M (= 13.0 wt%)	0.7 M (= 4.2 wt %)

[a]Include (mainly) kaolinite and chloride.
[b]Include (mainly) dolomite, muscovite, and halite.

5.2.2 Key experiment observations

Here we summarize the key experiment observations that are shown in Figure 5.1:

- The influences of water-to-ice phase transitions: Regardless of salinity and sediment texture, the onset of freezing is accompanied by rapid increases of P-wave velocities and sharp declines of P-wave amplitudes.
- The influences of pore-water salinity: For the non-saline sample, the freezing-induced velocity increases and amplitude decreases occurred close to 0°C, and then both the velocities and the amplitudes quickly plateaued as the temperatures decreased further. In contrast, for the saline samples, the higher the initial (i.e., prior to freezing) pore-water salinity, the lower the freezing point. Between the freezing point and the eutectic point, P-wave velocities of the saline samples are markedly lower than the non-saline sample, manifesting the potent stiffness reduction effect of the dissolved salts; the P-wave amplitudes remain low over the course of the partially frozen stage.
- The influence of fine-grained particles: Surface effects related to fine-grained particles usually manifest themselves through a freezing-point depression effect.

When the pore-water is saline, however, this freezing-point depression effect is largely negligible at the freezing point but pronounced at the eutectic point (e.g., the onset of the sub-eutectic freezing only become identifiable at −31.8°C).

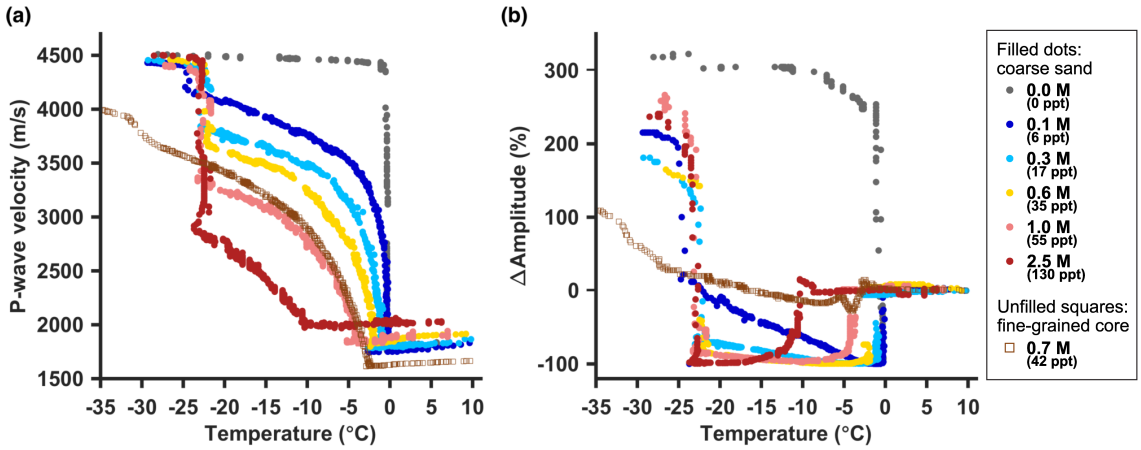

Figure 5.1 An abridged summary of the ultrasonic P-wave data acquired from a series of freezing experiments that are presented in Dou et al. (submitted to Geophysics, 2015): (a) P-wave velocities, and (b) relative peak-to-peak amplitudes (relative to the peak-to-peak amplitudes observed at 10°C).

5.3 Effective-medium modeling of P-wave velocities

Based upon the laboratory data described above, we developed a rock physics model to predict P-wave velocities of saturated, unconsolidated saline permafrost. The model's core relationship is between P-wave velocities and ice content. The experimental data, however, are velocities measured at various temperatures for different initial pore-water salinities. To facilitate a direct comparison between the data and the model predictions, we present the modeling results initially in terms of temperature and pore-water salinity.

Saturated saline permafrost is a mixture of sediment grains, ice, and water. Such a mixture, owing to the distinct elastic properties of its constituents, is heterogeneous and discontinuous on a small scale (i.e., grain/pore scale). Seismic measurements, however, are sensitive to the effective properties on a larger scale; that is, the average properties of a wavelength-scale volume (Guéguen and Palciauskas 1994). Therefore, for our rock physics modeling, we use an effective-medium approach to combine constituent properties into the effective properties of the composite, which can be viewed as a process of replacing the real heterogeneous medium by an effective homogeneous one.

We organize this section according to the three types of information required for the effective-medium modeling: (1) the elastic properties of the constituent phases, (2) the volume fractions of the phases (with an emphasis on the ice content estimation), and (3) the geometric details depicting the arrangements of the constituents. Property measurements exist for parameters involved in elastic properties and volume fractions, but little is known about the geometric arrangements. Thus we must apply assumptions. In our model, we adopt a two-end-member mixing approach to arrange the constituents,

and we assume a pore-scale distribution of ice in which cementing/load-bearing ice and pore-filling ice coexist. The details of the model are explained below.

5.3.1 Elastic properties of the constituents

- Ice: The elastic moduli of ice (K_i and G_i) are derived from the P- and S-wave velocities of pure ice (v_{Pi} and v_{Si}) measured by Vogt et al. (2008) ($K_i = v_{Pi}^2 \rho_i - 4/3 G_i$ and $G_i = v_{Si}^2 \rho_i$, where ρ_i is density of ice) (Equation C1-1 in Appendix C1). The density of ice ρ_i is determined based upon the expression in Pounder (1965) (Equation C1-2 in Appendix C1). These parameters are temperature-dependent (i.e., $K_i(T)$, $G_i(T)$, and $\rho_i(T)$, with T = temperature), and ice is assumed to be isotropic and homogeneous.
- Water (saline or non-saline): The Batzle-Wang relations (Batzle and Wang 1992) are used to derive the bulk modulus (K_w) and density of the pore water (ρ_w). Both parameters are temperature- and salinity-dependent (i.e., $K_w(T, S_n)$ and $\rho_w(T, S_n)$, where T = temperature and S_n = pore-water salinity).
- Sediment grains: The coarse-grained Ottawa sand is composed almost entirely of pure quartz (Table 5.1). Hence, we use the elastic properties of quartz as those of the individual sand grains. The fine-grained saline permafrost core sample consists of several different minerals (Table 5.1). Such a multi-mineralic mixture is treated as an assembly of composite grains. For each composite grain, its elastic moduli are the Hashin-Shtrikman-Hill average of moduli of the constituent minerals (Hashin and Shtrikman 1963, Hill 1952) (see Table C1.1 in Appendix C1), and its density is the arithmetic average of the mineral densities.

5.3.2 Volume fractions of the constituents

- The volume fractions of sediment grains (f_{gf}): $f_{gf} = 1 - \phi_{gf}$, where ϕ_{gf} is the porosity of the sediment grain frame (see Table 5.1). f_{gf} is assumed to be constant throughout the freezing/thawing processes.
- The volume fractions of pore ice and pore water: In fully saturated permafrost, water and ice occupy all available porosity. Hence, the total volume fraction of the pore water and pore ice equals to the porosity of the grain frame (ϕ_{gf}) and is also assumed to be constant. The volume ratio between pore water and pore ice, however, varies markedly with temperature, and the characteristics of the variations are determined by pore-water salinities and surface effects (i.e., supercooling of pore water caused by capillary and adsorption effects). As described earlier, our laboratory observations indicate that surface effects appear to be nearly negligible at above-eutectic temperatures. For this reason, we assume that at above-eutectic temperatures the ice content can be determined entirely based upon the phase diagram expressions of an aqueous NaCl solution. Only at sub-eutectic temperatures, when dissolved salts precipitate out of the residual pore water, do the influences of surface effects become strong. Thus at sub-eutectic temperatures, we assume that the ice content variations are controlled by surface

effects (Figure 5.2). The associated equations can be found in Appendix C2.

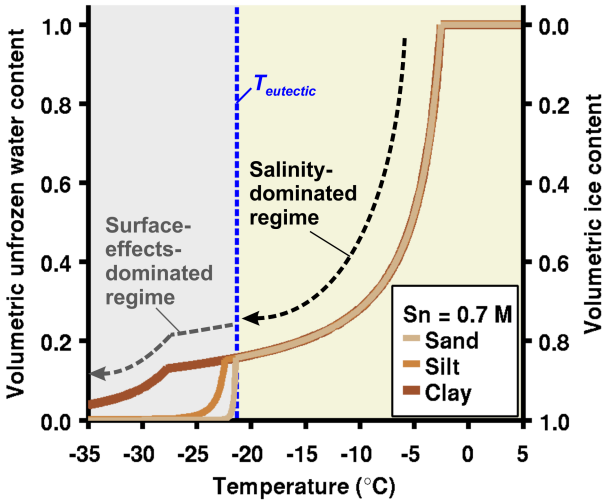

Figure 5.2 Volume fraction estimations of the unfrozen water content and the ice content, where volumetric ice content = 1 – volumetric water content (relevant equations are listed in Appendix C2). For the salinity-dominated regime, the ice/water content is estimated based upon the phase diagram expressions of aqueous NaCl solution in Potter et al. (1978). For the surface-effects-dominated regime, the ice/water content estimate is based upon the empirical expressions in Anderson et al. (1973).

5.3.3 Arrangements of the constituents: two-end-member mixing

The rationale for the mixing approach

A broad range of effective-medium models has been proposed to synthesize seismic velocities of permafrost (for a review, see Carcione and Seriani (1998)). Additionally, models that were originally developed for hydrate-bearing sediments also apply to ice-bearing permafrost, and vice versa. As with models that are used to understand ordinary sediments, two major types of effective-medium models can characterize permafrost: "inclusion models," which approximate permafrost as an effective host matrix enclosing inclusions (e.g., Jakobsen et al. 2000, Zimmerman and King 1986), and "granular pack models," which treats permafrost as a pack of sediment grains with ice distributed within the pore spaces (Ecker et al. 2000, Helgerud 2001, e.g., Helgerud et al. 1999).

The majority of these existing models, despite the different arrangements of the constituents, can be categorized as end-member models that depict the extreme ends of effective stiffness and seismic velocities. The key factor here is the assumed pore-scale distributions of ice. For instance, in the inclusion models proposed by Jakobsen et al. (2000), if ice forms part of the effective host matrix, the corresponding model is the stiff end-member in which ice is interconnected and bonds the sediments. If ice is treated as inclusions, the resulting model is the soft end-member in which ice is disconnected and thus is unable to bond the sediments. Similarly, for the granular pack models, if ice acts as a cement that hold the grains together, the corresponding model is the stiff end-

member that yields relatively high seismic velocities. If ice floats in the pore space without making contacts with the surrounding grains, the corresponding model is the soft end-member that yields relatively low seismic velocities.

Each of these end-member models assumes the sole existence of one possible physical scenario of pore-scale distributions of ice. But our experimental data indicate that various types of ice distributions may coexist in saturated, unconsolidated saline permafrost. The proof lies in the considerable mismatch between the experimental data and the predictions obtained from these end-member models (Figure 5.3). Hence, an appropriate mixing approach is desirable.

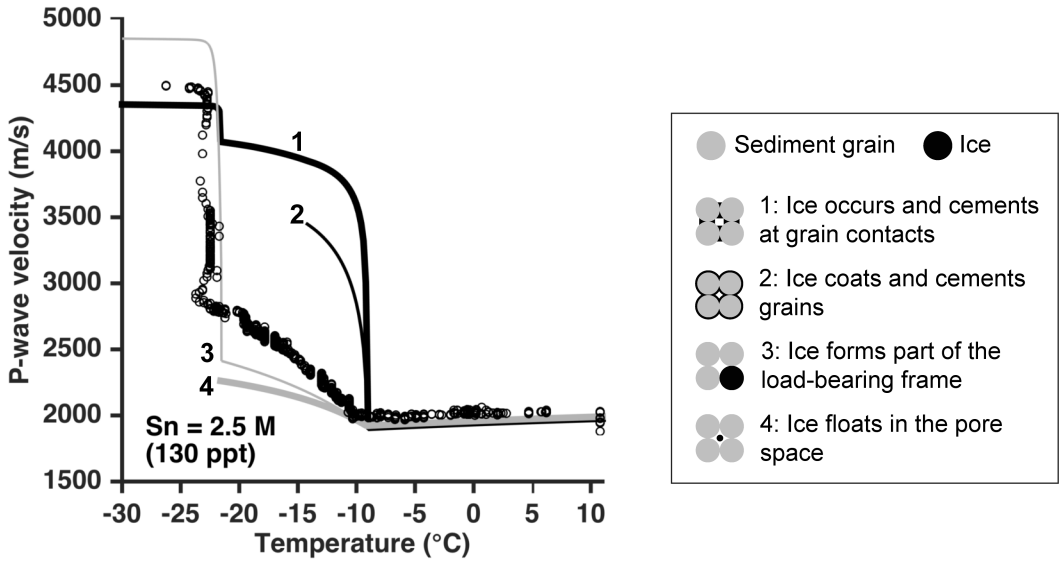

Figure 5.3 Comparisons between the observed (unfilled dots) and the model-predicted P-wave velocity (grey and black solid lines). Model predictions are based upon four commonly used end-member models (labeled with 1, 2, 3, and 4) that belong to the "granular pack" type.

Mixing schemes

After determining the necessity of incorporating a mixed ice distribution, we devised an appropriate mixing scheme. We first looked for plausible solutions in previous studies, and found two models that include end-member mixing procedures: (1) the variable cementation model in Chand et al. (2006), and (2) the two-end-member mixing model in Minshull et al. (1994).

We found the variable cementation model less appealing because it relies heavily on ad hoc tunings of the cement-ice/inclusion-ice ratio. Based upon the end-member inclusion models proposed by Jakobsen et al. (2000), the variable cementation model specifies part of the pore ice as interconnected cement, and the rest of the pore ice as disconnected inclusions. The relative proportion between the cement ice and the inclusion ice is a free parameter that needs to be tuned so as to achieve best data fits; hence the name "variable cementation" (Minshull and Chand 2009).

We favor the two-end-member mixing approach proposed by Minshull et al. (1994), as it does not require free-parameter tuning. In this model, the ice-filled (fully frozen) sediment represents the stiff end-member, and the water-filled (fully unfrozen)

sediment represents the soft end-member. These two end-members are mixed to model the intermediate, partially frozen sediment, and the mixing proportions are set to be equal to the relative proportions of pore ice and pore water. In this way, instead of relying on parameter tuning, the mixing proportion is consistent over the full range of the possible ice saturations. However, the mixing scheme of Minshull et al. (1994) cannot apply to unconsolidated sediments because Wyllie's time average equation is used to model the velocities of the fully frozen end-member, the fully unfrozen end-member, and the partially frozen mixture (Dvorkin and Nur 1998). Modifications are necessary to make this method useful for unconsolidated sediments.

To construct a modified two-end-member mixing model, we replace the Wyllie's time average equation used in Minshull et al. (1994) with effective-medium modeling procedures that are suitable for unconsolidated sediments. Figure 5.4 shows the framework of our two-end-member mixing model. We describe key steps in the model below. (See Appendix C3 for the associated equations and a comprehensive workflow diagram.)

- The fully frozen, stiff end-member. The fully frozen end-member is treated as a binary mixture of sediment grains and ice. Being ice-bonded and frozen solid, this stiff end-member is approximated as a composite of spherical sediment grains and ice-filled penny cracks. The elastic moduli of this sediment-ice composite are estimated with self-consistent approximation (Berryman 1995). Note that this step contains the only free parameter of the entire modeling procedure: the aspect ratio of the penny-shaped cracks. However, within a reasonable range, the model is relatively insensitive to this choice since both the ice and the grains are stiff components.
- The fully unfrozen, soft end-member. We approximate this binary mixture of sediment grains and water (saline or non-saline) as a random dense pack of sediment grains saturated with water. We first estimate the elastic moduli of the dry granular pack with Hertz-Mindlin contact theory (Mindlin 1949). Then we include the effects of pore water by using Biot's fluid substitution equations for the high-frequency limiting velocities (Johnson and Plona 1982).
- The intermediate, partially frozen state. We model this ternary mixture of sediment grains, ice, and water by mixing the fully frozen and the fully unfrozen end-members described above. As in Minshull et al. (1994), we use the relative volume fractions of pore ice and pore water as the relative volume fractions of the fully frozen and fully unfrozen end-members in the mixture. Instead of using the time average equation, we use the Hashin-Shtrikman-Hill (HSH) average of the two end-members to estimate effective moduli of the mixture.

To obtain an intuitive understanding of the microstructure implied by the two-end-member mixing model, we make use of the physical interpretation of the Hashin-Strikman bounds in the context of our modeling procedure (Figure 5.4): The upper bound is realized when the stiff end-member envelopes the soft end-member, in which case the ice-saturated, stiff end-member is largely interconnected and thus the pore ice mostly acts as a load-bearing/cementing material; the lower bound is realized when the soft end-member surrounds the stiff end-member, in which case the ice-saturated, stiff end-member is largely disconnected and thus the pore ice mostly acts as a non-loading-bearing/non-cementing material. By taking the Hill average of the Hashin-Shtrikman

bounds, the coexistence of load-bearing/cement ice and non-load-bearing/non-cement ice is taken into account. Although this interpretation provides an intuitive understanding of the two-end-member mixing model, it should not be considered as the realistic texture of unconsolidated saline permafrost.

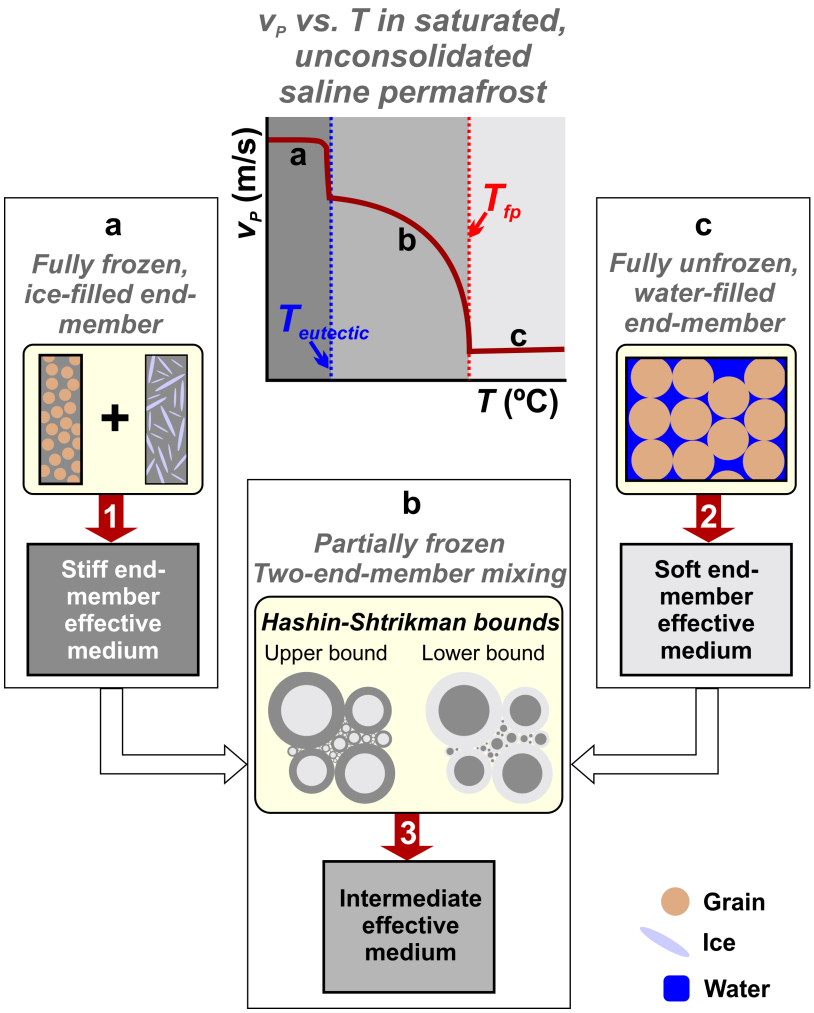

Figure 5.4 Schematic framework of the two-end-member mixing model. T = temperature; V_P = P-wave velocity; T_{fp} = the freezing point; $T_{eutectic}$ = the eutectic point. a—the fully frozen state associated with sub-eutectic temperatures; b—the partially frozen state associated with the temperatures between the freezing point and the eutectic point; c—the unfrozen state associated with the above-freezing temperatures. 1 = self-consistent approximation; 2 = Hertz-Mindlin contact theory followed by Biot's fluid substitution; 3 = Hashin-Shtrikman-Hill average. For the Hashin-Shtrikman upper bound, the stiff end-member envelopes the soft end-member; for the Hashin-Shtrikman lower bound, the soft end-member envelopes the stiff end-member.

5.4 Results

Due to the wide temperature and salinity ranges (−30°C to 10°C; 0.0–2.5 M) that were covered in our previous laboratory study, the resulting P-wave velocity data

incorporate all three states of the saturated, unconsolidated saline permafrost and thus is beneficial for evaluating the performance of our proposed mixing model.

Between the three states of the saline permafrost that were measured in the experiment, the partially frozen state is the most challenging to effectively model due to the presence of co-existing ice and brine. When applying the two-end-member mixing method to the experiment data, however, accurate modeling of the end-member states (i.e., the fully frozen state and the fully unfrozen state) is a prerequisite for modeling the intermediate, partially frozen state. In particular, to calibrate the only free parameter of the model—the aspect ratio of the ice-filled, penny-shaped cracks in the fully frozen end-member, the availability of the sub-eutectic measurements is especially helpful.

Nevertheless, the sub-eutectic measurements obtained from the corase-grained Ottawa sand samples correspond to the fully frozen end-member, similar measurements obtained from the fine-grained saline permafrost core sample are still affected by residual unfrozen water due to the surface effects of the fine-grained sediments. As a result, for the velocity modeling of the corase-grained sand samples, it is straightforward to calibrate the aspect ratio of the ice-filled cracks. For the velocity modeling of the fine-grained saline permafrost core sample however, the direct calibration of the crack aspect ratio is infeasible. Hence, we present these modeling results in different ways. For the corase-grained sand samples, we present the results associated with a fixed crack aspect ratio, and for the fine-grained saline permafrost core sample, we present a sensitivity test that is devised to explore the optimal range of the crack aspect ratio.

5.4.1 Modeling results: saturated, coarse-grained Ottawa sand samples

Figure 5.5 provides a comparison between our proposed mixing model and the observed P-wave velocities for all six coarse sand samples used in the prior experiment. Compared with the models depicted in Figure 5.3, the improvements in fit are clear. At all the above-freezing and sub-eutectic temperatures, the models for the fully unfrozen end-member and the fully frozen end-member (with an aspect ratio of 0.02 for the ice-filled, penny-shaped cracks) provide an excellent match. At temperatures that are immediately below the freezing point, the model-predicted velocities are also in good agreement with the data. At temperatures that are significantly below the freezing point, the model fits appear to vary with pore-water salinities in which the model predicts the velocities quite well for samples with medium (0.6 M) and high (1.0 M and 2.5 M) pore-water salinities (Figure 5.5d, 5.5e, and 5.5f), where the mismatch remains lower than 9% of the observed velocities. The model overestimates the velocities by up to 5%−15% of the observed values for samples with low (0.1 M and 0.3 M) pore-water salinities (Figure 5.5b and 5.5c). The causes of such salinity dependence are unclear but could be due to a microstructural preference in ice distribution during the final phases of freezing, a process not currently included in the model.

Despite the imperfect match between the predicted and the observed P-wave velocities is imperfect, the two-end-member mixing model has predictive ability that is sufficient to ensure its usefulness, and its data fits are much improved compared with existing models that are shown in Figure 5.3. Such improvements are attributable to the two-end-member mixing approach that inherently assumes the coexistence of more than one type of pore-scale distributions of ice.

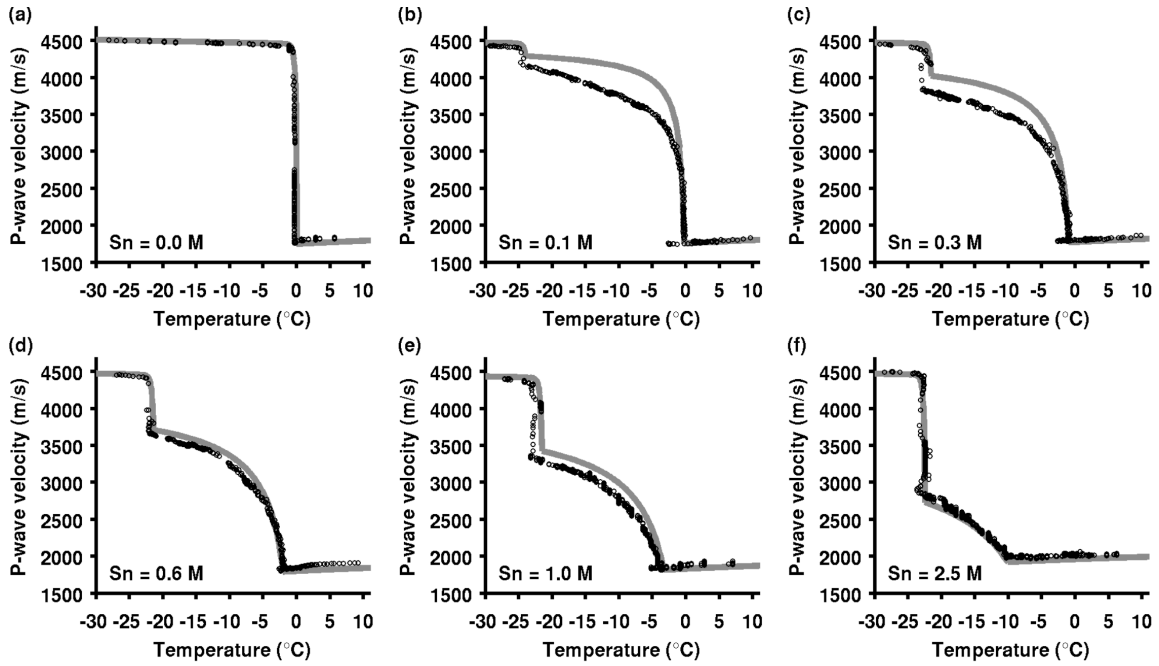

Figure 5.5 Comparisons between model-predicted (gray solid lines) and observed P-wave velocities (unfilled dots) as a function of temperatures and salinities for saturated, coarse-grained Ottawa sand.

5.4.2 Modeling results: saturated, fine-grained saline permafrost core sample

In contrast with the coarse-grained Ottawa sand packs, the fine-grained saline-permafrost core sample is an example of a more complicated coastal sediment class in which clay minerals and/or clay-sized particles (diameter $\leq$ 2 μm) are often present. For effective-medium modeling, the presence of clays introduces three challenges. First, surface effects strongly influence ice/water variations and are usually predicted using empirical relations with significant uncertainties. Second, because of significant water retention of the clay minerals/particles, sediments containing clays may not be fully frozen even at temperatures as low as −80°C (Thimus et al. 1993), and consequently the parameter calibration for the fully frozen end-member can be problematic. Third, the elastic properties of clay minerals are not well constrained and differ significantly in prior studies (e.g., Mondol et al. 2008), which in turn introduces additional uncertainties in the modeling results. Despite the presence of these uncertainties, the modeling results are not always sensitive to selection of the described parameters, particularly for our core sample in which the volume fraction of clay minerals is only 18%. To explore the influences of these parameter uncertainties, we present the modeling results of the fine-grained core sample in the form of a sensitivity test.

Among the different parameters mentioned above, inaccuracy in surface-effects-controlled unfrozen water content is likely the least important. This is because surface effects only become predominant for the core sample under sub-eutectic temperatures. Hence, these uncertainties have little influence for the temperature range between the freezing point and the eutectic point, which is the more likely range of temperature variation encountered in natural permafrost systems.

For completeness, we conduct modeling for the entire temperature range (10°C to −35°C) that was used in our experiment. For sub-eutectic temperatures, we use the unfrozen water content predictions associated with the measured D_{50} value of the sample (53 μm) (Appendix C2). Owing to uncertainties in the surface-controlled water content and in the D_{50} value measured with the laser diffraction particle-size analyzer, the sub-eutectic model predictions deviate substantially from the data (Figure 5.6). In the rest of this section, we focus on the temperature range between the freezing point and the eutectic point (i.e., from −2.5°C to −21.3°C), for which we examine the effects of the other two types of uncertainties, namely those of the elastic properties of clay minerals, and the aspect ratio of the ice-filled cracks.

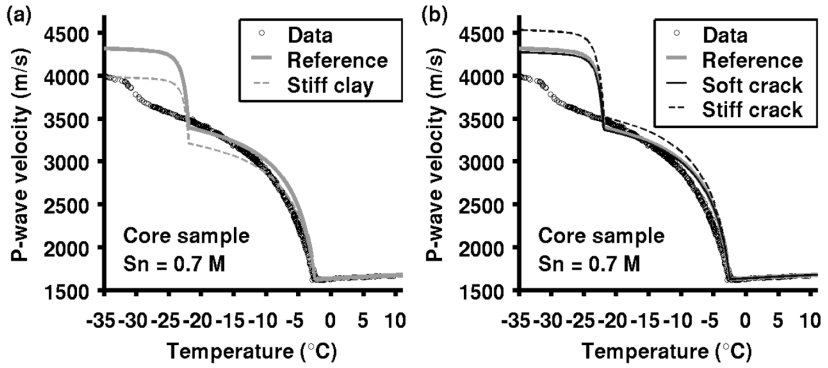

Figure 5.6 Results of the sensitivity tests for the fine-grained saline permafrost core sample. (a) Tests on the influences of clay properties: "soft clay" (reference model) versus "stiff clay". (b) Tests on the aspect ratio of the ice-filled penny cracks: "soft crack" versus "stiff crack". The unfilled dots denote the observed P-wave velocities, and the gray and black lines (solid and sashed) denote the model-predicted P-wave velocities.

We first set up a reference model by searching for a combination of the clay properties and the aspect ratio value that yields satisfactory agreement between the model predictions and the data. After a series of tests, we use the elastic properties of the "soft clay" (Table 5.2) and an aspect ratio of 0.02 for the reference model. Next, we conduct two sets of sensitivity tests as follows:

- Soft clay versus stiff clay (Figure 5.6a): To investigate the impact of uncertainties related to the elastic properties of clay minerals, we replace the "soft clay" in the reference model by the "stiff clay" in Table 5.2. Because the elastic moduli of "soft clay" and "stiff clay" correspond to the lowest and highest values found in existing literature (Mondol et al. 2008, Wang et al. 2001), the differences in the associated modeling results represent the range of the uncertainties related to clay properties. The test results show that the overall differences between using "soft clay" and using "stiff clay" are quite small (with root-mean-square-deviation of 116 m/s and 149 m/s, respectively), which indicates that the modeling results are insensitive uncertainties in clay properties.
- Soft cracks versus stiff cracks (Figure 5.6b): To investigate the impact of uncertainties related to the aspect ratio of the ice-filled cracks (in the fully frozen end-member), we change the aspect ratio of 0.02 in the reference value into 0.004 and 0.1 to represent "soft crack" and "stiff crack", respectively. The test results show that the use of "soft crack" yields little difference when compared against

the reference model. The use of parameters equivalent to a "stiff crack", on the other hand, results in model predictions that are notably different from those of the reference model. These results suggest that a small aspect ratio (e.g., < 0.1) may be more sensible for the modeling. However, the overall differences remain small, with root-mean-square-deviation no greater than 184 m/s, indicating that the modeling results are robust as long as the aspect ratio values are kept reasonably low.

Table 5.2 Elastic properties of clay minerals used for modeling the saline core sample.

	Mineral type	***K*** **(GPa)**	***G*** **(GPa)**	ρ **(kg/m^3)**	**References**
Soft clay	Kaolinite	1.5	1.4	1618.7	Woeber et al. (1963)
Stiff clay	Kaolinite	55.0	31.8	4890.4	Katahara (1996)

To conclude, the two-end-member mixing model remains effective for the fine-grained saline permafrost core sample that contains clays. However, we must point out that the influences of clays appear negligible here because the core sample does not contain a particularly high clay content (18 vol%). For clay-rich sediments, the uncertainties related to clays may become more important to represent.

5.5 Discussion

Our analyses so far are based upon P-wave velocities that are presented as functions of temperatures and salinities. Such a presentation is consistent with the laboratory measurements, thereby allowing the data and the model predictions to be directly compared. At this point we are still one step away from examining how P-wave velocities are related to ice content, a relationship that lies at the center of the rock physics modeling.

In this section, we move forward by presenting both the data and modeling results as functions of ice saturations, a unitless quantity, defined as the pore volume fraction of given sediment occupied by ice. With this alternative presentation, we also revisit the likely pore-scale distribution of ice, which is a key factor that determines the predictive capability of the effective-medium models. We infer the ice distributions using both the characteristics of the velocity versus ice saturation data trends, and by how well an effective model assuming a particular ice distribution can predict the velocity data.

Naturally, any reliable inference regarding the ice distributions depends on the accuracy of both the data and the participating components of the effective-medium modeling. To ensure accuracy, we use the data and the modeling results obtained from the coarse-grained Ottawa sand samples, given that they are free of uncertainties related to clay minerals and/or clay-sized particles. Moreover, this dataset provides comprehensive sampling of P-wave properties over the entire span of the probable ice saturations (0–1.0), which makes it an ideal testing ground for various effective-medium models. Our discussion focuses on the P-wave velocities (Figure 5.7a), and the corresponding P-wave amplitude data and the characteristics of P-wave attenuation (Figure 5.7b), with the objective of presenting very intriguing observations that we hope can inspire future research in this area. Quantitative modeling of the attenuation, however, is beyond the scope of this study.

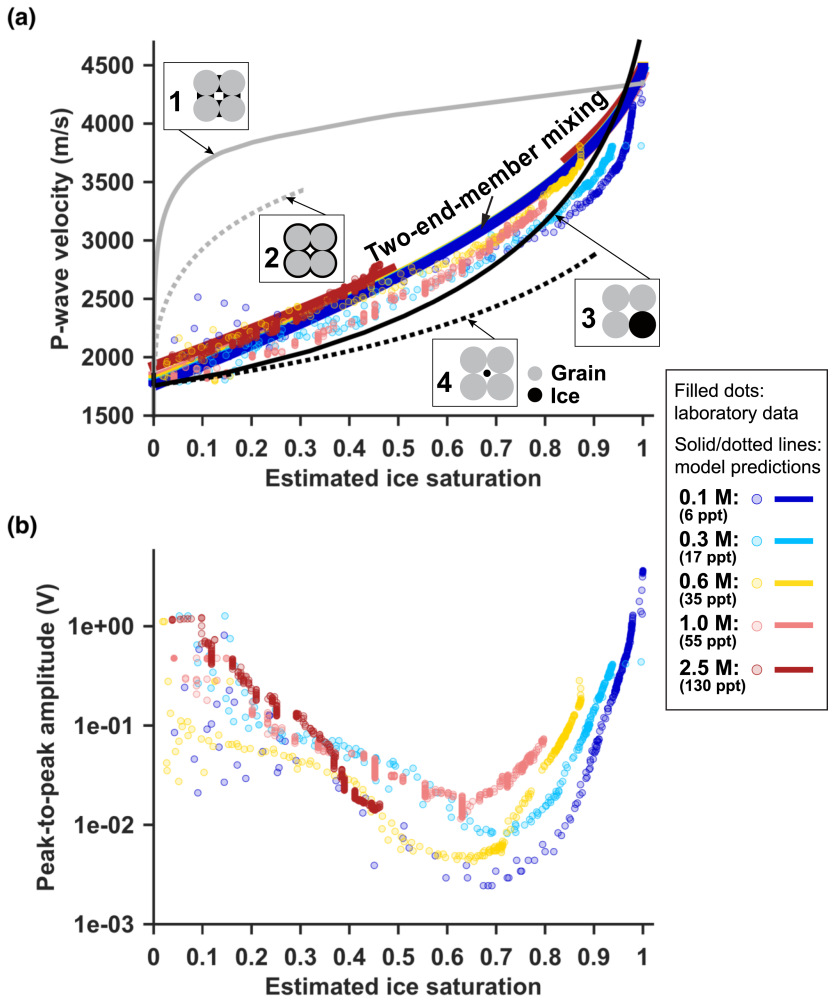

Figure 5.7 P-wave properties of brine-saturated coarse sand presented as functions of the estimated ice saturation. (a) Comparisons between the observed (filled dots) and the model-predicted P-wave velocity (solid lines) of brine-saturated, coarse-grained sand presented as functions of the estimated ice saturation. The black and gray lines correspond to microstructure-based end-member models: 1—ice occurs and cements at grain contacts; 2—ice coats and cements grains; 3—ice forms part of the load-bearing frame; 4—ice floats in pore space. The colored lines correspond to the two-end-member mixing model. (b) peak-to-peak amplitudes.

5.5.1 Ice-content dependencies of P-wave velocity

Comparison 1: data versus end-member model predictions

The shape of the ice-content-dependent variations of P-wave velocity can provide some insights concerning the pore-scale distribution of ice. For instance, the end-member model predictions shown in Figure 5.7a can be divided into the two categories of cementation models and non-cementation models. For cementation models 1 and 2, ice starts growing along the surfaces of the sediment grains and act as contact cement to bond the grains together. In this case, a small amount of cementating ice effectively

stiffens the frozen sediments. As a result, when ice saturations are low, the model-predicted P-wave velocities exhibit rapid increase as ice saturation increases. For the non-cementation models 3 and 4, ice acts as part of the load-bearing solid frame or as part of the pore fluids. For both of these models, the volume fraction of ice needs to be large to substantially affect the effective properties of the frozen sediments. As a result, when ice saturations are low, the model-predicted P-wave velocities exhibit slow increase as ice saturation increases.

However as Figure 5.7a shows the experimental measurements are in between these end member scenarios. For a broad range of ice saturations (from 0 to ~0.85), the measured P-wave velocity shows a steady increase with increasing ice saturations, indicating that neither cementating ice nor pore-filling ice are dominant at the pore-scale.

Comparison 2: data versus two-end-member mixing model predictions

On the other hand, the two-end-member mixing model discussed previously predicts P-wave velocities that agree well with the data (Figure 5.7a). The good performance of the model is attributable to the mixing scheme that naturally considers the coexistence of cementing ice and non-cementing ice.

The fits at low ice saturations (0–0.2) are particularly interesting. They indicate that even in the early stage of freezing, the pore ice may already be partially cementing and partially non-cementing. Considering that the initial growth of cementing ice likely occurs at grain surfaces where defects promote crystal nucleation, the likely presence of non-cementing ice implies that the growth of ice crystals may have no preferential affiliation to the grain surfaces. This contradicts the commonly used conceptual model in which ice is thought to be growing from the grain surfaces in uniform coarse-grained sediments (i.e., as depicted by the "grain-coating" model in Figure 5.7a) (e.g., Arenson and Sego 2006, Hivon and Sego 1995).

The following behaviors of the velocity data remain unexplained by the two-end-member mixing model:

- Over the entire range of the ice saturations (0.0–1.0), the data show noticeable inter-sample differences, but the model predictions are more compact. At a given ice saturation, the model-predicted P-wave velocities increase systematically as the initial pore-water salinity increases, which is a direct result of the salinity dependency of P-wave velocities. The data do not show such a systematic trend. The effective-medium models assume that the samples are effectively homogeneous at length scales comparable to the signal wavelengths. The more scattered and less systematic appearance of the data indicates that effective medium is a good but not a perfect approximation of the partially frozen samples.
- At moderate to high ice saturations (0.2–0.9), the two-end-member mixing model tends to slightly overestimate the P-wave velocities for the majority of the saline samples that are examined here (except for the most saline sample with an initial salinity = 2.5 M, for which the model predictions match the data closely), and such overestimation becomes more obvious when ice saturations are greater than 0.8. This mismatch indicates that the amount of cementing ice is likely to be biased high in the two-end-member mixing model.
- At high ice saturations (0.9–1.0), the data show a steepening increase of velocity as the samples approach full ice saturation, whereas the corresponding increase in the model-predicted velocities remains steady over the entire range of the ice

saturations. Such behavior of the data indicates that as the samples approach full ice saturation, the last bit of newly formed ice mainly acts as cement. This ice-type shift is not considered in the two-end-member model, leading to the mismatch.

Comparison 3: load-bearing end-member model versus two-end-member mixing model

Although three out of four of the end-member models shown in Figure 5.7a are unable to produce good data fits, the load-bearing model (model No. 3 in Figure 5.7a) is an exception. Originally proposed by Helgerud et al. (1999), the load-bearing model is frequently used in gas hydrate research (e.g., Dai et al. 2004, Helgerud et al. 2000, Winters et al. 2004), but is rarely mentioned in the permafrost literature. At low ice saturations (0–0.2), the load-bearing model underestimates the velocities, which could result from the complete absence of cementation ice in the assumed ice distributions. The two-end-member mixing model yields better data fits, which is intuitively reasonable given that the model assumes coexisting cementation and non-cementation ice. At moderate to high ice saturations (0.2–0.8), neither the load-bearing model nor the two-end-member mixing model produce ideal data fits. Instead, the model predictions appear to form a tight envelope that wraps around the data, with the upper envelope corresponding to the two-end-member mixing model and the lower envelope corresponding to the load-bearing model. We speculate that the realistic pore-scale distribution of ice is likely to be intermediate to the scenarios depicted in these two models. At high ice saturations (0.8–1.0), the observations exhibit a steepening increase of velocity as the samples approach 100% ice saturation, but neither model is able to accurately capture this feature. The velocity increase predicted by the two-end-member mixing model remains steady at high ice saturations. The load-bearing model predictions show a more noticeable steepening trend, but the onset and the extent of the steepening do not agree well with the data. The key observations is that when the samples approach full ice saturation, further increases in ice content rapidly increase stiffness, a process that may require special treatment in the modeling procedure.

5.5.2 Ice-content dependencies of P-wave amplitudes

The behavior of the P-wave amplitudes (Figure 5.7b) is unexpected and intriguing. In many geomaterials, we ordinarily see velocity increase being accompanied by amplitude increase, as high velocity materials tend to be less attenuative. However, our amplitude data contradict this expectation. As the velocities monotonically increase with increasing ice saturations, the amplitudes first drop by two to three orders of magnitude, and then grow back as ice saturations increase further. As a result, the amplitude versus ice saturation trends look like a group of asymmetric troughs (Figure 5.7b). A striking feature is that these troughs all reach their bottoms at an ice saturation of ~70%, indicating the presence of an absorption peak in P-wave attenuation and the likely existence of a characteristic length scale.

Attenuation can be caused by both intrinsic (elastic energy converted to heat) and apparent (elastic energy scattered away from direct propagating paths) attenuation mechanisms. In the experimental data, intrinsic attenuation mechanisms can include wave-induced phase transition and wave-induced fluid flow.

For the case of wave-induced phase transition in a partially frozen medium, ice and water coexist in a delicate equilibrium that could easily be perturbed by a small

amount of seismic wave energy passing through the medium. Once off balance, the proportion of ice and water starts to oscillate around the equilibrium value in a process that could absorb energy from the waves. In this case, the characteristic scale would be related to the wave period that is on the order of or shorter than the relaxation time of the phase oscillations (Povey 1997, Spetzler and Anderson 1968b).

For wave-induced fluid flow in a partially frozen medium, solid and liquid phases coexist. As seismic waves pass through the medium, pressure gradients produced by the waves can cause the liquid to move relative to the solid, yielding internal frictions that consume the wave energy. In this case, the characteristic length scale should be comparable to the spatial scale of the pressure gradient (e.g., the wavelength-scale Biot attenuation, the pore-scale "squirt" attenuation, and the intermediate, mesoscopic-flow-induced attenuation) (Müller et al. 2010).

In addition, partially frozen ice is a highly heterogeneous medium, which can produce apparent attenuation by elastic scattering of primary seismic wave energy. If the scale of the heterogeneities is comparable to the wavelength, wave energy can be scattered away from the direct path between the transmitter and the receiver, resulting in reduced energy that can reach the receivers. In this case, the characteristic scale should be related to the size of the scatterers.

Despite the many unknowns regarding the causes of the attenuation, these observations demonstrate the great potential of using attenuation as a diagnostic tool to detect and delineate partially frozen permafrost.

5.6 Conclusion

Based upon laboratory ultrasonic data (detailed in Dou et al., submitted to Geophysics, 2015), we developed an effective-medium model for P-wave velocities of saturated, unconsolidated saline permafrost. The modeling procedure considers three physical states of saline permafrost: the unfrozen state as a soft end member, the fully frozen state as a stiff end-member, and the partially frozen state as a mixture of the soft and stiff end-members. The benefit of the model is that the two-end-member mixing approach naturally assumes that cementation ice and non-cementation ice coexist in partially frozen saline permafrost, and that there is no free-parameter tuning involved in the mixing procedure. The modeling results agree well with the laboratory P-wave velocity data, demonstrating the utility of the model.

In contrast, models that assume ice either as grain-bonding cement or as pore-filling material are unable to produce comparably good fits to the data. The root cause of the mismatch is that these models assume only one type of pore-scale distribution of ice, whereas it is likely that a mixture of several types of ice distributions exist in saline permafrost.

One exception to this is the load-bearing model proposed by Helgerud et al. (1999), in which ice is assumed to be part of the load-bearing solid frame. Despite its tendency to underestimate the velocities due to the absence of cementing ice, it produces data fits that are comparable to those of our model at moderate to high ice saturations (0.2–1.0 for the Ottawa sand sample). At low ice saturations (0–0.2), however, our two-end-member mixing model produces better data fits because cementating ice is naturally included in the assumed ice distributions.

As with all effective-medium models, our model has a number of limitations. Despite the fit quality, it overestimates P-wave velocities at moderate to high ice saturations (e.g., 0.2–1.0), indicating that the model may have overestimate the role of cementing ice at those saturations. When samples approach full ice saturation, further increase in ice content appear to cause a steep increase in P-wave velocity, indicating the potent stiffening effect, however, are unable to capture this feature. Additional correction terms may be required in the effective-medium expressions so as to improve on these two aspects.

The good performance of the model in predicting ultrasonic P-wave velocities is an important prerequisite toward field-scale characterization of saturated, unconsolidated saline permafrost. Although bridging laboratory results and field applications requires additional research effort, especially because of the large difference in ultrasonic frequencies and field-seismic frequencies.

6. Conclusion and outlook

6.1 Conclusion

The body of work comprising this dissertation is the first systematic study to investigate seismic properties of unconsolidated saline permafrost. Starting out with site-specific endeavors focusing upon the Barrow Environmental Observatory (BEO) in Alaska, the study had grown to encompass field and laboratory components, yielding rich data sets, new knowledge, and versatile methods.

Through our field experiments, we realized that saline permafrost might exist in large volume along the polar coasts. In our laboratory experiments, we witnessed saline permafrost's striking vulnerability to temperature disturbances. Based upon these factors, we call attention to the potentially big impact of saline permafrost degradation in a warming climate.

6.1.1 Key results

- Field-scale studies (chapter 2 and 3): Based upon the dispersion characteristics of our multichannel surface-wave data, we detected pervasive presence of partially frozen/unfrozen saline permafrost across the BEO. S-wave velocity profiles produced from our full-wavefield inversion procedure revealed that the saline permafrost forms a markedly thick layer (at least ~8–39 m thick) that is overlain by thin layers (~1–6 m thick) of non-saline permafrost. Given that the permafrost structures at the BEO could be representative of a considerable portion of the permafrost along the polar coasts, saline permafrost is likely to be common in such areas.
- Lab-scale studies (chapter 4 and 5): From our ultrasonic P-wave measurements (velocity and attenuation) acquired during controlled freezing/thawing of saturated, unconsolidated saline sediments, we observed the striking sensitivity of P-wave properties to temperature changes, the potent velocity reduction caused by the dissolved salts, as well as the unexpected strong attenuation concurring with the onset of freezing. By examining the measured P-wave properties that are presented as functions of ice saturations, we learned that the initial growth of pore ice may have no preferences or aversion to the sediment-grain surfaces, and thus pore ice is neither purely cementing nor purely pore-filling. Based upon this microstructural realization, we developed a two-end-member mixing model for inferring ice saturations from P-wave velocities. The good data fits provided by the model illustrate its utility in seismic characterizations of saline permafrost.

6.1.2 Key contributions

- Rich datasets: Both the field and laboratory components of this dissertation have produced rich datasets that are among the first of their kind for investigating seismic properties of unconsolidated saline permafrost. These datasets will be made available to other researchers who are interested in this topic.
- Effective workflow for field-scale delineation of saline permafrost (or for seismic mapping of near-surface permafrost in general): We have devised a workflow in

which all components are proven effective in field applications, including data types (multichannel surface waves), processing methods (dispersion analyses via cylindrical slant stack), and inversion procedure (a full-wavefield approach that uses global optimization methods such as PSO to solve the nonlinear inverse problem). The utility of this workflow is not limited to saline permafrost, but expandable to near-surface permafrost in general.

- Improved microstructural realization regarding the pore-scale distribution of ice: We have learned from our laboratory data that the pore ice are more likely to be partially cementing and partially pore-filling in saturated, unconsolidated saline permafrost. This improved microstructural realization plays a crucial role in developing rock physics models of saline permafrost.

6.1.3 Applications outside permafrost research

The methods developed in this dissertation are also applicable to science and engineering areas that are outside permafrost research. Here we provide a few examples:

- Nondestructive testing of pavements: Pavements are inversely dispersive media that are present in our everyday life (a stiff asphalt layer overlies a soft sand-and-gravel base). Our field-seismic workflow should be readily adaptable for nondestructive testing of pavements. Such usage of surface-wave methods has been presented in existing literature (e.g., Ryden and Lowe 2004, Ryden and Park 2006).
- Rock physics modeling of hydrate-bearing sediments: As mentioned in chapter 4 and 5, because physical and mechanical properties of gas hydrates approximate those of pure ice, rock physics models developed for hydrate-bearing sediments are also applicable to permafrost, and vice versa.

6.1.3 Limitations

- Field-seismic workflow:
  - Data acquisition: Acquiring seismic data for permafrost studies is labor-intensive and time-consuming, which limits the data coverage that is obtainable in a field campaign. The best time to conduct seismic surveys is in the winter when the ground is frozen solid. The hard ground facilitates geophone coupling, and makes it easier to mobilize heavy equipment during the survey. However, it also increases the efforts required in putting down and picking up geophones. In order to put geophone spikes in the ground, snow cover needs to be cleared, and drill holes (as inserting points for geophone spikes) need to be prepared. Although flat geophone bases (instead of spikes) are sometimes recommended for saving time and labor, the resulting geophone coupling usually is poor and the data quality often is inferior.
  - Computational costs: Computing the full wavefield is time-consuming but necessary in surface-wave inversion of irregularly dispersive media. So far we have not found faster alternatives.
- The lab-field divide: Quantitatively linking laboratory and field investigations is not yet within our reach for the reasons listed below.
  - Composition differences: In laboratory experiments, we often use simpler sediment samples that are tailored for specific investigations (e.g., the coarse-grained Ottawa sand used in our laboratory studies). Although simpler

samples are helpful in providing us fundamental knowledge about the rock physics relationship (e.g., the plausible pore-scale distributions of ice), the associated quantitative results must go through site-specific adaptations when applied to field studies.

- Scale differences: The wavelengths relevant to our laboratory data are on the order of millimeter to centimeters, whereas the wavelengths of our field data are on the order of meters and tens of meters. Such scale differences can be particularly crucial for seismic attenuation that is often scale-dependent. As a result, although our laboratory observations indicate that seismic attenuation can be an excellent indicator for the presence of partially-frozen saline permafrost, we need more studies to confirm its usefulness in field investigations.

6.2 Outlook

6.2.1 Remaining research questions

- Field-scale:
  - How to better constrain the bottom of the saline layer?
  - Can seismic attenuation be reliably retrieved in field-scale studies? Can attenuation be an effective indicator for the presence of saline permafrost?
  - Is saline permafrost indeed pervasive along the polar coasts? Can we conduct regional-scale mapping to confirm or deny this speculation?
- Lab-scale:
  - What are the dominant mechanisms causing the strong attenuation in partially frozen saline permafrost? Can we develop quantitative models to explain the attenuation?
  - How will grain sizes, clay content, and saturation conditions affect the temperature- and salinity-dependent variation of seismic properties?

6.2.2 Directions for future research

- Regional-scale mapping of saline permafrost using airborne electromagnetic (AEM) techniques: Despite the many merits of seismic methods for delineating saline permafrost at the scales of engineering interests, the data acquisition is too time-consuming and labor-intensive for conducting regional-scale mapping of near-surface permafrost. A better candidate for this task is the AEM technique, which enables fast and cost-effective acquisition of detailed conductivity data over a large area. A highly relevant example of such an application is reported by Mikucki et al. (2015), in which the researchers detected the presence of a deep briny groundwater system existing beneath an Antarctic dry valley.
- Climate modeling efforts taking into account the influence of saline permafrost: Given that saline permafrost is likely to be pervasive along the polar coasts, its strong sensitivity to temperature changes could intensify the positive feedback between climate change and permafrost degradation. It is therefore important for climate modeling efforts to take into account the influence of saline permafrost.

Bibliography

Akimov, A. T., 1973, Logging in shallow dry boreholes for studying geotechnical and geodynamic characteristics of frozen soils: Proceedings of International Conference on Permafrost, U.S.S.R. Contribution: U.S. National Academy of Sciences, 452–456.

Andersland, O. B., and B. Ladanyi, 2004, Frozen ground engineering. 2nd ed: Wiley; American Society of Civil Engineers.

Anderson, D. M., A. R. Tice, and H. L. McKim, 1973, The unfrozen water and the apparent specific heat capacity of frozen soils: Proceedings of the 2nd International Conference on Permafrost: National Academy of Sciences, 289−295.

Arenson, L. U., and D. C. Sego, 2006, The effect of salinity on the freezing of coarse-grained sands: Canadian Geotechnical Journal, **43**, no. 3, 325−337, doi: 10.1139/t06-006.

Baker, G. C., and T. E. Osterkamp, 1989, Salt redistribution during freezing of saline sand columns at constant rates: Water Resources Research, **25**, no. 8, 1825−1831, doi: 10.1029/WR025i008p01825.

Barnes, D. F., 1963, A review of geophysical methods for delineating permafrost: Proceedings of International Conference on Permafrost: National Academy of Sciences, 349–355.

Batzle, M., and Z. Wang, 1992, Seismic properties of pore fluids: Geophysics, **57**, no. 11, 1396−1408, doi: 10.1190/1.1443207.

Beaty, K. S., D. R. Schmitt, and M. Sacchi, 2002, Simulated annealing inversion of multimode Rayleigh wave dispersion curves for geological structure: Geophysical Journal International, **151**, no. 2, 622–631, doi: 10.1046/j.1365-246X.2002.01809.x.

Bergamo, P., C. Comina, S. Foti, and M. Maraschini, 2011, Seismic characterization of shallow bedrock sites with multimodal Monte Carlo inversion of surface wave data: Soil Dynamics and Earthquake Engineering, **31**, no. 3, 530–534, doi: 10.1016/j.soildyn.2010.10.006.

Berryman, J. G., 1981, Elastic wave propagation in fluid-saturated porous media: The Journal of the Acoustical Society of America, **69**, no. 2, 416−424, doi: 10.1121/1.385457.

Berryman, J. G., 1995, Mixture theories for rock properties, Rock Physics & Phase Relations: American Geophysical Union.

Bing, H., P. He, and Y. Zhang, 2015, Cyclic freeze–thaw as a mechanism for water and salt migration in soil: Environmental Earth Sciences, **74**, no. 1, 675-681, doi: 10.1007/s12665-015-4072-9.

Black, P. B., and A. R. Tice, 1989, Comparison of soil freezing curve and soil water curve data for Windsor sandy loam: Water Resources Research, **25**, no. 10, 2205−2210, doi: 10.1029/WR025i010p02205.

Black, R. F., 1964, Gubik formation of quaternary age in northern Alaska: exploration of naval petroleum reserve no. 4 and adjacent areas, Northern Alaska, 1944-53: U.S. Geological Survey professional paper, 59–91.

Boiero, D., E. Wiarda, and P. Vermeer, 2013, Surface- and guided-wave inversion for near-surface modeling in land and shallow marine seismic data: The Leading Edge, **32**, no. 6, 638–646, doi: 10.1190/tle32060638.1.

Brouchkov, A., 2002, Nature and distribution of frozen saline sediments on the Russian Arctic coast: Permafrost and Periglacial Processes, **13**, no. 2, 83−90, doi: 10.1002/ppp.411.

Brouchkov, A., 2003, Frozen saline soils of the Arctic coast: their distribution and engineering properties: Proceedings of the 8th International Conference on Permafrost: National Academy of Sciences, 95−100.

Brown, J. 1969, Ionic concentration gradient in permafrost, Barrow, Alaska. U. S. Army Cold Regions Research and Engineering Laboratory Research Report.

Brownlee, J., 2012, Swarm algorithms: Clever Algorithms: Nature-Inspired Programming Recipes (ebook), http://www.cleveralgorithms.com/nature-inspired/swarm/pso.html, accessed 1 Nov., 2014

Carcione, J. M., O. H. Campanella, and J. E. Santos, 2007, A poroelastic model for wave propagation in partially frozen orange juice: Journal of Food Engineering, **80**, no. 1, 11−17, doi: 10.1016/j.jfoodeng.2006.04.044.

Carcione, J. M., and G. Seriani, 1998, Seismic and ultrasonic velocities in permafrost: Geophysical Prospecting, **46**, no. 4, 441−454, doi: 10.1046/j.1365-2478.1998.1000333.x.

Carmichael, R. S., 1989, Practical Handbook of Physical Properties of Rocks & Minerals: CRC Press.

Chen, S., 2014, Another Particle Swarm Toolbox (in MATLAB), Version 20140330, http://www.mathworks.com/matlabcentral/fileexchange/25986-another-particle-swarm-toolbox, accessed 12 Nov., 2014.

Chervinskaya, O. P., A. D. Frolov, and Y. D. Zykov, 1998, On the correlation of elastic and strength properties for saline frozen soils: Proceedings of the 7th International Conference on Permafrost: National Academy of Sciences, 139−141.

Collett, T. S., and K. J. Bird, 1988, Freezing-point depression at the base of the ice-bearing permafrost on the North Slope of Alaska: Proceedings of the 5th International Conference on Permafrost: Tapir Publishers, 50−55.

Collett, T. S., and K. J. Bird, 1993, Unfrozen, high-salinity intervals within ice-bearing permafrost, North Slope of Alaska: Proceedings of the 6th International Conference on Permafrost: South China University of Technology Press, 94−99.

Collins, F. R., and M. C. Brewer, 1961, Core tests and test wells, Barrow area, Alaska : exploration of naval petroleum reserve no. 4 and adjacent areas, northern Alaska, 1944-53. Part 5, Subsurface geology and engineering data: U.S. Geological Survey professional paper, 569–644.

Cox, M., E. F. Scherrer, and R. Chen, 1999, Static corrections for seismic reflection surveys, Geophysical references series: Society of Exploration Geophysicists.

Daanen, R. P., T. Ingeman-Nielsen, S. S. Marchenko, V. E. Romanovsky, N. Foged, M. Stendel, J. H. Christensen, and K. Hornbech Svendsen, 2011, Permafrost degradation risk zone assessment using simulation models: The Cryosphere, **5**, no. 4, 1043−1056, doi: 10.5194/tc-5-1043-2011.

Dafflon, B., S. S. Hubbard, C. Ulrich, J. E. Peterson, Y. Wu, H. Wainwright, and T. Kneafsey, 2014, Estimating permafrost properties, including ice-content and

saline layer distributions, near Barrow (AK) using electrical conductivity imaging: Manuscript in preparation.
Dai, J., H. Xu, F. Snyder, and N. Dutta, 2004, Detection and estimation of gas hydrates using rock physics and seismic inversion: examples from the northern deepwater Gulf of Mexico: The Leading Edge, **23**, no. 1, 60−66, doi: 10.1190/1.1645456.
De Pascale, G. P., W. H. Pollard, and K. K. Williams, 2008, Geophysical mapping of ground ice using a combination of capacitive coupled resistivity and ground-penetrating radar, Northwest Territories, Canada: Journal of Geophysical Research: Earth Surface, **113**, no. F2, F02S90, doi: 10.1029/2006JF000585.
Desai, K. P., and E. J. Moore, 1967, Well log interpretation in permafrost: SPWLA 8th Annual Logging Symposium: Society of Petrophysicists and Well-Log Analysts.
Dou, S., and J. Ajo-Franklin, 2014, Full-wavefield inversion of surface waves for mapping embedded low-velocity zones in permafrost: Geophysics, **79**, no. 6, EN107−EN124, doi: 10.1190/geo2013-0427.1.
Douma, H., and M. Haney, 2013, Exploring nonlinearity and nonuniqueness in surface-wave inversion for near-surface velocity estimation: The Leading Edge, **32**, no. 6, 648–655, doi: 10.1190/tle32060648.1.
Dvorkin, J., J. Berryman, and A. Nur, 1999, Elastic moduli of cemented sphere packs: Mechanics of Materials, **31**, no. 7, 461−469, doi: 10.1016/S0167-6636(99)00009-5.
Dvorkin, J., and A. Nur, 1996, Elasticity of high-porosity sandstones: theory for two North Sea data sets: Geophysics, **61**, no. 5, 1363−1370, doi: 10.1190/1.1444059.
Dvorkin, J., and A. Nur, 1998, Time-average equation revisited: Geophysics, **63**, no. 2, 460−464, doi: 10.1190/1.1444347.
Dvorkin, J., A. Nur, and H. Yin, 1994, Effective properties of cemented granular materials: Mechanics of Materials, **18**, no. 4, 351−366, doi: 10.1016/0167-6636(94)90044-2.
Eberhart, R. C., and J. Kennedy, 1995, A new optimizer using particle swarm theory: Proceedings of the Sixth International Symposium on Micro Machine and Human Science.
Ecker, C., J. Dvorkin, and A. Nur, 2000, Estimating the amount of gas hydrate and free gas from marine seismic data: Geophysics, **65**, no. 2, 565−573, doi: 10.1190/1.1444752.
Forbriger, T., 2003a, Inversion of shallow-seismic wavefields: I. Wavefield transformation: Geophysical Journal International, **153**, no. 3, 719–734, doi: 10.1046/j.1365-246X.2003.01929.x.
Forbriger, T., 2003b, Inversion of shallow-seismic wavefields: II. Inferring subsurface properties from wavefield transforms: Geophysical Journal International, **153**, no. 3, 735–752, doi: 10.1046/j.1365-246X.2003.01985.x.
Gautier, D. L., K. J. Bird, R. R. Charpentier, A. Grantz, D. W. Houseknecht, T. R. Klett, T. E. Moore, J. K. Pitman, C. J. Schenk, J. H. Schuenemeyer, K. Sorensen, M. E. Tennyson, Z. C. Valin, and C. J. Wandrey, 2009, Assessment of undiscovered oil and gas in the Arctic: Science, **324**, no. 5931, 1175–1179, doi: 10.1126/science.1169467.
Gilichinsky, D., E. Rivkina, C. Bakermans, V. Shcherbakova, L. Petrovskaya, S. Ozerskaya, N. Ivanushkina, G. Kochkina, K. Laurinavichuis, S. Pecheritsina, R.

Fattakhova, and J. M. Tiedje, 2005, Biodiversity of cryopegs in permafrost: FEMS Microbiology Ecology, **53**, no. 1, 117–128, doi: 10.1016/j.femsec.2005.02.003.

Guéguen, Y., and V. Palciauskas, 1994, Introduction to the physics of rocks: Princeton University Press.

Hamilton, E. L., 1976, Attenuation of shear waves in marine sediments: The Journal of the Acoustical Society of America, **60**, no. 2, 334–338, doi: 10.1121/1.381111.

Harvey, D. J., 1981, Seismogram synthesis using normal mode superposition: the locked mode approximation: Geophysical Journal of the Royal Astronomical Society, **66**, no. 1, 37-69, doi: 10.1111/j.1365-246X.1981.tb05947.x.

Hashin, Z., and S. Shtrikman, 1963, A variational approach to the theory of the elastic behaviour of multiphase materials: Journal of the Mechanics and Physics of Solids, **11**, no. 2, 127−140, doi: 10.1016/0022-5096(63)90060-7.

Hauck, C., M. Böttcher, and H. Maurer, 2011, A new model for estimating subsurface ice content based on combined electrical and seismic data sets: The Cryosphere, **5**, no. 2, 453−468, doi: 10.5194/tc-5-453-2011.

Hauck, C., and C. Kneisel, 2008, Applied geophysics in periglacial environments: Cambridge University Press.

Hayashi, K., 2012, Analysis of surface-wave data including higher modes using the genetic algorithm, GeoCongress 2012: American Society of Civil Engineers, 2776–2785.

Helgerud, M. B., 2001, Wave speeds in gas hydrate and sediments containing gas hydrate: a laboratory and modeling study. dissertation, Stanford University.

Helgerud, M. B., J. Dvorkin, and A. Nur, 2000, Rock Physics Characterization for Gas Hydrate Reservoirs: Elastic Properties: Annals of the New York Academy of Sciences, **912**, no. 1, 116−125, doi: 10.1111/j.1749-6632.2000.tb06765.x.

Helgerud, M. B., J. Dvorkin, A. Nur, A. Sakai, and T. Collett, 1999, Elastic-wave velocity in marine sediments with gas hydrates: effective medium modeling: Geophysical Research Letters, **26**, no. 13, 2021−2024, doi: 10.1029/1999GL900421.

Herrmann, R. B., 2004, Computer programs in seismology, version 3.30, http://www.eas.slu.edu/eqc/eqccps.html accessed 15 Jan., 2012.

Hilbich, C., 2010, Time-lapse refraction seismic tomography for the detection of ground ice degradation: The Cryosphere, **4**, no. 3, 243−259, doi: 10.5194/tc-4-243-2010.

Hill, R., 1952, The elastic behaviour of a crystalline aggregate: Proceedings of the Physical Society, Section A, **65**, no. 5, 349.

Hinkel, K. M., and F. E. Nelson, 2003, Spatial and temporal patterns of active layer thickness at Circumpolar Active Layer Monitoring (CALM) sites in northern Alaska 1995–2000: Journal of Geophysical Research: Atmospheres, **108**, no. D2, 8168, doi: 10.1029/2001JD000927.

Hivon, E. G., and D. C. Sego, 1993, Distribution of saline permafrost in the Northwest Territories, Canada: Canadian Geotechnical Journal, **30**, no. 3, 506−514, doi: 10.1139/t93-043.

Hivon, E. G., and D. C. Sego, 1995, Strength of frozen saline soils: Canadian Geotechnical Journal, **32**, no. 2, 336−354, doi: 10.1139/t95-034.

Hoekstra, P., and D. McNeill, 1973, Electromagnetic probing of permafrost: Proceedings of the 2nd International Conference on Permafrost: National Academy of Sciences, 517–526.

Hubbard, S. S., C. Gangodagamage, B. Dafflon, H. Wainwright, J. Peterson, A. Gusmeroli, C. Ulrich, Y. Wu, C. Wilson, J. Rowland, C. Tweedie, and S. D. Wullschleger, 2012, Quantifying and relating land-surface and subsurface variability in permafrost environments using LiDAR and surface geophysical datasets: Hydrogeology Journal, **21**, no. 1, 149−169, doi: 10.1007/s10040-012-0939-y.

Hubbard, S. S., C. Gangodagamage, B. Dafflon, H. Wainwright, J. Peterson, A. Gusmeroli, C. Ulrich, Y. Wu, C. Wilson, J. Rowland, C. Tweedie, and S. D. Wullschleger, 2013, Quantifying and relating land-surface and subsurface variability in permafrost environments using LiDAR and surface geophysical datasets: Hydrogeology Journal, **21**, no. 1, 149−169, doi: 10.1007/s10040-012-0939-y.

Huyer, W., and A. Neumaier, 1999, Global optimization by multilevel coordinate search: Journal of Global Optimization, **14**, no. 4, 331–355, doi: 10.1023/A:1008382309369.

Ikeda, T., T. Matsuoka, T. Tsuji, and K. Hayashi, 2012, Multimode inversion with amplitude response of surface waves in the spatial autocorrelation method: Geophysical Journal International, **190**, no. 1, 541–552, doi: 10.1111/j.1365-246X.2012.05496.x.

Ingeman-Nielsen, T., N. N. Foged, and A. S. Jørgensen, 2008, Geophysical investigation of saline permafrost at Ilulissat, Greenland: Proceedings of the 9th International Conference on Permafrost: Institute of Northern Engineering, University of Alaska Fairbanks, 773−778.

Jakobsen, M., J. A. Hudson, T. A. Minshull, and S. C. Singh, 2000, Elastic properties of hydrate-bearing sediments using effective medium theory: Journal of Geophysical Research: Solid Earth, **105**, no. B1, 561−577, doi: 10.1029/1999JB900190.

Johnson, D. L., and T. J. Plona, 1982, Acoustic slow waves and the consolidation transition: The Journal of the Acoustical Society of America, **72**, no. 2, 556−565, doi: 10.1121/1.388036.

Jones, A., V. Stolbovoy, C. Tarnocai, G. Broll, O. Spaargaren, and L. Montanarella, 2009, Soil atlas of the northern circumpolar region. Edited by A. Jones, V. Stolbovoy, C. Tarnocai, G. Broll, O. Spaargaren and L. Montanarella: European Commission.

Jorgenson, M. T., K. Yoshikawa, M. Kanveskiy, Y. L. Shur, V. Romanovsky, S. Marchenko, G. Grosse, J. Brown, and B. Jones. 2008, Permafrost characteristics of Alaska. Fairbanks, Alaska: Institute of Northern Engineering, University of Alaska, Fairbanks.

Justice, J. H., and C. Zuba, 1986, Transition zone reflections and permafrost analysis: Geophysics, **51**, no. 5, 1075–1086, doi: 10.1190/1.1442163.

Kachitvichyanukul, V., 2012, On comparison of three evolutionary algorithms: GA, PSO and DE: Industrial Engineering and Management Systems, **11**, no. 3, 215−223.

Katahara, K. W., 1996, Clay mineral elastic properties, SEG Technical Program Expanded Abstracts, 1691−1694.

Ke, G., H. Dong, Z. Cao, and L. Liu, 2010, Surface wave dispersion curve calculation in TIV medium: SEG Technical Program Expanded Abstracts, 1924–1928, doi: 10.1190/1.3513219.

King, M. S., B. I. Pandit, J. A. Hunter, and M. Gajtani, 1982, Some seismic, electrical, and thermal properties of sub-seabottom permafrost from the Beaufort Sea: Proceedings of the 4th Canadian Permafrost Conference: National Research Council Canada, 268−273.

Kneisel, C., C. Hauck, R. Fortier, and B. Moorman, 2008, Advances in geophysical methods for permafrost investigations: Permafrost and Periglacial Processes, **19**, no. 2, 157−178, doi: 10.1002/Ppp.616.

Li, H., 2009, Experimental and numerical study of sonic wave propagation in freezing sand and silt. dissertation, University of Alaska Fairbanks.

Lu, L., and B. Zhang, 2006, Inversion of Rayleigh waves using a genetic algorithm in the presence of a low-velocity layer: Acoustical Physics, **52**, no. 6, 701–712, doi: 10.1134/S106377100606011x.

Lu, L. Y., C. H. Wang, and B. X. Zhang, 2007, Inversion of multimode Rayleigh waves in the presence of a low-velocity layer: numerical and laboratory study: Geophysical Journal International, **168**, no. 3, 1235–1246, doi: 10.1111/j.1365-246X.2006.03258.x.

Maraschini, M., F. Ernst, S. Foti, and L. V. Socco, 2010, A new misfit function for multimodal inversion of surface waves: Geophysics, **75**, no. 4, G31–G43, doi: 10.1190/1.3436539.

Maraschini, M., and S. Foti, 2010, A Monte Carlo multimodal inversion of surface waves: Geophysical Journal International, **182**, no. 3, 1557–1566, doi: 10.1111/j.1365-246X.2010.04703.x.

Matsushima, J., M. Suzuki, Y. Kato, T. Nibe, and S. Rokugawa, 2008, Laboratory experiments on compressional ultrasonic wave attenuation in partially frozen brines: Geophysics, **73**, no. 2, N9–N18, doi: 10.1190/1.2827214.

Matsushima, J., M. Suzuki, Y. Kato, and S. Rokugawa, 2011, Laboratory measurements of ultrasonic P-wave and S-wave attenuation in partially frozen unconsolidated sediments saturated with brine: SEG Technical Program Expanded Abstracts: 2130–2134.

Matsushima, J., M. Suzuki, Y. Kato, and S. Rokugawa, 2011a, Laboratory measurements of ultrasonic P-wave and S-wave attenuation in partially frozen unconsolidated sediments saturated with brine, SEG Technical Program Expanded Abstracts, 2130−2134.

Matsushima, J., M. Suzuki, Y. Kato, and S. Rokugawa, 2011b, Estimation of ultrasonic scattering attenuation in partially frozen brines using magnetic resonance images: Geophysics, **76**, no. 1, T13−T25, doi: 10.1190/1.3511355.

Mavko, G., T. Mukerji, and J. Dvorkin, 2009, Rock Physics Handbook: Tools for Seismic Analysis in Porous Media (Second Edition). Second ed: Cambridge University Press.

Meyer, H., L. Schirrmeister, A. Andreev, D. Wagner, H.-W. Hubberten, K. Yoshikawa, A. Bobrov, S. Wetterich, T. Opel, E. Kandiano, and J. Brown, 2010, Lateglacial and Holocene isotopic and environmental history of northern coastal Alaska –

Results from a buried ice-wedge system at Barrow: Quaternary Science Reviews, **29**, no. 27–28, 3720–3735, doi: 10.1016/j.quascirev.2010.08.005.

Mikucki, J. A., E. Auken, S. Tulaczyk, R. A. Virginia, C. Schamper, K. I. Sorensen, P. T. Doran, H. Dugan, and N. Foley, 2015, Deep groundwater and potential subsurface habitats beneath an Antarctic dry valley: Nat Commun, **6**, doi: 10.1038/ncomms7831.

Miller, R. D., J. A. Hunter, W. E. Doll, B. J. Carr, R. A. Burns, R. L. Good, D. R. Laflen, and M. Douma, 2000, Imaging permafrost with shallow P- and S-wave reflection: SEG Technical Program Expanded Abstracts: 1339–1342.

Mindlin, R. D., 1949, Compliance of elastic bodies in contact: Journal of Applied Mechanics, **16**, no. 3, 259−268.

Minshull, T. A., and S. Chand, 2009, The pore-scale distribution of sediment-hosted hydrates: evidence from effective medium modelling of laboratory and borehole seismic data: Geological Society, London, Special Publications, **319**, no. 1, 93−101, doi: 10.1144/sp319.8.

Minshull, T. A., S. C. Singh, and G. K. Westbrook, 1994, Seismic velocity structure at a gas hydrate reflector, offshore western Colombia, from full waveform inversion: Journal of Geophysical Research: Solid Earth, **99**, no. B3, 4715−4734, doi: 10.1029/93JB03282.

Mondol, N. H., J. Jahren, K. Bjørlykke, and I. Brevik, 2008, Elastic properties of clay minerals: The Leading Edge, **27**, no. 6, 758−770, doi: 10.1190/1.2944161.

Mueller, J. L., and S. Siltanen, 2012, Linear and nonlinear inverse problems with practical applications, Computational Science & Engineering: Society for Industrial and Applied Mathematics.

Müller, T., B. Gurevich, and M. Lebedev, 2010, Seismic wave attenuation and dispersion resulting from wave-induced flow in porous rocks—A review: Geophysics, **75**, no. 5, 75A147−175A164, doi: 10.1190/1.3463417.

Nakano, Y., and R. Arnold, 1973, Acoustic properties of frozen Ottawa sand: Water Resources Research, **9**, no. 1, 178−184, doi: 10.1029/WR009i001p00178.

Nakano, Y., and N. H. Froula, 1973, Sound and shock transmission in frozen soils: Proceedings of the 2nd International Conference on Permafrost: National Academy of Sciences, 359−369.

Nelder, J. A., and R. Mead, 1965, A simplex-method for function minimization: Computer Journal, **7**, no. 4, 308–313.

Nelson, F. E., O. A. Anisimov, and N. I. Shiklomanov, 2001, Subsidence risk from thawing permafrost: Nature, **410**, no. 6831, 889-890.

Nelson, F. E., O. A. Anisimov, and N. I. Shiklomanov, 2002, Climate Change and Hazard Zonation in the Circum-Arctic Permafrost Regions: Natural Hazards, **26**, no. 3, 203-225, doi: 10.1023/A:1015612918401.

Neumaier, A., 2000, MCS: global optimization by Multilevel Coordinate Search, version 2.0, http://www.mat.univie.ac.at/~neum/software/mcs/ accessed 22 Jul., 2012.

Nixon, J. F., 1988, Pile load tests in saline permafrost at Clyde River, Northwest Territories: Canadian Geotechnical Journal, **25**, no. 1, 24−32, doi: 10.1139/t88-003.

Nixon, J. F., and G. Lem, 1984, Creep and strength testing of frozen saline fine-grained soils: Canadian Geotechnical Journal, **21**, no. 3, 518−529, doi: 10.1139/t84-054.

O'Neill, A., M. Dentith, and R. List, 2003, Full-waveform P-SV reflectivity inversion of surface waves for shallow engineering applications: Exploration Geophysics, **34**, no. 3, 158–173, doi: 10.1071/Eg03158.

O'Neill, A., and T. Matsuoka, 2005, Dominant higher surface-wave modes and possible inversion pitfalls: Journal of Environmental and Engineering Geophysics, **10**, no. 2, 185–201, doi: 10.2113/Jeeg10.2.185.

O'Sullivan, J. B., 1966, Geochemistry of permafrost, Barrow, Alaska, in Kenneth B. Woods, A. J. Alter, James A. Bender, Richard L. Cameron and Thevor A. Harwood, eds., Proceedings of International Conference on Permafrost: National Academy of Sciences, 30–37.

Ogata, N., M. Yasuda, and T. Kataoka, 1983, Effects of salt concentration on strength and creep behavior of artificially frozen soils: Cold Regions Science and Technology, **8**, no. 2, 139−153, doi: 10.1016/0165-232X(83)90005-8.

Osterkamp, T. E., 1989, Occurrence and potential importance of saline permafrost in Alaska: Workshop on Saline Permafrost: University of Manitoba.

Osterkamp, T. E., 2001, Sub-sea permafrost, in John H. Steele, ed., Encyclopedia of Ocean Sciences (Second Edition): Academic Press, 559−569.

Pan, Y., J. Xia, and C. Zeng, 2013, Verification of correctness of using real part of complex root as Rayleigh-wave phase velocity with synthetic data: Journal of Applied Geophysics, **88**, no. 0, 94–100, doi: 10.1016/j.jappgeo.2012.09.012.

Pandit, B. I., and M. S. King, 1978, Influence of pore fluid salinity on seismic and electrical properties of rocks at permafrost temperatures: Proceedings of International Conference on Permafrost: U. S. National Academy of Sciences, 553–559.

Pandit, B. I., and M. S. King, 1979, A study of the effects of pore-water salinity on some physical properties of sedimentary rocks at permafrost temperatures: Canadian Journal of Earth Sciences, **16**, no. 8, 1566−1580, doi: 10.1139/e79-143.

Park, C. B., R. D. Miller, and J. H. Xia, 1999, Multichannel analysis of surface waves: Geophysics, **64**, no. 3, 800–808, doi: 10.1190/1.1444590.

Pavlakovic, B., M. Lowe, D. Alleyne, and P. Cawley, 1997, Disperse: a general purpose program for creating dispersion curves, in DonaldO Thompson and DaleE Chimenti, eds., Review of Progress in Quantitative Nondestructive Evaluation: Springer US, 185–192.

Perez, R. E., and K. Behdinan, 2007, Particle swarm approach for structural design optimization: Computers & Structures, **85**, no. 19–20, 1579-1588, doi: 10.1016/j.compstruc.2006.10.013.

Poli, R., J. Kennedy, and T. Blackwell, 2007, Particle swarm optimization: Swarm Intelligence, **1**, no. 1, 33-57, doi: 10.1007/s11721-007-0002-0.

Pošík, P., W. Huyer, and L. Pál, 2012, A comparison of global search algorithms for continuous black box optimization: Evolutionary Computation, 1–32.

Potter, R. W., M. A. Clynne, and D. L. Brown, 1978, Freezing point depression of aqueous sodium chloride solutions: Economic Geology, **73**, no. 2, 284−285, doi: 10.2113/gsecongeo.73.2.284.

Pounder, E. R., 1965, The physics of ice: Pergamon Press.

Povey, M. J. W., 1997, Multiphase media, Ultrasonic Techniques for Fluids Characterization: Academic Press, 47−90.

Prasad, M., and J. Dvorkin, 2004, Velocity and attenuation of compressional waves in brines: SEG Technical Program Expanded Abstracts: 1666−1669.

Press, W. H., S. A. Teukolsky, W. T. Vetterling, and B. P. Flannery, 1992, Numerical Recipes in C : the art of scientific computing. 2nd ed: Cambridge University Press.

Ramachandran, K., G. Bellefleur, T. Brent, M. Riedel, and S. Dallimore, 2011, Imaging permafrost velocity structure using high resolution 3D seismic tomography: Geophysics, **76**, no. 5, B187–B198, doi: 10.1190/Geo2010-0353.1.

Richart, F. E., J. R. Hall, and R. D. Woods, 1970, Vibrations of soils and foundations, Prentice-Hall international series in theoretical and applied mechanics: Prentice-Hall.

Rix, G. J., and E. A. Leipski, 1991, Accuracy and resolution of surface wave inversion: Recent advances in instrumentation, data acquisition and testing in soil dynamics: ASCE, 17–32.

Ruffell, J. P., T. R. Murphy, and C. A. Graham, 1990, Planning and execution of a 500 m corehole through offshore permafrost: Proceedings of 5th Canadian Permafrost Conference: National Research Council Canada, 271−282.

Ryden, N., and M. J. S. Lowe, 2004, Guided wave propagation in three-layer pavement structures: The Journal of the Acoustical Society of America, **116**, no. 5, 2902–2913, doi: 10.1121/1.1808223.

Ryden, N., and C. B. Park, 2004, Surface waves in inversely dispersive media: Near Surface Geophysics, **2**, no. 4, 187–197.

Ryden, N., and C. B. Park, 2006, Fast simulated annealing inversion of surface waves on pavement using phase-velocity spectra: Geophysics, **71**, no. 4, R49–R58, doi: 10.1190/1.2204964.

Sain, K., and A. K. Singh, 2011, Seismic quality factors across a bottom simulating reflector in the Makran Accretionary Prism, Arabian Sea: Marine and Petroleum Geology, **28**, no. 10, 1838–1843, doi: 10.1016/j.marpetgeo.2011.03.013.

Sain, K., A. K. Singh, N. K. Thakur, and R. Khanna, 2009, Seismic quality factor observations for gas-hydrate-bearing sediments on the western margin of India: Marine Geophysical Researches, **30**, no. 3, 137–145, doi: 10.1007/s11001-009-9073-1.

Schmitt, D. R., M. Welz, and C. D. Rokosh, 2005, High-resolution seismic imaging over thick, permafrost at the 2002 Mallik drill site, in S. R. Dallimore and T. S. Collett, eds., Scientific Results from the Mallik 2002 Gas Hydrate Production Research Well Program, MackenzieDelta, Northwest Territories, Canada: Geological Survey of Canada Bulletin 585.

Schön, J., 2011, Physical properties of rocks: a workbook, Handbook of Petroleum Exploration and Production: Elsevier.

Sellmann, P. V., J. Brown, R. Lewellen, H. McKim, and C. Merry, 1975, The classification and geomorphic implications of thaw lakes on the Arctic coastal plain, Alaska: U. S. Army Cold Regions Research and Engineering Laboratory Research Report.

Shaw, R., and S. Srivastava, 2007, Particle swarm optimization: A new tool to invert geophysical data: Geophysics, **72**, no. 2, F75-F83.

Sheriff, R. E., 2002, Encyclopedic dictionary of applied geophysics: Society of Exploration Geophysicists, 203–217.

Snieder, R., 1998, The role of nonlinearity in inverse problems: Inverse Problems, **14**, no. 3, 387–404.

Socco, L. V., and D. Boiero, 2008, Improved Monte Carlo inversion of surface wave data: Geophysical Prospecting, **56**, no. 3, 357–371, doi: 10.1111/j.1365-2478.2007.00678.x.

Socco, L. V., S. Foti, and D. Boiero, 2010, Surface-wave analysis for building near-surface velocity models—Established approaches and new perspectives: Geophysics, **75**, no. 5, A83–A102, doi: Doi 10.1190/1.3479491.

Socco, L. V., and C. Strobbia, 2004, Surface-wave method for near-surface characterization: a tutorial: Near Surface Geophysics, **2**, no. 4, 165–185.

Sondergeld, C., and C. Rai, 2007, Velocity and resistivity changes during freeze-thaw cycles in Berea sandstone: Geophysics, **72**, no. 2, E99−E105, doi: 10.1190/1.2435198.

Spaans, E. J. A., and J. M. Baker, 1996, The soil freezing characteristic: its measurement and similarity to the soil moisture characteristic: Soil Science Society of America Journal, **60**, no. 1, 13−19, doi: 10.2136/sssaj1996.03615995006000010005x.

Spetzler, H., and D. L. Anderson, 1968a, The effect of temperature and partial melting on velocity and attenuation in a simple binary system: Journal of Geophysical Research, **73**, no. 18, 6051–6060, doi: 10.1029/JB073i018p06051.

Spetzler, H., and D. L. Anderson, 1968b, The effect of temperature and partial melting on velocity and attenuation in a simple binary system: Journal of Geophysical Research, **73**, no. 18, 6051−6060, doi: 10.1029/JB073i018p06051.

Strobbia, C., A. Glushchenko, A. Laake, P. Vermeer, T. J. Papworth, and Y. Ji, 2009, Arctic near surface challenges: the point receiver solution to coherent noise and statics: First Break, **27**, no. 2, 69–76.

Thimus, J. F., J. Aguirre-Puente, F. Cohen-Tenoudji, and P. Leclaire, 1993, Ultraosnic measurements in frozen soils to −120°C: results and interpretation using different theoretical models: Proceedings of the 6th International Conference on Permafrost: National Academy of Sciences, 611−616.

Thurston, D. K., L. A. Theiss, and U. S. M. M. S. A. O. Region, 1987, Geologic report for the Chukchi Sea planning area, Alaska: regional geology, petroleum geology, and environmental geology: U.S. Department of the Interior, Minerals Management Service, Alaska OCS Region.

Tian, H., C. Wei, H. Wei, and J. Zhou, 2014, Freezing and thawing characteristics of frozen soils: bound water content and hysteresis phenomenon: Cold Regions Science and Technology, **103**, no. 0, 74−81, doi: 10.1016/j.coldregions.2014.03.007.

Timur, A., 1968, Velocity of compressional waves in porous media at permafrost temperatures: Geophysics, **33**, no. 4, 584−595, doi: 10.1190/1.1439954.

Tronicke, J., H. Paasche, and U. Böniger, 2012, Crosshole traveltime tomography using particle swarm optimization: A near-surface field example: Geophysics, **77**, no. 1, R19-R32.

Trupp, R., J. Hastings, S. Cheadle, and R. Vesely, 2009, Seismic in arctic environs: meeting the challenge: The Leading Edge, **28**, no. 8, 936−942, doi: 10.1190/1.3192840.

Tsuji, T., T. A. Johansen, B. O. Ruud, T. Ikeda, and T. Matsuoka, 2012, Surface-wave analysis for identifying unfrozen zones in subglacial sediments: Geophysics, **77**, no. 3, En17–En27, doi: 10.1190/Geo2011-0222.1.

Velli, Y. Y., and P. A. Grishin, 1983, On the functional dependence of the freezing point of soils on the composition of water soluble salts in an interstitial solution, Rheology of soils and engineering geocryology (Transl. from Russian): Canada Institute for Scientific and Technical Information, 193–196.

Vogt, C., K. Laihem, and C. Wiebusch, 2008, Speed of sound in bubble-free ice: The Journal of the Acoustical Society of America, **124**, no. 6, 3613−3618, doi: 10.1121/1.2996304.

Wang, Z., H. Wang, and M. Cates, 2001, Effective elastic properties of solid clays: Geophysics, **66**, no. 2, 428−440, doi: 10.1190/1.1444934.

Wathelet, M., D. Jongmans, and M. Ohrnberger, 2004, Surface-wave inversion using a direct search algorithm and its application to ambient vibration measurements: Near Surface Geophysics, **2**, no. 4, 211–221.

Williams, J. R., 1970, Ground water in the permafrost regions of Alaska : ground water in permafrost regions in Alaska occurs according to the same geologic and hydrologic principles prevailing in temperate regions, Geological Survey professional paper: U.S. Geological Survey.

Williams, J. R., and L. D. Carter, 1984, Engineering-geologic maps of northern Alaska, Barrow quadrangle, Open-file report 84-124: U.S. Geological Survey.

Winters, W. J., I. A. Pecher, W. F. Waite, and D. H. Mason, 2004, Physical properties and rock physics models of sediment containing natural and laboratory-formed methane gas hydrate: American Mineralogist, **89**, no. 8-9, 1221−1227.

Woeber, A. F., S. Katz, and T. J. Ahrens, 1963, Elasticity of selected rocks and minerals: Geophysics, **28**, no. 4, 658−663, doi: 10.1190/1.1439242.

Xia, J. H., R. D. Miller, and C. B. Park, 1999, Estimation of near-surface shear-wave velocity by inversion of Rayleigh waves: Geophysics, **64**, no. 3, 691–700, doi: 10.1190/1.1444578.

Xia, J. H., R. D. Miller, C. B. Park, and G. Tian, 2003, Inversion of high frequency surface waves with fundamental and higher modes: Journal of Applied Geophysics, **52**, no. 1, 45–57, doi: 10.1016/S0926-9851(02)00239-2.

Yilmaz, O., and A. Kocaoglu, 2012, Effect of lateral heterogeneity in the soil column on shear-wave velocity estimation by Rayleigh-wave inversion: The Leading Edge, **31**, no. 7, 758–765, doi: 10.1190/tle31070758.1.

Yong, R. N., C. H. Cheung, and D. E. Sheeran, 1979, Prediction of salt influence on unfrozen water content in frozen soils: Engineering Geology, **13**, no. 1–4, 137−155, doi: 10.1016/0013-7952(79)90027-9.

Yoshikawa, K., V. Romanovsky, N. Duxbury, J. Brown, and A. Tsapin, 2004, The use of geophysical methods to discriminate between brine layers and freshwater taliks in permafrost regions: Journal of Glaciology and Geocryology, **26**, 301−309.

Zhang, S. X., and L. S. Chan, 2003, Possible effects of misidentified mode number on Rayleigh wave inversion: Journal of Applied Geophysics, **53**, no. 1, 17–29, doi: 10.1016/S0926-9851(03)00014-4.

Zimmerman, R. W., and M. S. King, 1986, The effect of the extent of freezing on seismic velocities in unconsolidated permafrost: Geophysics, **51**, no. 6, 1285−1290, doi: 10.1190/1.1442181.

Zimov, S. A., E. A. G. Schuur, and F. S. Chapin, 2006, Permafrost and the global carbon budget: Science, **312**, no. 5780, 1612–1613, doi: 10.1126/science.1128908.

Appendices

Appendix A

A1 Emprical equation for estimating freezing point of saline soils

According to Velli and Grishin (1983), the freezing point of saline soils can be determined from

$$T_{fp} = -T_k \left(\frac{S_n}{1000 + S_n} \right)$$

where S_n is salinity in g/l (or parts per thousand), T_k is a reference temperature (57 °C for sea salt; 62 °C for NaCl).

A2 Parameter settings and termination criteria of the global-local hybrid optimization method

MCS.—MCS is equipped with a set of default parameter values that have been well tested. Here we list a number of key controlling parameters that we use for minimizing the n-dimensional objective function:

1) The maximum number of function calls $Nf_{max} = 50n^2$ (default);
2) The maximum split level $s_{max} = 5n + 10$ (default);
3) The maximum number of sweeps $N_{sw} = 3n$ (default);
4) The maximum number of local searches $N_{loc} = 0$ (i.e., the local-search enhancement is turned off).

NM.—Termination criteria of the NM method are chosen to let the search process go through generous amount of iterations for optimal convergence. In addition, a tolerance in vector movement distance is used to stop the search, which is to avoid wasting large amounts of iterations on negligible function-value improvements:

1) The maximum number of function calls $Nf_{max} = 700$;
2) The fractional tolerance in the simplex-vector distance moved in a search step $X_{tol} = 1 \times 10^{-4}$.

Appendix B

B1 Texture information of the saline permafrost core sample

The texture of the saline permafrost core sample was first measured with a laser diffraction particle size analyzer (Malvern Mastersizer 3000). Because the amount of clay was not well constrained by using the laser diffraction sizing technique alone, the texture information were then refined based upon the mineral composition measurements obtained through X-ray powder diffraction (XRPD) analysis. The results of this two-step procedure (detailed in Table B1.1) determined that the core sample is a silty-clayey sand (D_{50} ~53 μm) consisting of 52 vol% of sand, 30 vol% of silt, and 18 vol% of clay.

Table B1.1 Texture information of the saline permafrost core sample

Method	Results	
Laser diffraction particle size analysis	Particle types	vol%
	Medium sand (250–500 μm)	1.5
	Fine to very fine sand (50–250 μm)	50.5
	Sub-sand fines (< 50 μm, silt- and clay-sized particles)	48
X-ray powder diffraction (XRPD) analysis	Mineral types	vol%
	Quartz	68
	Plagioclase	11
	Clay minerals (kaolinite and chloride)	18
	Secondary minerals (dolomite, muscovite, and halite)	3
Combination	Texture classes	vol%
	Sand	52
	Silt	30
	Clay	18

B2 Volume fractions of ice and water

For a given initial (i.e., prior to freezing) pore-water salinity S_{n0} (in wt%), the corresponding freezing point T_{fp} (in °C) is (Potter et al. 1978)

$$T_{fp} = 0.00 - (0.581855 S_{n0} + 3.48896\times10^{-3} S_{n0}^2 + 4.314\times10^{-4} S_{n0}^3) \quad \text{(B2-1)}$$

For a given sub-freezing temperature T ($T < T_{fp}$; in °C), the minimum salinity S_n (in wt%) required to prevent the residual pore water from freezing is (Potter et al. 1978)

$$S_n = 1.76958|T| - 4.2384\times10^{-2}|T|^2 + 5.2778\times10^{-4}|T|^3 \quad \text{(B2-2)}$$

Assuming that in the temperature range between the freezing point T_{fp} (in °C) and the eutectic point $T_{eutectic}$ (in °C), the total mass of the dissolved salts m_{salt}^{total} remains constant in the residual pore water. Then, by denoting the initial mass of the pore water at above-freezing temperatures as m_{w0} and the mass of the residual pore water at sub-freezing temperatures as m_w, the mass conservation of the dissolved salts yields

$$m_{salt}^{total} = S_{n0} m_{w0} = S_n m_w \tag{B2-3}$$

Given that $m_{w0} = \rho_{w0} V_{w0}$ and $m_w = \rho_w V_w$, Equation B2-3 can be rewritten as

$$S_{n0} \rho_{w0} V_{w0} = S_n \rho_w V_w \tag{B2-4}$$

where ρ_w and V_w are the density and volume of the saline pore water, respectively, and their initial values are $\rho_{w0} = \rho_w \big|_{S_n = S_{n0}, T = T_0}$ and $V_{w0} = V_w \big|_{S_n = S_{n0}, T = T_0}$.

In saline permafrost, the initial volume of water V_{w0} equals to the total volume of the pore space V_{pore}^{total} ($V_{w0} = V_{pore}^{total}$). After reorganizing Equation B2-4, the unfrozen water saturation S_w ($S_w = V_w / V_{pore}^{total}$, the volume fraction of residual unfrozen water in the pore space; unitless fraction) and ice saturation S_i ($S_i = V_i / V_{pore}^{total}$, the volume fraction of ice in the pore space; unitless fraction) can be expressed as

$$\begin{aligned} S_w &= \frac{V_w}{V_{pore}^{total}} = \frac{V_w}{V_{w0}} = \frac{\rho_{w0} S_{n0}}{\rho_w S_n} \\ S_i &= \frac{V_i}{V_{pore}^{total}} = \frac{V_{pore}^{total} - V_w}{V_{pore}^{total}} = 1 - \frac{V_w}{V_{pore}^{total}} = 1 - S_w \end{aligned} \tag{B2-5}$$

If the initial pore-water salinity S_{n0} and the temperatures T are known, the salinities of the residual pore water S_n during freezing are given by Equation B2-2, and the pore-water densities ρ_w and ρ_{w0} can be obtained based upon Batzle and Wang (1992). Then the unfrozen water saturation (S_w) and ice saturation (S_i) of saline permafrost can be estimated by using Equation B2-5 within the temperature range of $T_{eutectic} \le T \le T_{fp}$.

Appendix C

C1 Properties of the elementary components for the effective-medium velocity modeling

Velocities, density, and elastic moduli of ice

- P- and S-wave velocity of ice (v_{Pi} and v_{Si}; in m/s) as functions of temperature (T; in °C) (Vogt et al. 2008):

$$v_{Pi}(T) = 3837.9 - 2.812T$$
$$v_{Si}(T) = 1826.0 - 1.435T \quad \text{(C1-1)}$$

- Density of ice (ρ_i; in kg/m3) as a function of temperature (T; in °C) (Pounder 1965):

$$\rho_i(T) = 917.0 - 0.1403T \quad \text{(C1-2)}$$

- Bulk, shear, and P-wave moduli of ice (K_i, G_i, and M_i; in Pa) as functions of temperature (T; in °C):

$$M_i(T) = v_{Pi}(T)^2 \rho_i(T)$$
$$G_i(T) = v_{Si}(T)^2 \rho_i(T) \quad \text{(C1-3)}$$
$$K_i(T) = M_i(T) - 4G_i(T)/3$$

P-wave velocity, density and bulk modulus of water (saline or non-saline)

We calculate P-wave velocity (v_{Pw}; in m/s) and density (ρ_w; in kg/m^3) of water based upon the Batzle and Wang (1992) model (Equation 27a, 27b, 28, 29, and Table 1) as functions of temperature (T; in °C) and salinity (S_n; in wt%) at an effective pressure of 1.01325×10^5 Pa (1 atm). We then obtain bulk modulus (K_w; in Pa) of water as a function of temperature (T; in °C) and salinity (S_n; in wt%):

$$K_w(T, S_n) = v_{Pw}(T, S_n)^2 \rho_w(T, S_n) \quad \text{(C1-4)}$$

Density and elastic moduli of sediment-grain minerals

The density and elastic moduli of the essential sediment-grain minerals used in our effective-medium modeling are listed in Table C1.1.

Table C1.1 Density and elastic moduli of sediment-grain minerals.

Mineral	K (GPa)	G (GPa)	ρ (kg/m^3)	References
Quartz	37.0	44.0	2650.0	Woeber et al. (1963)
Plagioclase	75.6	25.6	2630.0	Carmichael (1989)
Kaolinite (soft)	1.5	1.4	1618.7	Woeber et al. (1963)
Kaolinite (stiff)	55.0	31.8	4890.4	Katahara (1996)

C2 Volume fractions of ice and water

When the influences of pore-water salinities are dominant

Freezing point (T_{fp}; in °C) for a given initial pore-water salinity (i.e., pore-water salinity prior to freezing) (S_{n0}; in wt%) (Potter et al. 1978) can be described as,

$$T_{fp} = 0.00 - (0.581855 S_{n0} + 3.48896 \times 10^{-3} S_{n0}^2 + 4.314 \times 10^{-4} S_{n0}^3) \quad \text{(C2-1)}$$

For a given sub-freezing temperature ($T < T_{fp}$; in °C), the minimum salinity required to prevent the residual pore-water from freezing (S_n; in wt%) is (Potter et al. 1978):

$$S_n = 1.76958|T| - 4.2384 \times 10^{-2} |T|^2 + 5.2778 \times 10^{-4} |T|^3 \quad \text{(C2-2)}$$

Assume that in the temperature range between the freezing point (T_{fp}; in °C) and the eutectic point ($T_{eutectic}$; in °C), the total mass of the dissolved salts remains constant in the unfrozen pore-water. Then, by denoting the initial mass (prior to freezing) of the pore- water and the mass of the residual pore-water at sub-freezing temperatures as m_{w0} and m_w, respectively, the mass conservation of the dissolved salts can be expressed as

$$m_{salt} = S_{n0} m_{w0} = S_n m_w \quad \text{(C2-3)}$$

Given that $m_{w0} = \rho_{w0} V_{w0}$ and $m_w = \rho_w V_w$, we can rewrite Equation B-3 as

$$S_{n0} \rho_{w0} V_{w0} = S_n \rho_w V_w \quad \text{(C2-4)}$$

In saline permafrost, the initial volume of water equals to the total volume of the pore space. After reorganizing Equation C2-4, unfrozen water saturation (S_w; unitless fraction: the volume fraction of residual unfrozen-water in the pore space) and ice saturation (S_i; unitless fraction: the volume of ice in the pore space) can be expressed as

$$S_w = \frac{\rho_{w0} S_{n0}}{\rho_w S_n}$$
$$S_i = 1 - S_w \quad \text{(C2-5)}$$

where the initial density of the pore-water (prior to freezing) can be expressed as $\rho_{w0} = \rho_w|_{S_n = S_{n0}, T = T_0}$.

By combining expressions of water density (as described in Appendix C1) and Equation C2-2, unfrozen water saturation (S_w) and ice saturation (S_i) of saline permafrost can be estimated using Equation B-5 within the temperature range of $T_{eutectic} \le T \le T_{fp}$.

Based upon Anderson et al. (1973), under the influences of surface effects, the mass fraction of unfrozen water (w_w; unitless fraction: the mass fraction of unfrozen water relative to the total mass of the sediment) can be expressed as a function of temperature (T; in °C) and specific surface area of the sediment grains (S_a; in m^2/kg):

$$w_w = \frac{m_w}{m_{total}} = \exp(0.2618 + 0.5519 \ln S_a - 1.449 S_a^{-0.264} \ln \theta) \quad \text{(C2-6)}$$

where the grain specific area S_a can be calculated based upon the density (ρ_g; in kg/m^3) and diameter of the sediment grain (D_g; in m) using $S_a = 6/(\rho_g D_g)$; $\theta = 0 - T$ for non- saline permafrost (in °C), and $T_{eutectic} - T$ for saline permafrost (in °C).

In Equation C2-6, the total mass of sediment can be expressed as

$$m_{total} = \left(\rho_g (1 - \phi_{gf}) + \rho_{w0} \phi_{gf} \right) V_{total} \tag{C2-7}$$

where ϕ_{gf} is the porosity of the sediment-grain frame (unitless fraction: the volume of the pore space relative to the total volume).

And the total mass of the residual pore-water is

$$m_w = \rho_w V_w \tag{C2-8}$$

By combining Equation C2-7, C2-8, and C2-6, the volume fraction of unfrozen water (v_w; unitless fraction: the volume fraction of unfrozen water relative to the total volume of the sediment) can be expressed as

$$v_w = \frac{V_w}{V_{total}} = w_w \left(\frac{\rho_g (1 - \phi_{gf}) + \rho_{w0} \phi_{gf}}{\rho_w \big|_{S_n = 0}} \right) \tag{C2-9}$$

Note that in this step, considering salt precipitation under sub-eutectic temperatures, the density of the residual unfrozen water in saline permafrost is assumed to be equal to those of non-saline water.

Then, unfrozen water saturation (S_w; unitless fraction: the volume fraction of residual unfrozen-water in the pore space) and ice saturation (S_i; unitless fraction: the volume of ice in the pore space) can be estimated based upon Equation C2-9

$$\begin{aligned} S_w &= \frac{V_w}{V_{pore}} = \frac{V_w}{V_{total} \phi_{gf}} = \frac{v_w}{\phi_{gf}} \\ S_i &= 1 - S_w \end{aligned} \tag{C2-10}$$

Connecting the transition around the eutectic point for saline permafrost

Note that the surface-effect-related equations derived from Anderson et al. (1973) are based upon empirical equations in which the fraction must be relative to the total volume of the pore space. But in saline-sample, when the temperature drops below the eutectic point, the starting volume of the residual water is already small. To ensure a smooth connection at the "elbow" part of the unfrozen water function (i.e., immediately below the eutectic), we choose a piecewise approach to connect this transition.

- We extend Equation C2-5 to estimate water saturation at temperatures that are immediately below eutectic. The results are denoted as S_{w1};
- With $\theta = T_{eutectic} - T$ for saline permafrost (in °C), we also estimate the surface-effect-controlled water saturation with Equation C2-10, and denote the results as S_{w2};
- For the near-eutectic transition, unfrozen water saturation (S_w; unitless fraction: the volume fraction of residual unfrozen-water in the pore space) and ice saturation (S_i; unitless fraction: the volume of ice in the pore space) are then expressed as

$$\begin{aligned} S_w &= \begin{cases} S_{w1} & (\text{if } S_{w1} < S_{w2}) \\ S_{w2} & (\text{if } S_{w1} \geq S_{w2}) \end{cases} \\ S_i &= 1 - S_w \end{aligned} \tag{C2-11}$$

Although this way of connecting the transition is not physically rigorous, it ensures a smooth connection, and counts in grain-size-induced supercooling at temperatures immediately below the eutectic.

Summary

All the equations used for estimating volume fractions of ice and water under various temperature and salinity conditions are compiled into Table C2.1.

Table C2.1 List of equations for estimating volume fractions of ice and water.

Temperatures (T; in °C)	S_w and S_i in saline sample	S_w and S_i in non-saline sample
$T > T_{fp}$	$S_w = 1; S_i = 0$	$S_w = 1; S_i = 0$
$T_{eutectic} \le T \le T_{fp}$	Equation C2-5	Equation C2-10
$T_{eutectic} - \Delta T_{transition} < T < T_{eutectic}$	Equation C2-11	Equation C2-10
$T \le T_{eutectic} - \Delta T_{transition}$	Equation C2-10	Equation C2-10

C3 Effective medium velocity modeling: a two-end-member mixing approach

In this appendix, we walk the readers through the workflow of the two-end-member mixing model (Figure C3.1) and present the key equations that are involved.

The fully frozen end-member (ice-saturated sediment)

The fully frozen end-member is approximated as a composite consisting of spherical sediment grains and pore-ice as ice-filled penny cracks. The effective moduli of the fully frozen end-member are calculated based upon the self-consistent approximation (SCA) (Berryman 1995). Note that SCA is indiscriminate toward the constituents of the composite. Hence, the self-consistent effective moduli are derived from the combination of two terms and $\{K_2, G_2\}$ that must satisfy:

$$\begin{aligned} K_1 + K_2 &= 0 \\ G_1 + G_2 &= 0 \end{aligned} \tag{C3-1}$$

where $\{K_1, G_1\}$ and $\{K_2, G_2\}$ represent the following two scenarios:

- Ice as penny-shaped inclusions embedded in the self-consistent effective medium

$$\begin{aligned} K_1 &= f_i(K_i - K_*)P_{*i}^{penny-crack} \\ G_1 &= f_i(G_i - G_*)Q_{*i}^{penny-crack} \quad \text{, and } f_i = \phi_{gf} \end{aligned} \tag{C3-2}$$

  where f_i = volume fraction of ice inclusions; ϕ_{gf} = porosity of the grain frame; K_i = bulk modulus of ice; G_i = shear modulus of ice; K_* = the self-consistent effective bulk modulus; G_* = the self-consistent effective shear modulus; and $P_{*i}^{penny-crack}$ and $Q_{*i}^{penny-crack}$ coefficients are calculated with ice as penny crack inclusions and the effective medium as the background material:

$$P_{*i}^{penny-crack} = \frac{K_* + \frac{4}{3}G_i}{K_i + \frac{4}{3}G_i + \pi\alpha_i\beta_*}$$

$$Q_{*i}^{penny-crack} = \frac{1}{5}\left(1 + \frac{8G_*}{4G_i + \pi\alpha_i(\mathrm{G}_* + 2\beta_*)} + 2\frac{K_i + \frac{2}{3}(G_i + G_*)}{K_i + \frac{4}{3}G_i + \pi\alpha_i\beta_*}\right) \quad \text{(C3-3)}$$

with α_i = the aspect ratio of the ice-filled penny shaped cracks; and $\beta_* = G_*\frac{3K_* + G_*}{3K_* + 4G_*}$.

- Sediment grains as spherical inclusions embedded in the self-consistent effective medium

$$K_2 = f_g(K_g - K_*)P_{*g}^{sphere}$$

$$G_2 = f_g(G_g - G_*)Q_{*g}^{sphere} \quad , and \ f_g = 1 - \phi_{gf} \quad \text{(C3-4)}$$

where f_g = volume fraction of sediment grains; K_g = bulk modulus of the sediment-grain mineral; G_g = shear modulus of the sediment-grain mineral; and P_{*g}^{sphere} and Q_{*g}^{sphere} coefficients are calculated with sediment grains as spherical inclusions and the effective medium as the background material:

$$P_{*g}^{sphere} = \frac{K_* + \frac{4}{3}G_*}{K_g + \frac{4}{3}G_*}$$

$$Q_{*g}^{sphere} = \frac{G_* + \zeta_*}{G_g + \zeta_*} \quad \text{(C3-5)}$$

with $\zeta_* = \frac{G_*}{6}\left(\frac{9K_* + 8G_*}{K_* + 2G_*}\right)$.

Then a combination of Equation C3-1, C3-2, and C3-4 forms a set of coupled equations that are used to iteratively solve for the self-consistent effective moduli K_* and G_*, starting from an initial guess as K_{*0} and G_{*0}.

In the end, the effective moduli of the fully frozen end-member (K_{is} and G_{is}; as the effective moduli of the ice-saturated, stiff end-member) equal to the optimal solution of K_* and G_*:

$$K_{is} = K_*$$

$$G_{is} = G_* \quad \text{(C3-6)}$$

The fully unfrozen end-member (water-saturated sediment)

The fully unfrozen end-member is approximated as a random dense pack of sediment grains saturated with water (saline or non-saline).

- The effective moduli of the dry granular frame K_{gf} and G_{gf} are first calculated with Hertz-Mindlin contact theory (Mindlin 1949):

$$K_{gf} = \left(\frac{C^2(1-\phi_{gf})^2 G_g^2}{18\pi^2(1-\upsilon_g)^2} P \right)^{\frac{1}{3}}$$
$$G_{gf} = \left(\frac{5-4\upsilon_g}{5(2-\upsilon_g)} \right) \left(\frac{3C^2(1-\phi_{gf})^2 G_g^2}{2\pi^2(1-\upsilon_g)^2} P \right)^{\frac{1}{3}} \quad \text{(C3-7)}$$

where $\upsilon_g = \frac{3K_g - 2G_g}{2(3K_g + G_g)}$ is the Poisson's ratio of the sediment grain; P = hydrostatic confining pressure (= 1 atm in our modeling for the laboratory data); C = the coordination number (the average number of contacts that each grain has with surrounding grains), and it is related to the grain frame porosity ϕ_{gf} based upon a cubic spline interpolation of empirical coefficients that can be found in Mavko et al. (2009) (Table 5.1.4).

- The effective moduli of the water-saturated granular pack K_{ws} and G_{ws} are then calculated based upon Biot's fluid substitution equations for the high-frequency limiting velocities (Johnson and Plona 1982)

$$K_{sw} = \left(v_{P\infty sw}^2 - \frac{4}{3} v_{S\infty sw}^2 \right) \rho_{sw}$$
$$G_{sw} = v_{S\infty sw}^2 \rho_{sw} \quad \text{(C3-8)}$$

where the average density of the water-saturated granular pack is

$$\rho_{sw} = \rho_g(1-\phi_{gf}) + \rho_w \phi_w$$

and the high-frequency limiting velocities are given by

$$v_{P\infty sw} = \left(\frac{\Delta + \left(\Delta^2 - 4(\rho_{11}\rho_{22} - \rho_{12}^2)(PR - Q^2) \right)^{\frac{1}{2}}}{2(\rho_{11}\rho_{22} - \rho_{12}^2)} \right)^{\frac{1}{2}}$$
$$v_{S\infty sw} = \left(\frac{G_{gf}}{\rho_{sw} - \phi_{gf}\rho_w \tau^{-1}} \right)^{\frac{1}{2}} \quad \text{(C3-9)}$$

where $\tau = 1 - \frac{1}{2}\left(1 - \frac{1}{\phi_{gf}}\right)$ is the tortuosity (defined as the ratio between total flow-path length to the total length of the porous medium) for spherical pores (Berryman 1981) and the associated coefficients as follows

$$P = \frac{K_g\left(\left(1-\phi_{gf}\right)\left(1-\phi_{gf}-\frac{K_{gf}}{K_g}\right)+\phi_{gf}\frac{K_{gf}}{K_w}\right)}{1-\phi_{gf}-\frac{K_{gf}}{K_g}+\phi_{gf}\frac{K_g}{K_w}}+\frac{4}{3}G_{gf}$$

$$Q = \frac{\phi_{gf}K_g\left(1-\phi_{gf}-\frac{K_{gf}}{K_g}\right)}{1-\phi_{gf}-\frac{K_{gf}}{K_g}+\phi_{gf}\frac{K_g}{K_w}}$$

$$R = \frac{\phi_{gf}^2 K_g}{1-\phi_{gf}-\frac{K_{gf}}{K_g}+\phi_{gf}\frac{K_g}{K_w}}$$

$$\rho_{11} = \left(1-\phi_{gf}\right)\rho_g - \left(1-\tau\right)\phi_{gf}\rho_w \tag{C3-10}$$

$$\rho_{22} = \tau\phi_{gf}\rho_w$$

$$\rho_{12} = \left(1-\tau\right)\phi_{gf}\rho_w$$

$$\Delta = P\rho_{22} + R\rho_{11} - 2Q\rho_{12}$$

The two-end-member mixing approach

With the elastic moduli of the stiff, ice-saturated end-member $\{K_{is}, G_{is}\}$ and the soft, water-saturated end-member $\{K_{ws}, G_{ws}\}$, the effective moduli of saline permafrost are calculated based upon Hashin-Shtrikman-Hill average (Hashin and Shtrikman 1963, Hill 1952) of the two end- members for the entire range of water/ice saturations

$$\begin{aligned} K_{eff} &= \frac{1}{2}\left(K_{HS+} + K_{HS-}\right) \\ G_{eff} &= \frac{1}{2}\left(G_{HS+} + G_{HS-}\right) \end{aligned} \tag{C3-11}$$

where the Hashin-Shtrikman upper bounds are

$$K_{HS+} = K_{is} + \frac{f_{ws}}{\left(K_{ws} - K_{is}\right)^{-1} + f_{is}\left(K_{is} + \frac{4}{3}G_{is}\right)^{-1}}$$

$$G_{HS+} = G_{is} + \frac{f_{ws}}{\left(G_{ws} - G_{is}\right)^{-1} + 2f_{is}\left(\frac{K_{is} + 2G_{is}}{5G_{is}\left(K_{is} + \frac{4}{3}G_{is}\right)}\right)} \quad \text{(C3-12)}$$

and the Hashin-Shtrikman lower bounds are given by

$$K_{HS-} = K_{ws} + \frac{f_{is}}{\left(K_{is} - K_{ws}\right)^{-1} + f_{ws}\left(K_{ws} + \frac{4}{3}G_{ws}\right)^{-1}}$$

$$G_{HS-} = G_{ws} + \frac{f_{is}}{\left(G_{is} - G_{ws}\right)^{-1} + 2f_{ws}\left(\frac{K_{ws} + 2G_{ws}}{5G_{ws}\left(K_{ws} + \frac{4}{3}G_{ws}\right)}\right)} \quad \text{(C3-13)}$$

and the volume fractions of the two end-members are given by $f_{is} = S_i$ and $f_{ws} = S_w$, where S_i and S_w are the ice and water saturation that are estimated based upon Equations shown in Appendix C2 (Table C2.1).

Then P-wave and S-wave velocity of saline permafrost for the entire range of water/ice saturations are expressed as

$$v_P = \sqrt{\frac{K_{eff} + \frac{4}{3}G_{eff}}{\rho}} \text{ and } v_S = \sqrt{\frac{G_{eff}}{\rho}} \quad \text{(C3-14)}$$

with the average density $\rho = \rho_g(1-\phi_{gf}) + \rho_i S_i \phi_{gf} + \rho_w S_w \phi_{gf}$.

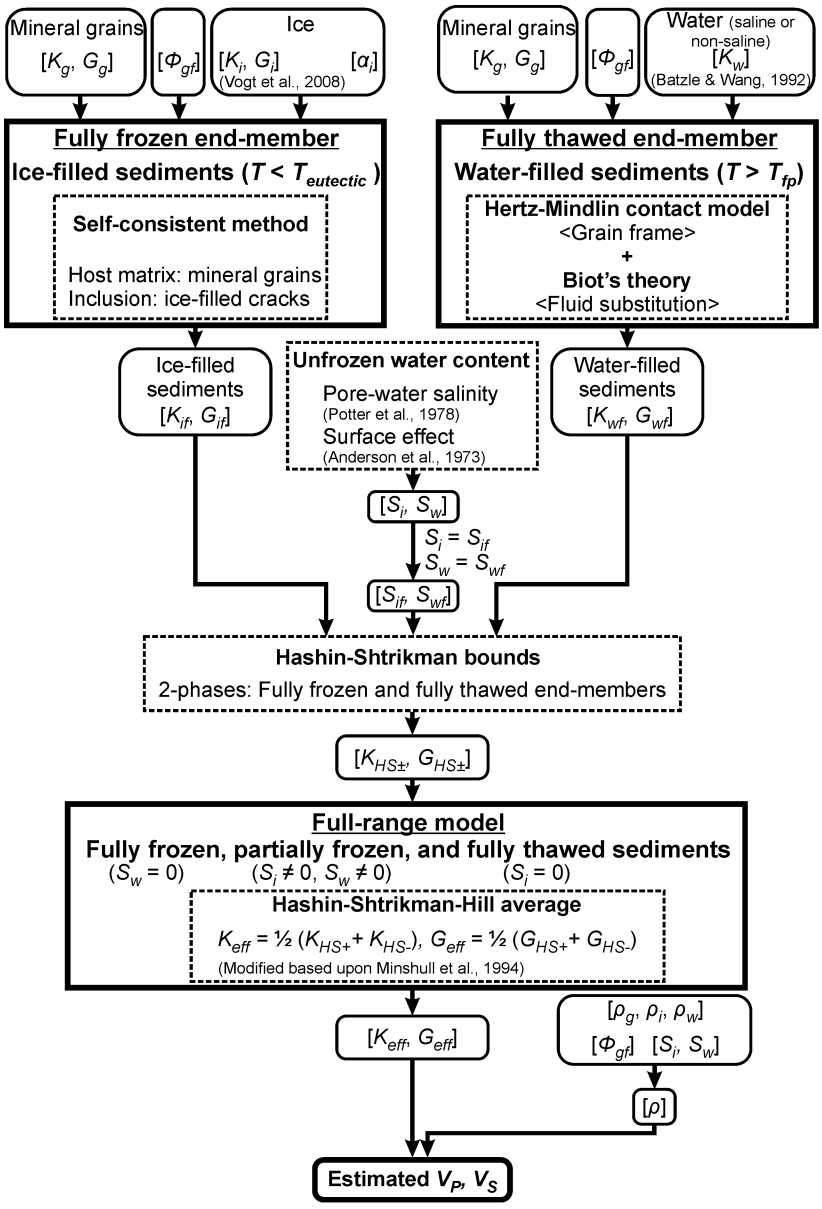

Figure C3.1 Workflow of the two-end-member mixing model. f_{is} = the volume fraction of the ice-saturated, fully frozen end-member; f_{ws} = the volume fraction the water-saturated, fully unfrozen end-member; K = bulk modulus; G = shear modulus; T = temperature; $T_{eutectic}$ = the eutectic point; T_{fp} = the freezing point; ϕ_{gf} = porosity of the sediment-grain frame; α_i = the aspect ratio of the ice-filled cracks.